Title
Novel Approaches to Carbon Capture: Biomimetic Absorption and Solar Desorption

Author
Nguyen, Du

Publication Date
2015

Peer reviewed|Thesis/dissertation

UNIVERSITY OF CALIFORNIA,
IRVINE

Novel Approaches to Carbon Capture: Biomimetic Absorption and Solar Desorption

DISSERTATION

submitted in partial satisfaction of the requirements
for the degree of

DOCTOR OF PHILOSOPHY

in Chemical and Materials Physics

by

Du Thai Nguyen

Dissertation Committee:
Assistant Professor Aaron Esser-Kahn, Chair
Professor Peter Taborek
Professor Michael Dennin

2015

DEDICATION

To
my family
for always supporting me

TABLE OF CONTENTS

LIST OF FIGURES

LIST OF TABLES

ACKNOWLEDGMENTS

I would like to thank my committee chair, principle investigator, and mentor, Aaron Esser-Kahn. It was rewarding to work not only on a captivating research project, but also experience building a new lab group from its foundations. His guidance and enthusiasm has helped me develop in a full-fledged researcher and I will always be thankful for that.

To Lalisa Stutts and Janine Tom, I would like to offer my sincere thanks. I'm glad you were both with me to build the lab from the ground up. Go dream team! To Kyle Brubaker and Stan Hiew, thanks for always spending to time to think of crazy and exciting ideas, even if most of them didn't work. To Dr. Maya Kleiman, thank you for being my office neighbor and giving good insights to my projects. To Nari Ryu and Dr. Rock Mancini although our projects have little in common, thank you for being great lab mates. You've all been very helpful troubleshooters for everything I've worked on in lab. It's been fun see all of your projects grow and develop over the years. Lastly, to all of the newer members of the lab, while I haven't been able to know you all better, I wish you all the very best.

I would also like to thank everyone that has helped me with the various characterization instruments and technical aid. I would like to thank Jian-Guo Zheng and Wytze Van Der Veer for use of the Calit2 Microscopy Center and Laser Spectroscopy Facility at the University of California, Irvine. I would also like to thank Sabra Djomehri and Yongxue Li for assistance with CT imaging. I thank Lee Moritz at the UCI Physical Sciences Machine Shop for machining our fabrication support devices. I would like to thank Prof. Peter Taborek and Robert Joachim for the aid and use of their high-speed photography equipment.

The text of Chapter 2 is a reprint of the material as it appears in Advanced Functional Materials. The co-author listed in this publication directed and supervised research which forms the basis for the dissertation.

The text of Chapter 3 is a reprint of the material as it appears in Materials Horizons. The co-author listed in this publication directed and supervised research which forms the basis for the dissertation.

The text of Chapter 4 is a reprint of the material as it appears in ACS Applied Materials and Interfaces. The co-author listed in this publication directed and supervised research which forms the basis for the dissertation.

The text of Chapter 5 is a reprint of the material as it appears in Angewandte Chemie International Edition. The co-author listed in this publication directed and supervised research which forms the basis for the dissertation.

The text of Chapter 6 is a reprint of the material as it appears in Energy and Environmental Science. The co-author listed in this publication directed and supervised research which forms the basis for the dissertation.

Lastly, I would like to thank our funding sources. This work was supported by the AFOSR

Young Investigator Program under FA9550-12-1-0352 and a 3M Non-Tenured Faculty Award. I was supported by the Department of Defense (DoD) through the National Defense Science & Engineering Graduate Fellowship (NDSEG) Program.

CURRICULUM VITAE

Du Thai Nguyen

EDUCATION

Doctor of Philosophy in Physics **2015**
University of California, Irvine *Irvine, California*

Bachelor of Science in Physics **2010**
Michigan State University *East Lansing, Michigan*

RESEARCH EXPERIENCE

Graduate Research Assistant **2011–2015**
University of California, Irvine *Irvine, California*

Professorial Assistant **2007–2010**
Michigan State University *East Lansing, Michigan*

PUBLICATIONS

C.C. Kuo, Y. Li, D. Nguyen, S. Buchsbaum, L. Innes, A. P. Esser-Kahn, L. Valdevit, L. Sun, Z. Siwy, M. Dennin. Macroscopic Strain Controlled Ion Current in an Elastic Microchannel. *Journal of Applied Physics*(2015)

Nguyen, D.T., Kleiman, M., Truong, R., and Esser-Kahn, A.P. Bio-inspired Microvascular Exchangers Employing Circular Packing - Designing Synthetic Rete Mirabile. *Mater. Horiz.*, **1** 602-607 (2014).

Nguyen, D.T., Truong, R., Lee, R., Goetz, S.A., and Esser-Kahn, A.P. Photothermal release of CO2 from capture solutions using nanoparticles. *Energy Environ. Sci.*, **7**, 2603-2607 (2014).

Nguyen, D.T., Kleiman, M., Ryu, K.A., Hiew, S., Brubaker, K., Mughnetsyan, R., Truong, R., Dolan, B., Tackett, E., and Esser-Kahn, A.P. Three-Dimensional Confromal Coatings through the Entrapment of Polymer Membrane Precursors. *ACS Applied Materials and Interfaces*, **6**, 2830-2835 (2014).

Nguyen, D.T. and Esser-Kahn, A.P. A Microvascular System for Chemical Reactions Using Surface Waste Heat. *Angewandte Chemie International Edition*, **52**, 13731-13734 (2013).

Nguyen, D.T., Leho, Y.T., and Esser-Kahn, A.P. Process of Making Three-dimensional Microstructures using Vaporization of a Sacrificial Component. *Journal of Visualized Experiments*, **81**, e50459 (2013).

Nguyen, D., Leho, Y, and Esser-Kahn, A.P. The Effect of Membrane Thickness on a Microvascular Gas Exchange Unit. *Advanced Functional Materials*, **23**, 100-106 (2013).

Nguyen, D., Leho, Y, and Esser-Kahn, A.P. A Three-Dimensional Microvascular Exchange Unit for Carbon Dioxide Capture. *Lab Chip*, **12**, 1246-1250 (2012).

G. Perdikakis, M. Sasano, Sam M. Austin, D. Bazin, C. Caesar, S. Cannon, J.M. Deaven, H.J. Doster, C.J. Guess, G.W. Hitt, J. Marks, R. Meharchand, D.T. Nguyen, D. Peterman, A. Prinke, M. Scott, Y. Shimbara, K. Thorne, L. Valdez, R.G.T. Zegers. LENDA: A low energy neutron detector array for experiments with radioactive beams in inverse kinematics. *Nucl. Instrum. Methods Phys. Res.*, **686**, 117-124 (2012).

G. Perdikakis, Sam M. Austin, D. Bazin, C. Caesar, J. M. Deaven, C. J. Guess, G. W. Hitt, R. T. Meharchand, D. T. Nguyen, Y. Shimbara, K. Thorne, and R. G. T. Zegers. LENDA: A Low Energy Neutron Detector Array for Studies of (p,n) Reactions With Radioactive Beams. *IEEE Transactions on Nuclear Science*, **56**, 1174-1178 (2009).

ABSTRACT OF THE DISSERTATION

Novel Approaches to Carbon Capture: Biomimetic Absorption and Solar Desorption

By

Du Thai Nguyen

Doctor of Philosophy in Chemical and Materials Physics

University of California, Irvine, 2015

Assistant Professor Aaron Esser-Kahn, Chair

Global climate change is one of the most pressing issues that we currently face. With atmospheric CO_2 level reaching 400 ppm, they are higher now than at any point in the last 800,000 years. However, the reduction of CO_2 emissions remains a significant challenge. Current CO_2 capture technologies are estimated to increase the cost of energy by 80%. As a result, we seek to find less costly methods of capturing CO_2 from point sources by looking at improving current CO_2 capture solvent absorption and desorption efficiency. CO_2 absorption can be made more efficient by looking towards the avian lung. In that system, hierarchically structured capillaries with high specific surface areas enable more efficient mass transport. We have developed mass transport devices that use these principles for efficient capture of CO_2 using a sacrificial element fabrication technique. CO_2 desorption can be enhanced through the use of waste heat and light absorbing nanoparticles. Microstructures could be formed around hot surfaces in order to capture the emitted waste heat. The smaller size scale of the structures enables more efficient use of the waste heat. Carbon black nanoparticles can generate high local heat gradients in the presence of light. The localized photothermal heat generation enable the use of solar energy to drive CO_2 desorption in capture fluids in order to reduce energy costs.

Chapter 1

Introduction

1.1 Motivation

Each year, almost 29 billion metric tons of CO_2 are released into the atmosphere from anthropogenic sources. [1] This results in an atmospheric CO_2 concentration that is higher now than at any other point in history within the past 800,000 years.[2] These emissions are primarily caused by the combustion of fossil fuels which are expected to remain a primary source of energy production for the next 20 years.[3] As CO_2 is a major contributor to the global climate change, a route to lower emissions is required. Carbon capture and sequestration technologies (CCS) are being researched as a means of reducing CO_2 emissions from point sources such as power plants. In proposed CCS technologies, CO_2 is captured, compressed, transported, and stored in subterranean or submarine environments.[4] The U.S. Dept. of Energy has set a goal of achieving 90% CO_2 capture with the cost of energy increasing by no more than 35%.[5] The use of amine-based aqueous solutions such as monoethanolamine (MEA) is currently one of the most attainable methods of separating CO_2 from flue streams as they have already been used industrially for natural gas purification and food-grade CO_2

production.[6] However, using MEA is estimated to increase the cost of energy for a new plant by 80-85% and reduce the plant's efficiency by 30%, which hinders its widespread adoption.

1.2 Post-Combustion CO_2 Capture

In a conventional post-combustion CO_2 capture system, flue gas from a power plant is directed to a CO_2 absorption column(Figure 1.1). There, the CO_2 in the flue gas is captured by MEA and flue gas exits as a purified gas stream. The CO_2 rich MEA is then pumped through a desorption column where the solution is heated to 120 °C to release the CO_2 in a concentrated form. The concentrated CO_2 is collected and compressed for sequestration. Last the CO_2 lean MEA is pumped back into the absorption column, completing the CO_2 capture cycle.

1.2.1 CO_2 Absorption

In order to implement post-combustion CO_2 capture, one area of needed improvement is in the absorption column. The volume of the absorption column required for a typical power plant is very large. As a result, the large volume serves as a roadblock towards retrofitting existing power plants. While it may be possible to design newer plants with this constraint in mind, existing plants must be considered for practical implementation of CO_2 capture technologies.

Many solutions using different chemistries have emerged as potential methods of capturing CO_2 from mixed gas streams including solid sorbents, new solvents, and membrane technologies.[7–15] In order for some of these solutions to be implemented at scales beyond the laboratory, they require larger, patterned structural platforms. However, very little re-

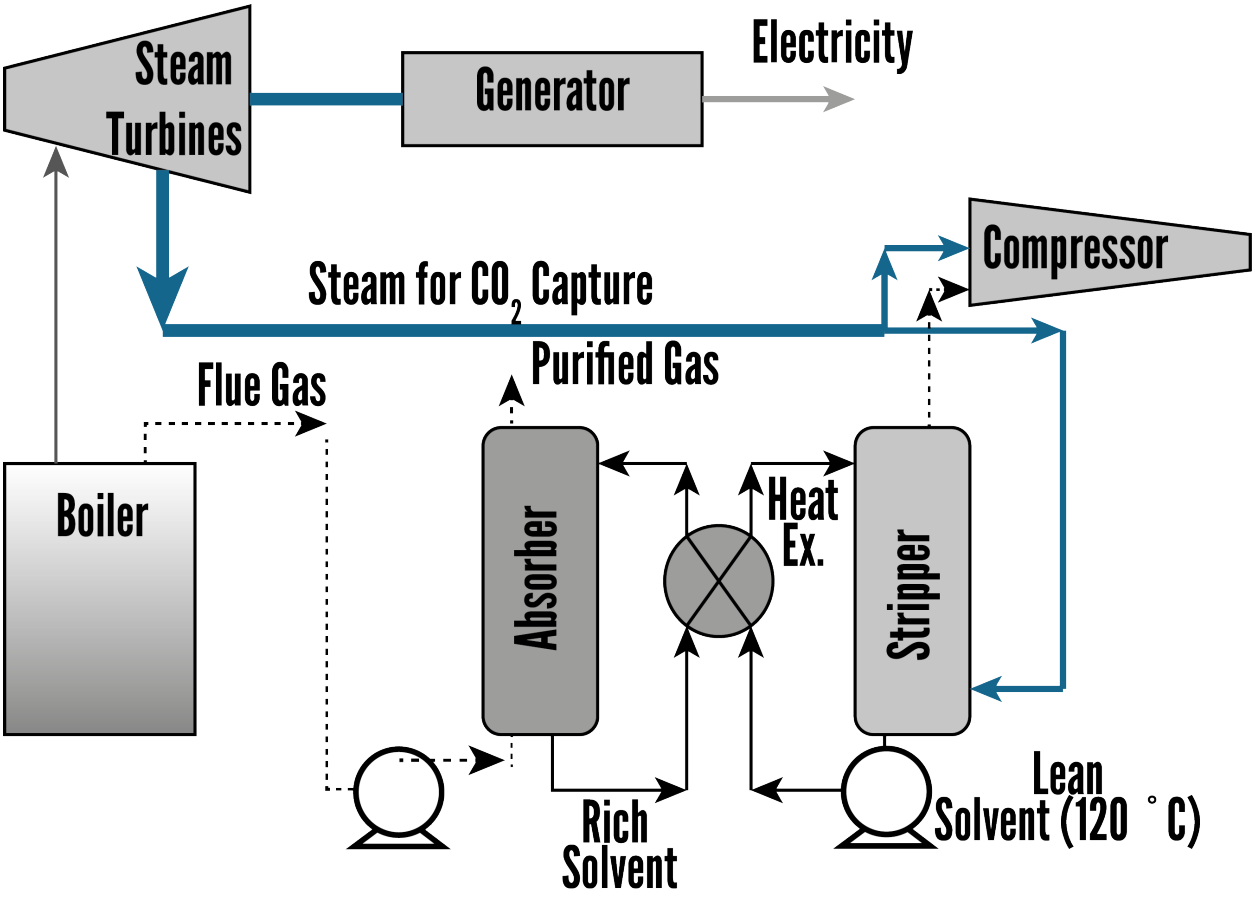

Figure 1.1: Representative schematic of post-combustion CO_2 capture.

search has been done in synthesizing these new platform materials. In nature, gas exchange is critical for survival and requires energy efficient systems. In contrast to current research, these natural systems use many different physical structures for gas exchange with very few different chemical methods. Inspired by nature, we are working towards the goal of building a platform analogous to the natural lung, a modular gas exchange system that has a low footprint, high-selectivity, and requires little energy.[16] Many methods have been developed to create vascular structures in soft materials for self-healing materials, tissue-growth and autonomic cooling.[17–26]. Additionally, micro-structured materials have advanced the fields of heat exchange, chemical analysis, flow chemistry, fuel cells, and carbon capture, and are currently advancing the field of tissue engineering.[14, 18, 26–47] Despite these successes, improved heat and mass micro-exchangers would benefit many applications.[48–51]

We have recently demonstrated the novel synthesis of microvascular bio-mimetic gas exchange units capable of capturing CO_2.[35] These gas exchange units are three-dimensional arrays composed of hollow micro-channels patterned within a polymer resin. The patterning of the channels creates short, polymer-filled separations that have many properties of the given polymer membrane. Our microvascular system also allows for the well-defined geometrical positioning of gases and fluids. This microvascular design allows for high specific surface areas, which enhances the reactivity between capture fluids and gases. Furthermore, our microvascular structures can serve as a new platform for enhancing the larger scale function of emerging low-energy chemical solutions to carbon capture. Each microvascular unit is made with entirely commercially available components and can therefore be constructed in a scalable manner. We detail our effort to improve exchange rates and to better understand the relationship between the positions of individual channels in our material as well as the importance of hierarchically structured microvascular channels.

1.2.2 CO_2 Desorption

Another difficulty in applying post-combustion CO_2 capture technologies is the high energy cost. During the desorption process, energy is parasitically drawn from the power plant, reducing its output. Part of the this energy cost comes from the energy required to break the bond between MEA and CO_2 (83 kJ/mol). However, there is a large energy cost in heating the capture fluid which is compost mostly of water (70 wt%). Most work is aimed towards reducing this energy cost through chemical means, however, few consider methods of harnessing alternative sources of energy. We look at two possible alternative sources of energy. The first is the use of low-grade waste heat from surfaces to provide energy for the chemical reactions. The waste heat is accessed by microchannels, up to meters in length, conformed to heated ceramic and metal surfaces in three-dimensional configurations. The other source of energy that we seek to use is solar energy. Using light absorbing nanoparticles, heat can be generated locally, resulting in enhanced vapor generation.[52, 53]

Bibliography

[1] P. Friedlingstein, R. A. Houghton, G. Marland, J. Hackler, T. A. Boden, T. J. Conway, J. G. Canadell, M. R. Raupach, P. Ciais, and C. Le Qur. Update on CO_2 emissions. *Nature Geoscience*, 3(12):811–812, November 2010.

[2] Dieter Lüthi, Martine Le Floch, Bernhard Bereiter, Thomas Blunier, Jean-Marc Barnola, Urs Siegenthaler, Dominique Raynaud, Jean Jouzel, Hubertus Fischer, Kenji Kawamura, and Thomas F. Stocker. High-resolution carbon dioxide concentration record 650,000800,000years before present. *Nature*, 453(7193):379–382, May 2008.

[3] DOE. *Annual Energy Outlook, 2011 with Projections to 2035*, 2011.

[4] Howard J. Herzog. Peer Reviewed: What Future for Carbon Capture and Sequestration? *Environmental Science & Technology*, 35(7):148A–153A, April 2001.

[5] Timothy J. Skone. Carbon Dioxide Capture from Existing Coal-Fired Power Plants. Technical Report DOE/NETL-401/110907, U.S. Department of Energy, November 2007.

[6] J. P. Ciferno, T. E. Fout, A. P. Jones, and J. T. Murphy. Capturing Carbon from Existing Coal-Fired Power Plants | AIChE. *Chemical Engineering Progress*, 105:33–41, April 2009.

[7] David Britt, Hiroyasu Furukawa, Bo Wang, T. Grant Glover, and Omar M. Yaghi. Highly efficient separation of carbon dioxide by a metal-organic framework replete with open metal sites. *Proceedings of the National Academy of Sciences*, 106(49):20637 – 20640, December 2009.

[8] Hailian Li, Mohamed Eddaoudi, M. O'Keeffe, and O. M. Yaghi. Design and synthesis of an exceptionally stable and highly porous metal-organic framework. *Nature*, 402(6759): 276–279, November 1999.

[9] Jos D. Figueroa, Timothy Fout, Sean Plasynski, Howard McIlvried, and Rameshwar D. Srivastava. Advances in CO_2 capture technology–The U.S. Department of Energy's Carbon Sequestration Program. *International Journal of Greenhouse Gas Control*, 2 (1):9–20, January 2008.

[10] R Franchi, P Harlick, and A Sayari. A high capacity, water tolerant adsorbent for CO_2: diethanolamine supported on pore-expanded MCM-41. In *Studies in Surface Science and Catalysis*, volume 156, pages 879–886. Elsevier, 2005.

[11] Rajesh A. Khatri, Steven S. C. Chuang, Yee Soong, and McMahan Gray. Thermal and Chemical Stability of Regenerable Solid Amine Sorbent for CO_2 Capture. *Energy & Fuels*, 20(4):1514–1520, July 2006.

[12] Eleanor D. Bates, Rebecca D. Mayton, Ioanna Ntai, and James H. Davis. CO_2 Capture by a Task-Specific Ionic Liquid. *Journal of the American Chemical Society*, 124(6): 926–927, February 2002.

[13] Dean Camper, Jason E. Bara, Douglas L. Gin, and Richard D. Noble. Room-Temperature Ionic LiquidAmine Solutions: Tunable Solvents for Efficient and Reversible Capture of CO_2. *Industrial & Engineering Chemistry Research*, 47(21):8496–8498, November 2008.

[14] Ryan P. Lively, Ronald R. Chance, B. T. Kelley, Harry W. Deckman, Jeffery H. Drese, Christopher W. Jones, and William J. Koros. Hollow Fiber Adsorbents for CO_2 Removal from Flue Gas. *Industrial & Engineering Chemistry Research*, 48(15):7314–7324, 2009.

[15] Imona C. Omole, Ryan T. Adams, Stephen J. Miller, and William J. Koros. Effects of CO_2 on a High Performance Hollow-Fiber Membrane for Natural Gas Purification. *Industrial & Engineering Chemistry Research*, 49(10):4887–4896, May 2010.

[16] John N. Maina, Sikiru A. Jimoh, and Margo Hosie. Implicit mechanistic role of the collagen, smooth muscle, and elastic tissue components in strengthening the air and blood capillaries of the avian lung. *Journal of Anatomy*, 217(5):597–608, November 2010.

[17] Leon M. Bellan, Sunil P. Singh, Peter W. Henderson, Teresa J. Porri, Harold G. Craighead, and Jason A. Spector. Fabrication of an artificial 3-dimensional vascular network using sacrificial sugar structures. *Soft Matter*, 5(7):1354, 2009.

[18] Leon M Bellan, Tatiana Kniazeva, Ernest S Kim, Alla A Epshteyn, Donald M Cropek, Robert Langer, and Jeffrey T Borenstein. Fabrication of a Hybrid Microfluidic System Incorporating both Lithographically Patterned Microchannels and a 3d FiberFormed Microfluidic Network. *Advanced Healthcare Materials*, 1(2):164–167, March 2012.

[19] Christopher J. Hansen, Willie Wu, Kathleen S. Toohey, Nancy R. Sottos, Scott R. White, and Jennifer A. Lewis. Self-Healing Materials with Interpenetrating Microvascular Networks. *Advanced Materials*, 21(41):4143–4147, November 2009.

[20] Jeffrey T. Borenstein, Eli J. Weinberg, Brian K. Orrick, Cathryn Sundback, Mohammad R. Kaazempur-Mofrad, and Joseph P. Vacanti. Microfabrication of Three-Dimensional Engineered Scaffolds. *Tissue Engineering*, 13(8):1837–1844, August 2007.

[21] Jen-Huang Huang, Jeongyun Kim, Nitin Agrawal, Arjun P. Sudarsan, Joseph E. Maxim, Arul Jayaraman, and Victor M. Ugaz. Rapid Fabrication of Bio-inspired 3D Microfluidic Vascular Networks. *Advanced Materials*, 21(35):3567–3571, July 2009.

[22] Michael Shin, Kant Matsuda, Osamu Ishii, Hidetomi Terai, Mohammed Kaazempur-Mofrad, Jeffrey Borenstein, Michael Detmar, and Joseph P. Vacanti. Endothelialized Networks with a Vascular Geometry in Microfabricated Poly(dimethyl siloxane). *Biomedical Microdevices*, 6(4):269–278, 2004.

[23] Brian D. Kozola, Lyle A. Shipton, Vinay K. Natrajan, Kenneth T. Christensen, and Scott R. White. Characterization of Active Cooling and Flow Distribution in Microvascular Polymers. *Journal of Intelligent Material Systems and Structures*, 21(12):1147–1156, August 2010.

[24] R. S. Trask, G. J. Williams, and I. P. Bond. Bioinspired Self-Healing of Advanced Composite Structures Using Hollow Glass Fibres. *Journal of The Royal Society Interface*, 4 (13):363–371, April 2007.

[25] Jiwon Lee, Jungwook Paek, and Jaeyoun Kim. Sucrose-based fabrication of 3D-networked, cylindrical microfluidic channel for rapid-prototyping of lab-on-a-chip and vaso-mimetic device. *Lab on a Chip*, 2012.

[26] Willie Wu, Adam DeConinck, and Jennifer A. Lewis. Omnidirectional Printing of 3D Microvascular Networks. *Advanced Materials*, 23(24):H178–H183, March 2011.

[27] Maxine A. McClain, Christopher T. Culbertson, Stephen C. Jacobson, Nancy L. Allbritton, Christopher E. Sims, and J. Michael Ramsey. Microfluidic Devices for the High-Throughput Chemical Analysis of Cells. *Analytical Chemistry*, 75(21):5646–5655, November 2003.

[28] Volker Hessel, Holger Lwe, and Friedhelm Schnfeld. Micromixersa review on passive and active mixing principles. *Chemical Engineering Science*, 60(8-9):2479–2501, April 2005.

[29] E Choban. Microfluidic fuel cell based on laminar flow. *Journal of Power Sources*, 128 (1):54–60, March 2004.

[30] A. Brunetti, F. Scura, G. Barbieri, and E. Drioli. Membrane technologies for CO_2 separation. *Journal of Membrane Science*, 359(1-2):115–125, September 2010.

[31] Geeta Mehta, Jay Lee, Wansik Cha, Yi-Chung Tung, Jennifer J. Linderman, and Shuichi Takayama. Hard Top Soft Bottom Microfluidic Devices for Cell Culture and Chemical Analysis. *Analytical Chemistry*, 81(10):3714–3722, May 2009.

[32] Aditya Balasubramanian, Robert Morhard, and Christopher J Bettinger. Shape-Memory Microfluidics. *Advanced Functional Materials*, 23(38):4832–4839, 2013.

[33] C. J. Bettinger, E. J. Weinberg, K. M. Kulig, J. P. Vacanti, Y. Wang, J. T. Borenstein, and R. Langer. Three-Dimensional Microfluidic Tissue-Engineering Scaffolds Using a Flexible Biodegradable Polymer. *Advanced Materials*, 18(2):165–169, January 2006.

[34] Christopher J. Hansen, Scott R. White, Nancy R. Sottos, and Jennifer A. Lewis. Accelerated Self-Healing Via Ternary Interpenetrating Microvascular Networks. *Advanced Functional Materials*, 21(22):4320–4326, November 2011.

[35] Du T. Nguyen, Y T. Leho, and Aaron P. Esser-Kahn. A three-dimensional microvascular gas exchange unit for carbon dioxide capture. *Lab Chip*, 12(7):1246–1250, March 2012.

[36] Du T. Nguyen, Y T. Leho, and Aaron P. Esser-Kahn. The Effect of Membrane Thickness on a Microvascular Gas Exchange Unit. *Advanced Functional Materials*, 23(1):100–106, January 2013.

[37] Ying Zheng, Peter W. Henderson, Nak Won Choi, Lawrence J. Bonassar, Jason A. Spector, and Abraham D. Stroock. Microstructured templates for directed growth and vascularization of soft tissue in vivo. *Biomaterials*, 32(23):5391–5401, August 2011.

[38] Leon M. Bellan, Matthew Pearsall, Donald M. Cropek, and Robert Langer. A 3D Interconnected Microchannel Network Formed in Gelatin by Sacrificial Shellac Microfibers. *Advanced Materials*, 24(38):5187–5191, October 2012.

[39] Nicolas Da Mota, David A. Finkelstein, Joseph D. Kirtland, Claudia A. Rodriguez, Abraham D. Stroock, and Hctor D. Abrua. Membraneless, Room-Temperature, Direct Borohydride/Cerium Fuel Cell with Power Density of Over 0.25 W/cm ^{2}. *Journal of the American Chemical Society*, 134(14):6076–6079, April 2012.

[40] J. Cooper McDonald and George M. Whitesides. Poly(dimethylsiloxane) as a Material for Fabricating Microfluidic Devices. *Accounts of Chemical Research*, 35(7):491–499, July 2002.

[41] Pei-Xue Jiang, Ming-Hong Fan, Guang-Shu Si, and Ze-Pei Ren. Thermalhydraulic performance of small scale micro-channel and porous-media heat-exchangers. *International Journal of Heat and Mass Transfer*, 44(5):1039–1051, March 2001.

[42] A. Khademhosseini, R. Langer, J. Borenstein, and J. P. Vacanti. Microscale technologies for tissue engineering and biology. *Proceedings of the National Academy of Sciences of the United States of America*, 103(8):2480–2487, February 2006. WOS:000235554900004.

[43] Dong Hyuck Kam and Jyoti Mazumder. Three-dimensional biomimetic microchannel network by laser direct writing. *Journal of Laser Applications*, 20(3):185, 2008.

[44] Matthew D. Determan, Dhruv C. Hoysall, and Srinivas Garimella. Heat- and Mass-Transfer Kinetics of Carbon Dioxide Capture Using Sorbent-Loaded Hollow Fibers. *Industrial & Engineering Chemistry Research*, 51(1):495–502, January 2012.

[45] Willie Wu, Christopher J. Hansen, Alejandro M. Aragn, Philippe H. Geubelle, Scott R. White, and Jennifer A. Lewis. Direct-write assembly of biomimetic microvascular networks for efficient fluid transport. *Soft Matter*, 6(4):739–742, 2010.

[46] Dongliang Wang, K Li, and W.K Teo. Preparation and characterization of polyvinylidene fluoride (PVDF) hollow fiber membranes. *Journal of Membrane Science*, 163(2): 211–220, November 1999.

[47] Dominic T Clausi and William J Koros. Formation of defect-free polyimide hollow fiber membranes for gas separations. *Journal of Membrane Science*, 167(1):79–89, March 2000.

[48] Gian Luca Morini. Single-phase convective heat transfer in microchannels: a review of experimental results. *International Journal of Thermal Sciences*, 43(7):631–651, July 2004.

[49] Poh-Seng Lee, Suresh V. Garimella, and Dong Liu. Investigation of heat transfer in rectangular microchannels. *International Journal of Heat and Mass Transfer*, 48(9): 1688–1704, April 2005.

[50] Weilin Qu and Issam Mudawar. Analysis of three-dimensional heat transfer in micro-channel heat sinks. *International Journal of Heat and Mass Transfer*, 45(19):3973–3985, September 2002.

[51] Sung-Min Kim and Issam Mudawar. Analytical heat diffusion models for different micro-channel heat sink cross-sectional geometries. *International Journal of Heat and Mass Transfer*, 53(19-20):4002–4016, September 2010.

[52] Oara Neumann, Alexander S. Urban, Jared Day, Surbhi Lal, Peter Nordlander, and Naomi J. Halas. Solar Vapor Generation Enabled by Nanoparticles. *ACS Nano*, 7(1): 42–49, January 2013.

[53] Oara Neumann, Curtis Feronti, Albert D. Neumann, Anjie Dong, Kevin Schell, Benjamin Lu, Eric Kim, Mary Quinn, Shea Thompson, Nathaniel Grady, Peter Nordlander, Maria Oden, and Naomi J. Halas. Compact solar autoclave based on steam generation using broadband light-harvesting nanoparticles. *Proceedings of the National Academy of Sciences*, 110(29):11677–11681, July 2013.

Chapter 2

Microvascular Carbon Capture

2.1 Background

The microvascular gas exchange units were fabricated using the Vaporization of a Sacrificial Component (VaSC) technique to create a three-dimensional patterned micro-channel structure.[28] This technique constructs arrays of micro-scale hollow channels within a polymer resin without lithography. The fabrication process is highly modular and allows for a wide range of both membrane materials and capture fluids. In this study, the units were composed of a hexagonal arrangement of hollow channels embedded within polydimethylsiloxane (PDMS) as a model membrane. In each unit, the central channel began with a diameter of 300 μm while the outer channels had diameters of 200 μm. The separations between the central and outer channels started as 50 μm (Figure 2.1). This initial structure provided a specific surface area of 2267 m^2 m^{-3}. As a model capture-fluid, the industrial standard gas scrubbing liquid, 30% MEA in water, was loaded into the outer channels as CO_2 was flowed through the central channel. Upon entering the material, CO_2 permeated through the PDMS membrane until it reached the surface of the capture fluid channel. The

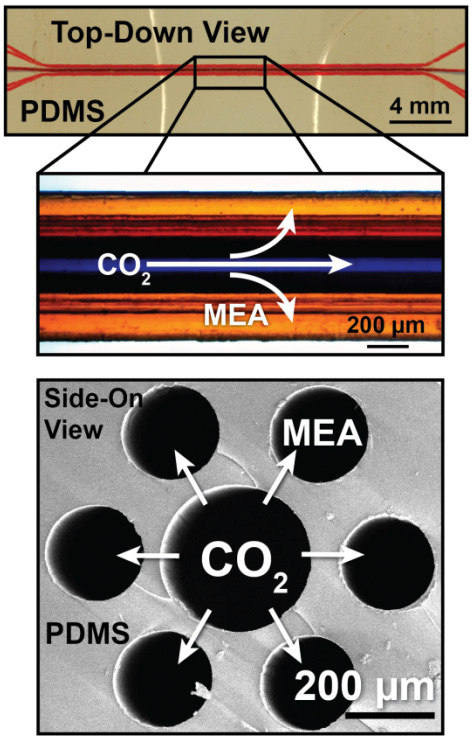

Figure 2.1: A representative gas exchange unit. Optical microscope and cross-sectional SEM images of a microvascular gas exchange unit composed of a central channel with a diameter of 300 μm and outer channels with diameters of 200 μm. The inter-channel distance is initially 50 μm. Channels are separated in a second interface to load the channels with fluid and gas more easily.

CO_2 then reacted with the MEA at the surface and was subsequently retained as carbamic acid in the outer channels, completing the capture process.

In our microvascular gas exchange system, the inter-channel distance was a critical parameter for controlling the permeability of CO_2 between the gas channel and the capture channel. A chemical etching technique was used to precisely modify the inter-channel distance of a gas exchange unit as the distances dictated the thickness of the membrane.[29] A tetrabutylammonium fluoride (TBAF) in dimethylformamide (DMF) solution (3:1; vol:vol; DMF:75% wt. TBAF in water, hereafter referred to as the etching solution) was used to depolymerize the PDMS membrane of the exchange units (Figure 2.2).

The fluoride anions in TBAF attacked the silicon centers of PDMS, forming Si-F bonds.

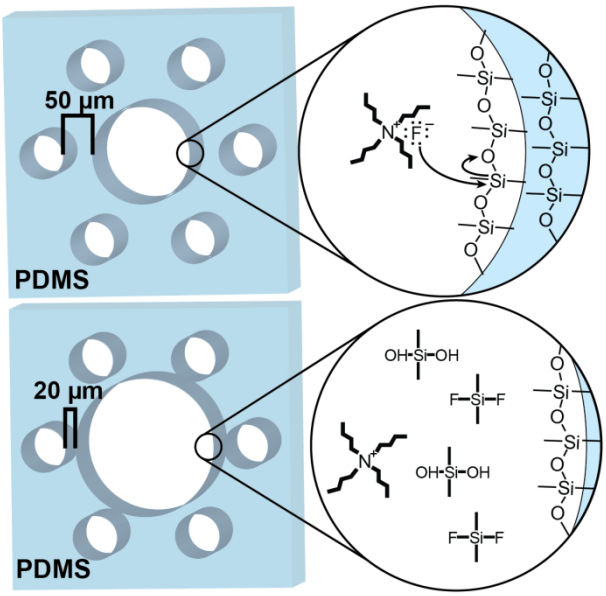

Figure 2.2: A schematic of the etching process. As TBAF flows through the central channel, the fluoride anions PDMS. Through this process, the polymer sidewall is rapidly depolymerized. The products are cleared from the system as new etching solution is continually flowed into the channel. By etching the walls of the central channel, the inter-channel distance is decreased between the central and outer channels.

The smooth laminar flow of the etching solution provided precise control over the etching rate. Upon removal of the PDMS, the central channel diameter increased causing the inter-channel distance, or membrane thickness, to decrease. We confirmed the etching process by imaging horizontal and vertical cross-sections of the micro-channels with a scanning electron microscope (SEM) (Figure 2.3). With this etching strategy, we were able to systematically study the relationship between membrane thicknesses and CO_2 capture rates. To simulate the gas exchange units, we have developed a computational finite element model which combines fluid flows, reaction rates, and diffusion rates. This model was able to accurately predict the capture rates in units with membrane thicknesses above 25 μm, but a divergence between the experimental results and the model occurred below such thicknesses. We further explore the divergence in this report.

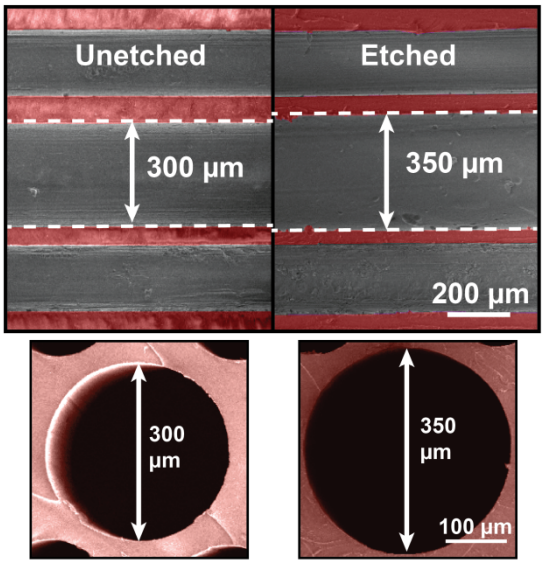

Figure 2.3: Visualization of etching. SEM images of a gas exchange unit taken before and after etching 50 μm of PDMS from the central microchannel. Membranes are false-colored for visual clarity. Both horizontal and vertical cross sections were imaged. The inter-channel distance is decreased by 25 μm and results in higher mass transfer rates.

2.2 Results and Discussion

To determine the etching rate of the process, samples were created with 500, 300, and 200 μm diameter channels. The etching solution was flowed through the channels at a constant rate of 0.5 mL min^{-1} for 10 minutes. The channels were flushed with DMF at the same flow rate for 2 minutes to clear any remaining etching solution. A final rinse with 5 mL of DI water was then performed. While this resulted in different flow velocities for each channel due to the different channel radii, it provided an accessible calibration of the etching rate. The channel diameters were measured between each trial by imaging channels loaded with red dye for visualization. The channel diameters were computed with precise averages and errors using distance detection algorithms on the images across the entire length of the channels (Appendix A.1). The overall etching rate for each initial channel diameter was calculated after multiple trials (Figure 2.4a). For the 200 and 300 μm channels, the etching rates were similar at ˜1 μm min^{-1} while the etching rate for the larger 500 μm channel was found to be ˜2 μm min-1. Although only 300 μm diameter channels were etched in this

a)

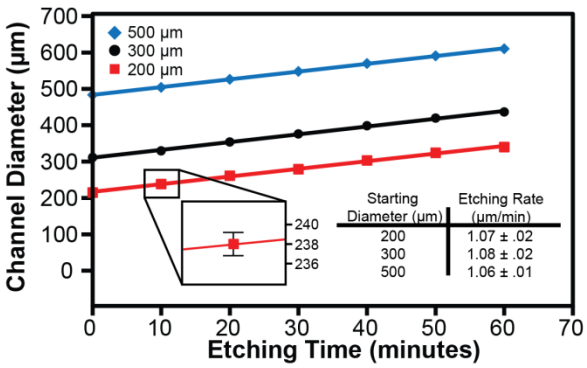

b)

Flow Rate (mL min $^{-1}$)	Etching Rate (µm min^{-1})
2.00	1.07 ± .03
1.00	0.97 ± .02
0.50	1.06 ± .01
0.25	0.85 ± .03

Figure 2.4: Etching rate calibration. a) Etching rates for 500, 300, and 200 μm channel diameters (blue, black, and red respectively) with an etching solution flow rate of 0.5 mL min^{-1}. An enhanced set of a 200 μm channel is shown to illustrate error bars. b) Etching rates for varying etching solution flow rates in a 500 μm diameter channel. An increase in etching rate occurs as the flow rate increases.

study for the purpose of capturing CO_2, further optimization of the gas exchange units may use other initial channel diameters. We also sought to understand the relationship between etching solution flow rates and etching rates. Samples were created with 500 μm diameter channels and etched at varying flow rates of etching solution for 5 minutes. The same flushing procedure with DMF and DI water was then performed on the samples. It was found that by increasing the flow rate, there was a slight increase of the etching rate which then levels off (Figure 2.4b).

We believe this is due to the saturation of the fluoride ions at the surfaces of the channels above flow rates of 0.5 mL min^{-1}. Faster flow rates required more overall solution and provided negligible increases in the etching rate. This resulted in the use of lower flow rates to reduce the overall consumption of the etching solution.

With the calibration of the etching procedure prepared, we then sought to explore the effects of decreasing the inter-channel distances on the ability of gas exchange units to capture CO_2. To determine the mass transfer rate of the units, a colorimetric technique was used. CO_2 was flowed through the central channel at a rate of 1 cm^3 min^{-1} while a solution of MEA (30:70, vol:vol, MEA:DI H2O) was loaded into the outer channels. As MEA captures CO_2, the solution becomes more acidic (˜pH 12 to ˜8). This reaction was indirectly visualized by adding phenolphthalein, a pH sensitive dye that shifts color from red to colorless (red to light pink in bulk) once the channel was saturated with CO_2 (6 mg dye/mL MEA solution).[30] Defining the saturation time as 50% color change, the shift occurred at ˜9 wt % CO_2 (˜2.2M carbamic acid) which was determined through UV-Vis spectroscopy (Appendix A.2). This method allowed us to observe the reaction of CO_2 with MEA on an optical microscope in real time. Combining the saturation times with the saturation concentration, the average mass transfer rates could then be calculated.

The microvascular gas exchange units were also modeled using the COMSOL Multiphysics simulation software. The model uses a combination of fluid flow and diffuse species transport physics to simulate the system. Several assumptions and parameters were used to create the model, including diffusion coefficients and reaction rates (Table 2.1). A time-dependent model was then created, simulating the flow and diffusion of CO_2 through a gas exchange unit as well as its reaction with MEA once it reached the outer channels. By averaging the concentration of carbamic acid over the outer channel volumes, we used the model to predict the saturation times for various inter-channel distances (Figure 2.5). The model saturation times were defined as the time to reach 2.2 M carbamic acid and could then be compared with the experimental data. A linear trend of decreasing saturation times with decreasing channel separations was predicted. Using this colorimetric technique, we determined the relationship between inter-channel distances and gas exchange rates of our microvascular units with 100% CO_2. Between each trial, the central channel was etched for 4 minutes with an etching solution flow rate of 0.5 mL min^{-1} resulting in the inter-channel distance

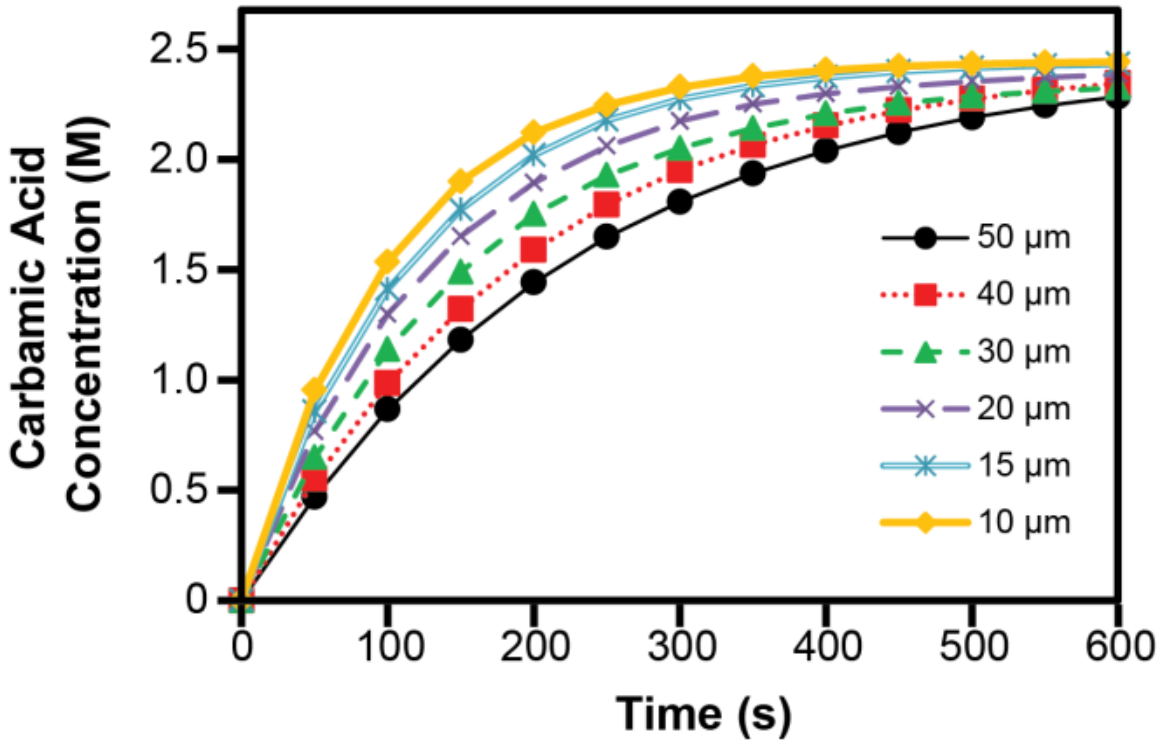

Figure 2.5: COMSOL model simulation of CO_2 capture in gas exchange units with various membrane thicknesses. As CO_2 diffuses into the outer channels, a reaction occurs with MEA, forming carbamic acid which is modeled by the software. The time to reach a concentration of ˜2200 mol m^{-3} is considered the saturation time.

decreasing by ˜4 μm per trial. The three-dimensional arrangement of channels interfered with the two-dimensional optical imaging of channels and resulted in large errors in the channel separation measurements. To reduce this error, MEA without dye was loaded into the upper and lower channels to increase transparency while the two flanking channels were loaded with dyed MEA for both the separation distance and saturation time measurements. The minimum membrane thickness reached was 21 μm and resulted in a specific surface area of 2706 m^2 m^{-3}. As expected, the saturation times decreased when the inter-channel distances decreased (Fig. 6a). With thinner membranes, CO_2 diffused to the outer channels more rapidly. The initial gas exchange rate was found to be 3.59 $\pm$ 0.19 mol m^{-2} hr^{-1} for an inter-channel distance of 45.7 μm. For pure CO_2, the fastest mass transfer rate was found to be 6.86 $\pm$ 0.43 mol m^{-2} hr^{-1} which was obtained for an inter-channel distance of 20.8 μm. By etching the central channel to produce smaller inter-channel distances, the mass transfer rate increased by 91%.

The experiment was repeated with a flue gas simulant of 10 vol% CO_2, balanced with N_2, to determine if the same trend would be found with lower concentrations of CO_2. The model again predicted a linear trend of decreasing saturation times with decreasing inter-channel distances, and with saturation times increasing by a factor of 10 in comparison to using 100% CO_2. Again, a general decrease in saturation time with a decrease in membrane thickness was found (Fig. 6b).

The initial inter-channel distance of 42.7 μm resulted in a mass transfer rate of 0.30 $\pm$ 0.02 mol m^{-2} hr^{-1}. At the lowest inter-channel distance of 20.8 μm, a mass transfer rate of 0.78 $\pm$ 0.03 mol m-2 hr-1 was obtained, increasing by 160%. While this absolute rate may be lower in comparison to other devices such as hollow fiber membrane contactors (˜2 mol m^{-2} hr^{-1}), the rates for other such devices include flowing rather than stationary MEA and slightly higher concentrations of CO_2 (˜14%).[31] This result suggests the intriguing possibility that creating gas exchange units with inter-channel distances less than 20 μm could improve gas exchange

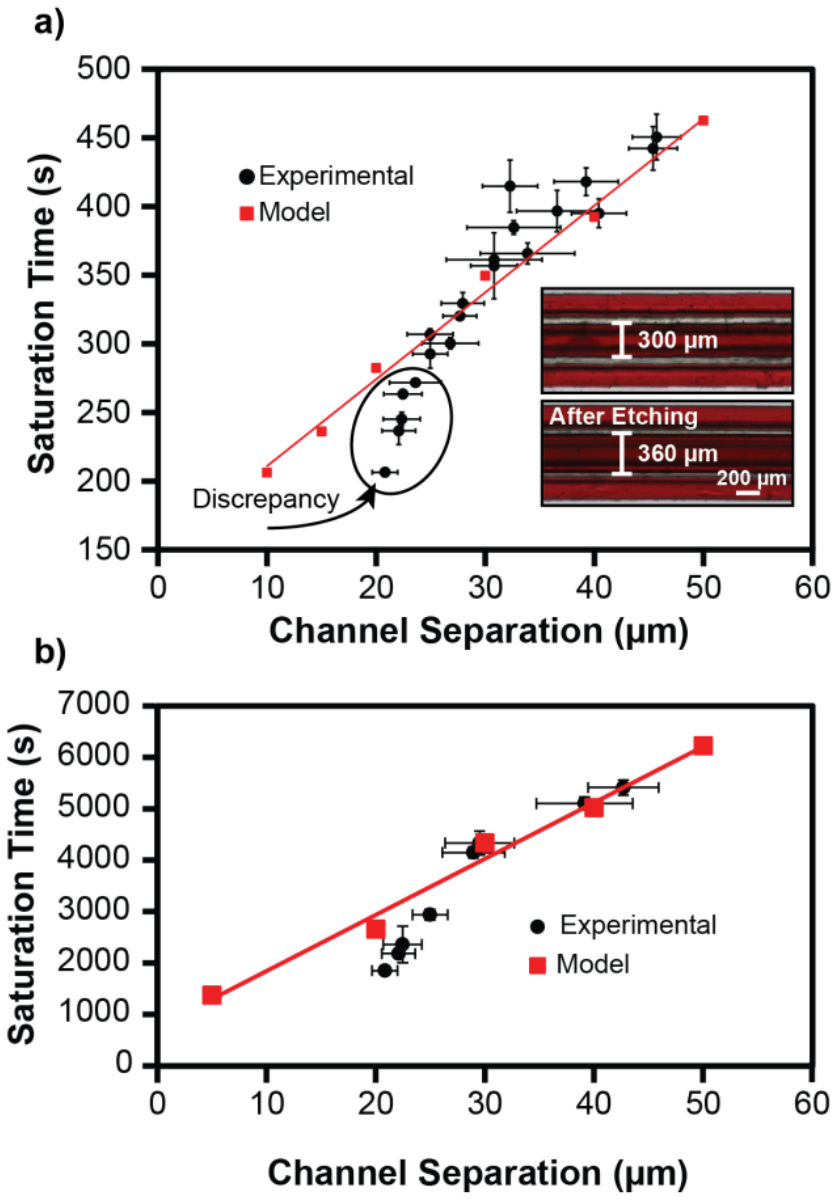

Figure 2.6: The effect of membrane thickness on saturation times. a) Saturation times for 100% CO_2. Inset is the channel before and after the etching trials were complete. Red dye is loaded on the central and flanking outer channels while the upper and lower channels are loaded with water for visual clarity. b) Saturation times for 10% vol CO_2 balanced with N_2. In both cases, as the membrane thickness decreases, the saturation times also decrease. Initially this trend is linear, but then accelerates and diverges from the model as the thickness decreases under 25 μm. The divergence is less prominent with the lower concentration of CO_2.

rates more dramatically. However, we believe this may require a new approach to overall fabrication. While the general trends with pure and 10% CO_2 matched our predictions, the linear trends expected by the model did not match with the experimental results. Instead, the trends were only linear at inter-channel distances above ˜25 μm. When the distances were less than 25 μm, the saturation times decreased at a faster rate and diverged from the model. We attempted to decrease the inter-channel distance below 20 μm, but were hindered by the leaking of capture fluid between the outer and central channels at various points along the channels. We examined what effects these leak points would have on the mass transfer rates to determine if they could cause the divergences. Leaking might be explained by the presence of micro-dents in the material prior to etching. The presence of these micro-dents creates membrane regions of smaller thicknesses. CO_2 could permeate through the membrane more rapidly at these points and then diffuse through the MEA solution resulting in a more rapid saturation time.

To understand if the divergences from the model at smaller inter-channel distances were caused by micro-dents, we first attempted to model the system with simulated micro-dents. The micro-dents were simulated with cylindrical portions with 180 μm radii added to the central channel of the model with a 50 μm inter-channel distance resulting in segments with closer separations. From the results of the model, the saturation time of a gas exchange unit with the micro-dents decreased by 25 s in comparison to the model with smooth channels (Figure 2.7).

While this accounted for some of the discrepancy, the model did not fully agree with experiments. We then attempted to introduce micro-dents experimentally to examine the resulting decrease in saturation time. The micro-dents were created by joining extra PLA to the central channel using 25 μm fibers and TFE. With these artificially created micro-dents, the saturation time of a gas exchange unit with a 44 μm inter-channel distance improved by ˜90 s. This rate is comparable to the divergence between the model and experimental satura-

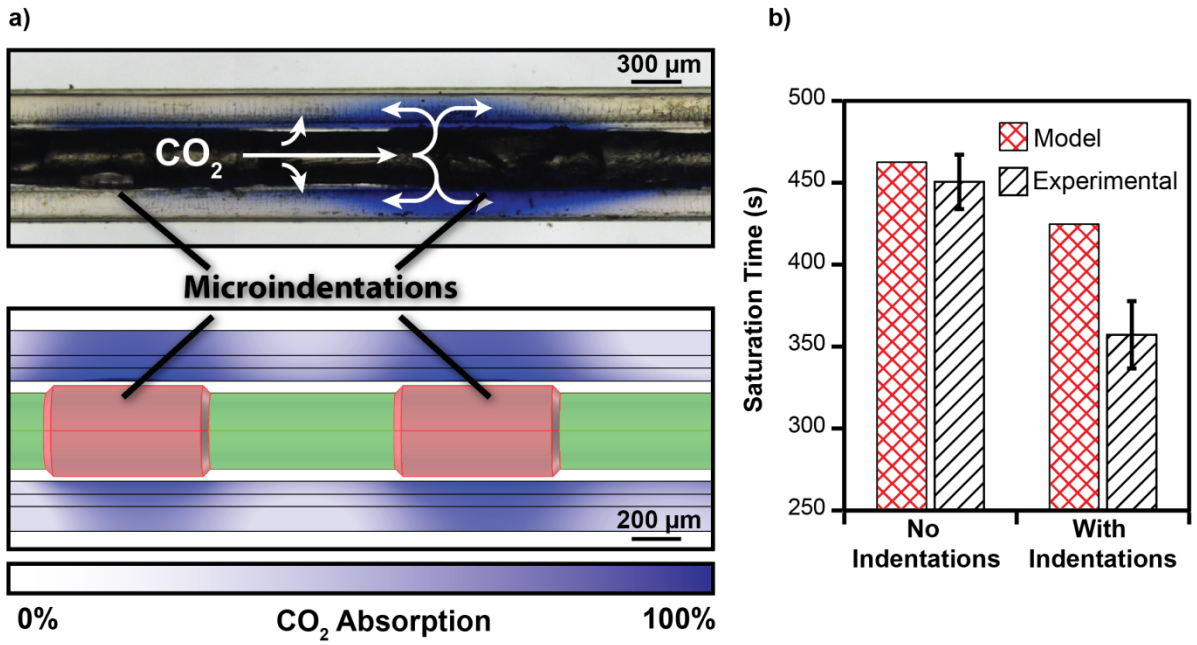

Figure 2.7: The effect of inducing micro-dents on the central channel. a) Experimental and model gas exchange units with micro-dents. Micro-dents are added to the model through additional cylindrical segments with larger radii than the central channel. Experimental micro-dents are added by fusing 25 μm PLA fibers to the central channel resulting in a rougher surface. b) A graph of saturation times with and without dents. In both cases with the microdents, a decrease in saturation time is observed. Only with the experimental data does this decrease in saturation time match the divergence from the model seen at low channel separations.

tion times at 20 μm separations. This result suggests that the micro-dents improve the mass transfer rates of a gas exchange unit and account for the divergences found previously. It also implies that smooth micro-channels are not necessary to promote enhanced gas absorption rates in our microvascular gas exchange units.

2.3 Experimental

2.3.1 Materials

Monoethanolamine (99%, MEA), phenolphthalein, methyl blue, tin (II) oxalate (98%) tetrabutylammonium fluoride solution (75 wt % in water, TBAF), and N,N-Dimethylformamide (99.8%, DMF) were purchased from Sigma-Aldrich. Sylgard 184 silicone elastomer kit (PDMS) was purchased from Dow Corning. Disperbyk-130 was purchased from BYK Additives & Instruments. Trifluoroethanol (TFE) was purchased from Halogen Inc. Poly(lactic) acid (PLA) fibers were provided by Teijin Monofilament. Preparation of Fibers for Exchange Unit Fabrication: PLA fibers were infused with tin (II) oxalate to lower its depolymerization temperature from 280 °C to 200 °C. A 800 mL treatment solution was created (400 mL deionized water, 400 mL trifluoroethanol, 50 g tin oxalate, 20 g DISPERBYK-130, 0.5 g malachite green) to infuse the tin oxalate within the fibers and to dye the fibers for visual clarity. Fibers were wound around a custom spindle and placed within the solution. The solution with the fibers was agitated by spinning the spindle at 300 RPM for 48 hours at room temperature. The fibers were then removed from the solution and dried in air at room temperature for 24 hours.

2.3.2 Gas Exchange Unit Fabrication

Gas exchange units were created using the Vaporization of a Sacrificial Component (VaSC) technique. Poly(lactic) acid (PLA) fibers were infused with a tin (II) oxalate (SnOx) catalyst. PDMS was created using mixtures of the Sylgard 184 silicone elastomer base and curing agent with a 10:1 ratio between base and curing agent. The mixture was then degassed using a rough vacuum pump and glass bell jar for 15 minutes. The fibers were strung through two laser-cut brass plates containing a hexagonal pattern. The plates were placed onto a mold box with the fibers tensioned on either side to create a set of parallel fibers in a hexagonal arrangement within the mold box. The mold box was then filled with PDMS and cured at 65 °C for 1 hour. A second stage of molding with PDMS was performed to separate the channels from the hexagonal pattern and allow for easier loading of channels. The vascular preforms were heated to 210 °C under vacuum to vaporize and evacuate the fibers embedded within the PDMS resin resulting in the hexagonal arrangement of hollow channels.

2.3.3 Creating Micro-dents

A procedure similar to the fabrication of a normal gas exchange unit was followed. After the fibers were strung through the patterning plates, but before placement onto the mold box and tensioning, the micro-dents were added. Small loops of 25 μm PLA fibers were wrapped around the 300 μm central fiber. Single drops of TFE were added to the loops to meld the 25 μm fibers onto the central fiber. The remaining TFE was then dried in air and resulted in a central fiber with increased surface roughness to simulate the micro-dents.

2.3.4 COMSOL Model

To model the system, the Laminar Flow and Transport of Dilute Species modules were coupled to simulate the flow of CO_2, diffusion of CO_2, and reaction of CO_2 with MEA. Diffusion coefficients of 1.6e-5 m^2 s^{-1}, 1.51e-9 m^2 s^{-1}, and 7.08e-10 m^2 s^{-1} for CO_2 in air, water, and PDMS respectively were used to determine the transport properties of the model.[33–35] The densities and dynamic viscosities of N_2 and CO_2 were used to determine the flow properties of 10 vol% CO_2 and 100% CO_2 respectively. The reaction rate between CO_2 and MEA was approximated using a 1st order reaction and calculated as r = 6550*[MEA] where r is the rate in mol m^{-3} s^{-1}.[36–39] Time dependent simulations were run using a generalized alpha time-stepping method.

The COMSOL Multiphysics program was used to create models of the gas exchange units. The physical geometries of the units were generated using 8 mm long cylinders arranged in a hexagonal pattern within a surrounding box with dimensions of $4 \times 4 \times 8$ mm. The central cylinder had a diameter of 300 μm and the outer cylinders had diameters of 200 μm. The cylinders corresponded to the gas and fluid channels while the surrounding box represented the PDMS. Meshes composed of tetrahedrons were formed to approximate the physical geometries of the systems and allowed for numerical calculations within the model.

The program initially solved for the steady state velocities and pressures in the fluid and gas channels, assuming laminar flow. The solution parameters from the fluid and gas flows were then used to determine the time-dependent solution to the transportation of species within the model gas exchange unit. The time-dependent solver was set to a generalized alpha time stepping method rather than a backward differentiation formula (BFD) time stepping method. BFD methods approximate the integration of ordinary differential equations numerically by approximating the derivatives of the functions from previously computed times. Generalized alpha time stepping methods are similar, but further approximate the solutions

Physics Module	**Location**	**Parameter**	**Value**
Laminar Flow	Central Channel	Laminar inflow average velocity	0.059 m/s
		Entrance length	300 μm
	Outer Channels	Inflow Pressure	0 Pa
Transport of Diluted Species (All)	All	Velocity field	(spf/fp1)
Transport of Diluted Species (CO_2)	Central Channel	Diffusion coefficient	16 mm^2/s
		Inflow	45 mol/m^3 (4500 for 100% CO_2)
	Outer Channels	Diffusion coefficient	1.51e-9 m^2/s
		Inflow	0 mol/m^3
		Reaction equation	-6550*[CO_2]
	PDMS	Diffusion coefficient	7.08e-10 m^2/s
Transport of Diluted Species (MEA)	Outer Channels	Diffusion coefficient	9.32e-10 m^2/s
		Initial concentration	4900 mol/m^3
		Reaction equation	-6550*2*[CO_2][MEA]
Transport of Diluted Species (MEA-COOH-)	Outer Channels	Diffusion coefficient	9.32e-10 m^2/s
		Initial concentration	0 mol/m^3
		Reaction equation	6550*[CO_2][MEA]

Table 2.1: Coefficients and parameters used in the simulation model

through a second-order expansion multiplied by an alpha coefficient. This results in a faster computation of the model.

2.3.5 Microscopy

Optical microscopy images were taken with a Zeiss Axio Observer.A1 Microscope at a 5X objective for determining inter-channel distances and a 2.5X objective for determining saturation times. Tiled images were taken over the entire unit as water dyed with methyl blue was loaded into the central and flanking outer channels while water without dye was loaded into the upper and lower outer channels to determine the inter-channel distances. To determine the saturation times, time-lapsed images with four second intervals were taken on marked central positions along the length of the gas exchange units. Regions of interest were made along the outer channels to quantify the image data within the regions. The average hue within the regions were found and normalized from the initial to final hue values. The time to reach 50% hue change was defined as the saturation time.

Scanning Electron Microscopy: SEM images were taken on a FEI Quanta FIB system (Oxford Instruments) with currents ranging from 1.06 pA to 4.74 pA and voltages ranging from 1.00 kV to 2.00 kV.

Bibliography

[1] P. Friedlingstein, R. A. Houghton, G. Marland, J. Hackler, T. A. Boden, T. J. Conway, J. G. Canadell, M. R. Raupach, P. Ciais, and C. Le Qur. Update on CO_2 emissions. *Nature Geoscience*, 3(12):811–812, November 2010.

[2] Dieter Lüthi, Martine Le Floch, Bernhard Bereiter, Thomas Blunier, Jean-Marc Barnola, Urs Siegenthaler, Dominique Raynaud, Jean Jouzel, Hubertus Fischer, Kenji Kawamura, and Thomas F. Stocker. High-resolution carbon dioxide concentration record 650,000800,000years before present. *Nature*, 453(7193):379–382, May 2008.

[3] DOE. *Annual Energy Outlook, 2011 with Projections to 2035*, 2011.

[4] Howard J. Herzog. Peer Reviewed: What Future for Carbon Capture and Sequestration? *Environmental Science & Technology*, 35(7):148A–153A, April 2001.

[5] Timothy J. Skone. Carbon Dioxide Capture from Existing Coal-Fired Power Plants. Technical Report DOE/NETL-401/110907, U.S. Department of Energy, November 2007.

[6] J. P. Ciferno, T. E. Fout, A. P. Jones, and J. T. Murphy. Capturing Carbon from Existing Coal-Fired Power Plants | AIChE. *Chemical Engineering Progress*, 105:33–41, April 2009.

[7] David Britt, Hiroyasu Furukawa, Bo Wang, T. Grant Glover, and Omar M. Yaghi. Highly efficient separation of carbon dioxide by a metal-organic framework replete with open metal sites. *Proceedings of the National Academy of Sciences*, 106(49):20637 – 20640, December 2009.

[8] Hailian Li, Mohamed Eddaoudi, M. O'Keeffe, and O. M. Yaghi. Design and synthesis of an exceptionally stable and highly porous metal-organic framework. *Nature*, 402(6759): 276–279, November 1999.

[9] Jos D. Figueroa, Timothy Fout, Sean Plasynski, Howard McIlvried, and Rameshwar D. Srivastava. Advances in CO_2 capture technology–The U.S. Department of Energy's Carbon Sequestration Program. *International Journal of Greenhouse Gas Control*, 2 (1):9–20, January 2008.

[10] R Franchi, P Harlick, and A Sayari. A high capacity, water tolerant adsorbent for CO_2: diethanolamine supported on pore-expanded MCM-41. In *Studies in Surface Science and Catalysis*, volume 156, pages 879–886. Elsevier, 2005.

[11] Rajesh A. Khatri, Steven S. C. Chuang, Yee Soong, and McMahan Gray. Thermal and Chemical Stability of Regenerable Solid Amine Sorbent for CO_2 Capture. *Energy & Fuels*, 20(4):1514–1520, July 2006.

[12] Eleanor D. Bates, Rebecca D. Mayton, Ioanna Ntai, and James H. Davis. CO_2 Capture by a Task-Specific Ionic Liquid. *Journal of the American Chemical Society*, 124(6): 926–927, February 2002.

[13] Dean Camper, Jason E. Bara, Douglas L. Gin, and Richard D. Noble. Room-Temperature Ionic LiquidAmine Solutions: Tunable Solvents for Efficient and Reversible Capture of CO_2. *Industrial & Engineering Chemistry Research*, 47(21):8496–8498, November 2008.

[14] Ryan P. Lively, Ronald R. Chance, B. T. Kelley, Harry W. Deckman, Jeffery H. Drese, Christopher W. Jones, and William J. Koros. Hollow Fiber Adsorbents for CO_2 Removal from Flue Gas. *Industrial & Engineering Chemistry Research*, 48(15):7314–7324, 2009.

[15] Imona C. Omole, Ryan T. Adams, Stephen J. Miller, and William J. Koros. Effects of CO_2 on a High Performance Hollow-Fiber Membrane for Natural Gas Purification. *Industrial & Engineering Chemistry Research*, 49(10):4887–4896, May 2010.

[16] John N. Maina, Sikiru A. Jimoh, and Margo Hosie. Implicit mechanistic role of the collagen, smooth muscle, and elastic tissue components in strengthening the air and

blood capillaries of the avian lung. *Journal of Anatomy*, 217(5):597–608, November 2010.

[17] Leon M. Bellan, Sunil P. Singh, Peter W. Henderson, Teresa J. Porri, Harold G. Craighead, and Jason A. Spector. Fabrication of an artificial 3-dimensional vascular network using sacrificial sugar structures. *Soft Matter*, 5(7):1354, 2009.

[18] Leon M Bellan, Tatiana Kniazeva, Ernest S Kim, Alla A Epshteyn, Donald M Cropek, Robert Langer, and Jeffrey T Borenstein. Fabrication of a Hybrid Microfluidic System Incorporating both Lithographically Patterned Microchannels and a 3d FiberFormed Microfluidic Network. *Advanced Healthcare Materials*, 1(2):164–167, March 2012.

[19] Christopher J. Hansen, Willie Wu, Kathleen S. Toohey, Nancy R. Sottos, Scott R. White, and Jennifer A. Lewis. Self-Healing Materials with Interpenetrating Microvascular Networks. *Advanced Materials*, 21(41):4143–4147, November 2009.

[20] Jeffrey T. Borenstein, Eli J. Weinberg, Brian K. Orrick, Cathryn Sundback, Mohammad R. Kaazempur-Mofrad, and Joseph P. Vacanti. Microfabrication of Three-Dimensional Engineered Scaffolds. *Tissue Engineering*, 13(8):1837–1844, August 2007.

[21] Jen-Huang Huang, Jeongyun Kim, Nitin Agrawal, Arjun P. Sudarsan, Joseph E. Maxim, Arul Jayaraman, and Victor M. Ugaz. Rapid Fabrication of Bio-inspired 3D Microfluidic Vascular Networks. *Advanced Materials*, 21(35):3567–3571, July 2009.

[22] Michael Shin, Kant Matsuda, Osamu Ishii, Hidetomi Terai, Mohammed Kaazempur-Mofrad, Jeffrey Borenstein, Michael Detmar, and Joseph P. Vacanti. Endothelialized Networks with a Vascular Geometry in Microfabricated Poly(dimethyl siloxane). *Biomedical Microdevices*, 6(4):269–278, 2004.

[23] Brian D. Kozola, Lyle A. Shipton, Vinay K. Natrajan, Kenneth T. Christensen, and Scott R. White. Characterization of Active Cooling and Flow Distribution in Microvas-

cular Polymers. *Journal of Intelligent Material Systems and Structures*, 21(12):1147–1156, August 2010.

[24] R. S. Trask, G. J. Williams, and I. P. Bond. Bioinspired Self-Healing of Advanced Composite Structures Using Hollow Glass Fibres. *Journal of The Royal Society Interface*, 4 (13):363–371, April 2007.

[25] Jiwon Lee, Jungwook Paek, and Jaeyoun Kim. Sucrose-based fabrication of 3D-networked, cylindrical microfluidic channel for rapid-prototyping of lab-on-a-chip and vaso-mimetic device. *Lab on a Chip*, 2012.

[26] Willie Wu, Adam DeConinck, and Jennifer A. Lewis. Omnidirectional Printing of 3D Microvascular Networks. *Advanced Materials*, 23(24):H178–H183, March 2011.

[27] Du T. Nguyen, Y T. Leho, and Aaron P. Esser-Kahn. A three-dimensional microvascular gas exchange unit for carbon dioxide capture. *Lab Chip*, 12(7):1246–1250, March 2012.

[28] Aaron P EsserKahn, Piyush R Thakre, Hefei Dong, Jason F Patrick, Vitalii K VlaskoVlasov, Nancy R Sottos, Jeffrey S Moore, and Scott R White. ThreeDimensional Microvascular FiberReinforced Composites. *Advanced Materials*, 23(32):3654–3658, August 2011.

[29] S. Takayama, E. Ostuni, X. Qian, J. C McDonald, X. Jiang, P. LeDuc, M. H Wu, D. E Ingber, and G. M Whitesides. Topographical Micropatterning of Poly(dimethylsiloxane) Using Laminar Flows of Liquids in Capillaries. *Advanced Materials*, 13(8):570–574, April 2001.

[30] Ram Wasudeo Sabnis. *Handbook of acid-base indicators*. CRC Press, October 2007.

[31] Shui-ping Yan, Meng-Xiang Fang, Wei-Feng Zhang, Shu-Yuan Wang, Zhi-Kang Xu, Zhong-Yang Luo, and Ke-Fa Cen. Experimental study on the separation of CO_2 from

flue gas using hollow fiber membrane contactors without wetting. *Fuel Processing Technology*, 88(5):501–511, May 2007.

[32] Kathleen S. Toohey, Nancy R. Sottos, Jennifer A. Lewis, Jeffrey S. Moore, and Scott R. White. Self-healing materials with microvascular networks. *Nature Materials*, 6(8): 581–585, June 2007.

[33] D. T. Pritchard and J. A. Currie. Diffusion of coefficients of carbon dioxide, nitrous oxide, ethylene and ethane in air and their measurement. *Journal of Soil Science*, 33 (2):175–184, June 1982.

[34] A. Tamimi, Edward B. Rinker, and Orville C. Sandall. Diffusion Coefficients for Hydrogen Sulfide, Carbon Dioxide, and Nitrous Oxide in Water over the Temperature Range 293-368 K. *Journal of Chemical & Engineering Data*, 39(2):330–332, April 1994.

[35] T. C. Merkel, V. I. Bondar, K. Nagai, B. D. Freeman, and I. Pinnau. Gas sorption, diffusion, and permeation in poly(dimethylsiloxane). *Journal of Polymer Science Part B: Polymer Physics*, 38(3):415–434, 2000.

[36] Roco Maceiras, Estrella lvarez, and M. ngeles Cancela. Effect of temperature on carbon dioxide absorption in monoethanolamine solutions. *Chemical Engineering Journal*, 138 (1-3):295–300, May 2008.

[37] Jorge M. Plaza, David Van Wagener, and Gary T. Rochelle. Modeling CO_2 capture with aqueous monoethanolamine. *Energy Procedia*, 1(1):1171–1178, February 2009.

[38] P.M.M. Blauwhoff, G.F. Versteeg, and W.P.M. Van Swaaij. A study on the reaction between CO_2 and alkanolamines in aqueous solutions. *Chemical Engineering Science*, 38(9):1411–1429, 1983.

[39] Roongrat Sakwattanapong, Adisorn Aroonwilas, and Amornvadee Veawab. Reaction

rate of CO_2 in aqueous MEA-AMP solution: Experiment and modeling. *Energy Procedia*, 1:217–224, February 2009.

Chapter 3

Close Packing Structure

3.1 Background

Alongside our artificial exchangers, biological systems developed micro-patterned exchange designs for much of evolutionary history.[29–32] Evolution repeatedly converged on vascular exchange units composed of arrays of circular channels, known as "rete mirabile". Remarkably, in the 1970s, it was discovered that these bio-exchange designs are the exact solutions to the compact, packing of circles of two diameters.[31] Despite strong interest in micro-exchangers and their many applications, very little work examines biologically inspired systems composed of the close-packed circular microchannels. Here we report the synthesis and study of the transfer characteristics of microvascular exchange units adapted from the solution of close-packed patterns of circles of two diameters. We find that the patterns exchange coefficients vary and that biological systems generally employ the more efficient patterns. However, two patterns have not been found in biological systems and yet we found they are also efficient for both heat and mass transfer.

Our interest in compact packing patterns was first piqued by observations of natural systems

as almost all biological systems converge on one of these solutions (Figure 3.1a). A complete set of solutions to binary circular packing was recently reported by Kennedy.[33–37] In determining if packing patterns effected transfer, we studied the relative transfer rates among four of the patterns using finite element modeling. As no formal names exist, we refer to the different patterns as "Hexagonal", "Dodecagonal", "Squarer", and "Double Squarer" in this report (Figure 3.1c). While the "Hexagonal" and "Squarer" patterns have known natural analogs to the avian lung and piscine gas bladder, respectively, the "Dodecagonal" and "Double Squarer" have no biological analogs that we can identify. Additionally patterns, the "Dodecagonal" and "Double Squarer" were chosen for their similarity to biological patterns, but have never been found in biological systems. Each pattern has an optimal ratio between diameters of the two circle sizes, which allows for the highest occupied density in a regular lattice arrangement. For synthesis and analysis, we modified these ratios to maintain constant minimum inter-channel distances and to account for available fabrication sizes.

Intrigued by our observations and preliminary models, we fabricated these four patterns to confirm the model results, including the abiological patters which were of particular interest. To synthesize such compact patterns, we used the Vaporization of a Sacrificial Component (VaSC) technique. VaSC employs a sacrificial element rather than a lithographic or direct-write approach.[38, 39] During the course of experiments, we measured the mass transfer characteristics of each packing structure using a model reaction between carbon dioxide and monoethanolamine (MEA, 30% w/w). The highest mass transfer coefficient, for our samples, occurs in the "Double Squarer", a previously unknown pattern, and the lowest in the "Hexagonal" close packed patterns. We measured the heat transfer characteristics of each packing structure by using the countercurrent flow of hot and room temperature water. The highest heat transfer coefficient is again found in a "Double Squarer" an abiological pattern. The general trends found in the mass transfer coefficients were also found in the heat transfer coefficients. It should be noted that the geometries chosen were constrained, by fabrication techniques, to only certain patterns. The primary constraint was to maintain a

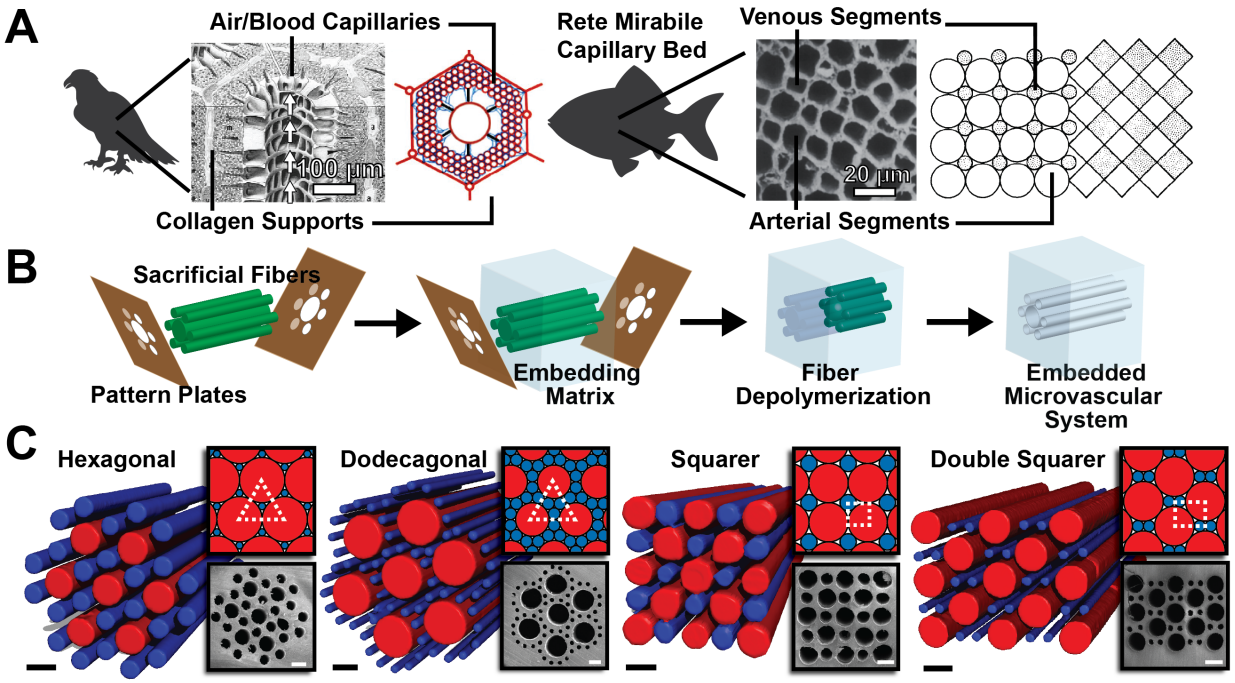

Figure 3.1: Biological inspiration, design and creation of close packed patterned exchangers. (A) Natural exchange systems. The avian lung contains a modified hexagonal packing structure for the transfer of CO_2 and O2 [29, 32], reproduced with permission from Environmental Health Perspectives and Journal of Anatomy. The piscine gas bladder uses a squarer packing structure for the release of O_2 to control its buoyancy [30, 31], reproduced with permission from Microvascular Research and The Biological Bulletin. (B) VaSC fabrication process of compact, packing elements. Sacrificial fibers are placed in a parallel arrangement using patterning plates. A polymer matrix then fills the space between the fibers. Last, the fibers are depolymerized, resulting in a hollow microvascular system. (C) Microvascular close packed patterns. SEM and μCT images confirm the fabrication of the patterned exchange units. Inset are the ideal geometries for the most densely packed structures. Unit cell shapes are outlined in white. Scale bars are 300 μm.

minimum inter-channel distance of 50 μm. Other parameters such as mean distance, channel ratios, and closeness to ideal sizes were also considered, but not experimentally examined.

3.2 Experimental

Materials: Monoethanolamine (99%, MEA), tin (II) oxalate (98%), and fluorescein were purchased from Sigma-Aldrich. 5-(and-6)-Carboxynaphthofluorescein was purchased from Invitrogen. Tris-HCl was purchased from J. T. Baker. Sylgard®184 silicone elastomer kit (PDMS) was purchased from Dow Corning. Disperbyk-130 was purchased from BYK Additives & Instruments. Trifluoroethanol (TFE) was purchased from Halogen Inc. Poly(lactic) acid (PLA) fibers were provided by Teijin Monofilament.

VaSC Fiber Preparation: Tin (II) oxalate was entrapped within PLA fibers to lower its depolymerization temperature from 280 °C to 200 °C. A 800 mL treatment solution was created (400 mL deionized water, 400 mL trifluoroethanol, 50 g tin oxalate, 20 g DISPERBYK-130, 0.5 g malachite green) to infuse the tin oxalate within the fibers and to dye the fibers for visual clarity. Fibers were wound around a custom spindle and placed within the solution. The solution with the fibers was spun at 300 RPM for 48 hours at room temperature. The fibers were then removed from the solution and dried in air at room temperature for 24 hours.

Exchange Unit Fabrication: PDMS was created using mixtures of the Sylgard 184 silicone elastomer base and curing agent with a 10:1 ratio between base and curing agent. VaSC fibers were strung through two laser-cut brass plates containing the desired close-packed patterns. The plates were placed onto a 1 in. long mold box with the fibers tensioned on either side to create a set of parallel fibers in the patterned arrangement within the mold box. The mold box was then filled with PDMS and cured at 85 °C for 1 hour. A second

stage of molding with PDMS was performed to separate the channels from the pattern and allow for easier loading of channels. The vascular preforms were heated to 210 °C under vacuum to vaporize and removed the fibers embedded within the PDMS resin resulting in a close packed arrangement of hollow channels.

Mass and Heat Transfer Model: The models were created using the COMSOL Multiphysics Modeling and Simulation software. The models assumed conservation of momentum, mass and energy to describe the movement of fluids and mass. The models use several parameters including diffusion coefficients, reaction rates, fluid properties, heat capacities, thermal conductivities, and densities (Figure 3.4).[40–45]

Exchange Unit Imaging: Scanning Electron Microscope (SEM) images were taken on a FEI Quanta FIB system (Oxford Instruments) and performed at the Laboratory for Electron and X-ray Instrumentation (LEXI) at UC Irvine. The images were taken at a beam current of 8.31 pA and a voltage of 2.00 kV. X-ray computed tomography (μCT) images were taken using a Xradia VersaXRMTM 410 nano-CT system and also performed at LEXI. Images were taken at a 40 kV and 7 W beam settings at 4X magnification. Image reconstruction to form the three-dimensional images was performed using ImageJ image processing software.

3.3 Results and Discussion

Each microvascular exchange unit was modeled using COMSOL Multiphysics. For mass transfer, the model predicted that the "Double Squarer" pattern had the highest mass transfer coefficient while the "Hexagonal" pattern had the lowest. For heat transfer, similar predictions were made due to the underlying physical laws governing mass and heat transfer. The prediction that the "Double Squarer" pattern has the highest mass and heat transfer rate intrigued us, because it has no known natural analog and a lower degree of rotational

symmetry. A full analysis of our model parameters are provided later in the text.

To test our predictions, we fabricated close-packed microvascular exchange units by employing the VaSC fabrication process (Figure 3.1b). VaSC uses a positive polymer template to create long, cylindrical microchannels placed in a patterned arrangement. Poly(lactic) acid (PLA) fibers were impregnated with a Tin(II) catalyst to lower its depolymerization temperature using a solution that swells the fibers allowing the catalyst to enter the swollen region. The fibers were then placed in a compact, packed pattern using pairs of laser-cut micromachined plates. The fibers were strung through the plates and then placed under tension to create a parallel arrangement of fibers matching the patterning plates. To create a membrane, the space between fibers was filled with polydimethylsiloxane (PDMS) pre-polymer. PDMS was cured at 85 °C for 30 min to form the embedding matrix of the patterns. Last, the fibers were depolymerized under vacuum at 210 °C for 48 hours. The result was a single exchange unit, consisting of a set of microchannels matching the desired pattern.

Based on the packing patterns for circles of two sizes, a precise ratio between two sizes exists for each pattern to form the densest packing of the circles. However, we adjusted the dimensions to accommodate the requirement of 50 μm minimum separations between all fibers and discrete fiber diameters. These two adjustments resulted in average packing densities of ˜57%. For each pattern, multiple unit cells were fabricated. Each exchange unit structure was confirmed using scanning electron microscopy (SEM) and X-ray computed tomography (μCT) imaging techniques. For ease of testing, structures were fabricated with a single unit cell, surrounded by nearest neighbor channels.

First, we examined the mass transfer characteristics of the close-packed systems. The mass transfer model solved the Navier-Stokes equation for fluid flow and Ficks laws of diffusion to predict the mass transport in the close-packed vascular system.[40, 41] We then matched model to experiment (Figure 3.2a). In our experiment, carbon dioxide flowed through the larger set of channels at the same flow rate as the model (1 mL/min per channel). The gas

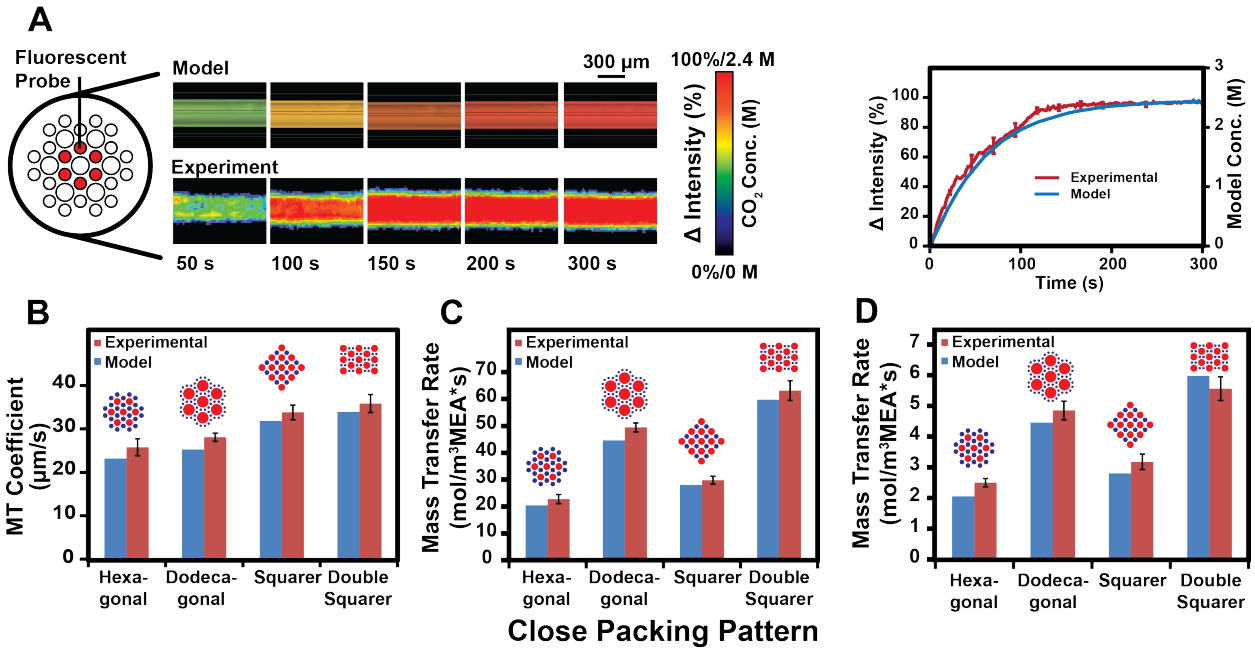

Figure 3.2: Close packing mass transfer. (A) Model and experimental comparison. The reaction between CO_2 and monoethanolamine (MEA) was used to obtain the mass transfer characteristics. A CO_2 sensitive fluorescent solution was loaded into the microchannels to visualize the capture of CO_2 by MEA. The normalized intensity change in intensity and predicted model concentration are plotted against time. (B) Mass transfer coefficient. Differences between the patterns were observed, with the "Double Squarer" pattern obtaining the highest mass transfer coefficient. (C) MEA volume normalized mass transfer rate. Differences between the patterns become more pronounced, although the "Double Squarer" pattern still obtained the highest mass transfer rate. (D) MEA volume normalized mass transfer rate using 10% CO_2. Mass transfer rates were similar to the results from the use of 100% CO_2, but decreased by a factor of 10. Reported values are mean ± SD (n=3).

diffuses across the PDMS membrane and reacts with MEA (30% wt. in H2O) containing a pH sensitive fluorescent dye (5-(and-6)-Carboxynaphthofluorescein, 0.17 mg/mL) in the smaller channels. To test the micro-vascular exchange, each unit is mounted on a fluorescent microscope. As MEA reacts with carbon dioxide, the carbamic acid formation lowers the pH of the solution. The fluorescence intensity of the probing dye decreases as the pH decreases (from pH ˜12 to ˜8), providing a colorimetric readout of mass transfer. The change in intensity is normalized, reaching 100% change at its lowest intensity value (Figure 3.2a). We calculated the mass transfer rate by measuring the time to reach an intensity change of 80% (2.2 M CO_2). We initially examined the mass transfer characteristics of the close-packed patterns by comparing the mass transfer coefficients (Figure 2b). The "Double Squarer" pattern had the highest mass transfer coefficient (36 $\pm$ 2.1 μm/s) of all the synthesized close-packed patterns and was ˜40% greater than that of the lowest rate, found in the "Hexagonal" pattern (26 $\pm$ 2.0 μm/s). Similar trends were found from the computational model, but experimentally obtained mass transfer rates were 3-10% higher than predicted.

The mass transfer rates per total volume of the liquid phase provided further insight into the effects of the packing geometries (Figure 3.2c). The patterns containing 100 μm diameter channels consistently obtained the highest mass transfer rates with respect to the volume of MEA used (up to 63 mol/m3s). To simulate an application of a mass transfer device, 10% CO_2 (balance N_2), representing the CO_2 in the flue stream produced by a power plant, was flowed through each pattern (Figure 2d). Similar trends were found and the measured mass transfer rates were ten times lower than the mass transfer rates obtained using pure CO_2. Again, the model predicted similar, but lower mass transfer rates.

Next, the heat transfer characteristics of the packing patterns were examined. The heat transfer model solved the Navier-Stokes equation again for fluid flow, while the heat equation and Fouriers Law were used for heat transfer.[46, 47] We experimentally examined the heat transfer characteristics through the counter-current flow of warm (0.2 mL/min per channel,

45 °C) and colder water (0.1 mL/min per channel, 25 °C). The three-dimensional geometries of the close-packed patterns created difficulty in using thermocouple elements to measure the temperatures. Instead, a thermally sensitive, fluorescent solution was used.[48] The solution consists of fluorescein coupled to a Tris-HCl solution (10 μM fluorescein in 10 mM Tris-HCl). The pH of Tris-HCl depends on temperature and the intensity of fluorescein depends on pH (Figure S3b). This coupled solution acts as an intensity based temperature probe (Figure 3.3a). Using this probe, the temperature gradient within a close-packed structure was measured, allowing for the measurement of heat transfer (Figure 3.3b).

The heat transfer characteristics were compared using the heat transfer coefficients of each pattern (Figure 3.3c). The heat transfer model was less accurate than the mass transfer model and predicted the heat transfer characteristics of the patterns to within 20 percent. The elastomeric properties of the membrane allow the exchanger to potentially physically deform while fluid flows through the exchanger. This may change the geometry and result in different heat transfer characteristics. We found that the "Double Squarer" pattern again obtained the highest heat transfer coefficient (3000 W/m^2 K). The trends between the patterns were identical to the mass transfer coefficients. These values are lower than conventional micro heat exchangers (˜5000-20000 W/m^2 K).[26] However, PDMS is a poor conductor of heat. Heat transfer coefficients would increase with increased thermal conductivities of the material used to cast the micro vascular exchange unit. We expected the agreement found between trends for the mass transfer coefficients and heat transfer coefficients due to the similar governing physical laws behind heat and mass transfer. Nusselt numbers were also calculated for the patterns and the "Hexagonal", "Squarer", and "Double Squarer" patterns obtained similar values while the "Dodecagonal" pattern obtained the lowest (Figure 3.14).

Although we had determined that the "Double Squarer" pattern obtained the highest transfer coefficients, we sought to understand the reasoning behind this. In looking towards explaining why certain patterns obtained higher mass or heat transfer coefficients than others, the

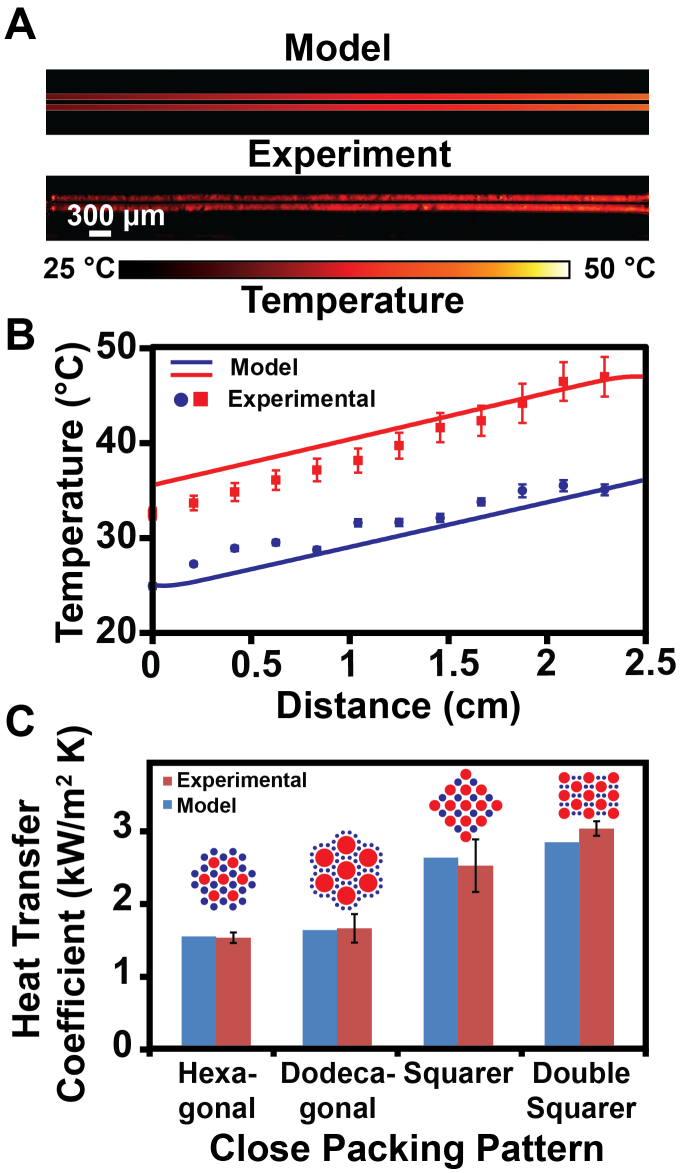

Figure 3.3: Comparison of heat transfer in close packing patterns. (A) Model and experimental comparison. Warm and cool water flow counter-currently through the exchange, resulting in a temperature gradient. A temperature-dependent, fluorescent solution was flowed through the microvascular exchange unit to measure the temperature profile of the packing patterns. The solid lines indicate the predicted model temperatures. (B) Sample temperature profile. The changes in temperature across the hot and cool channels are used to calculate the heat transfer characteristics within the exchangers. (C) Heat transfer coefficients. The "Double Squarer" pattern obtained the highest heat transfer coefficient while the other patterns obtained similar coefficients as each other. Reported values are mean ± SD (n=3).

distances between two sets of channels were initially examined. The closest distance between one set of channels to the other, over the entire arc length of a channel was calculated. We found that as the root mean square of the nearest channel distances decreased, the transfer coefficients increased (Figure 3.15). However, when we adjusted the models to maintain constant mean distances, the relative transfer coefficients between patterns remained the same. Upon further investigation using the model, we found that channel ratios and use of ideal channel sizes impacted the transfer coefficients.

3.4 Experimental Details

3.4.1 Close Packing Designs

For these circular patterns, there are only nine possible radii ratios that lead to close packed configurations in a binary system (Figure 3.4).[33] Each close packed pattern contains an ideal ratio between circle diameters to remain close packed. Of the nine patterns, two have been identified in nature: the "Hexagonal" and "Squarer" patterns. We chose two other patterns to examine due to their similarities to the ones found in nature: the "Dodecagonal" and "Double Squarer". The "Dodecagonal" and "Hexagonal" patterns both have equilateral triangular unit cells while the "Double Squarer" and "Squarer" patterns are the only patterns with quadrilateral unit cells. The other unit patterns were not examined in this report due to unit cell shape (a,b,e), asymmetric unit cell (c), or lack of available microfibers for fabrication (i).

In designing the exchange unit patterns, primary requirement was to maintain a 50 μm minimum separation. This requirement was enforced as the fabrication plates are unable to have smaller separations. The available microchannel sizes were 100, 200, 300, and 500 μm diameters, which drove the modification of the packing pattern geometries (Table 3.1,

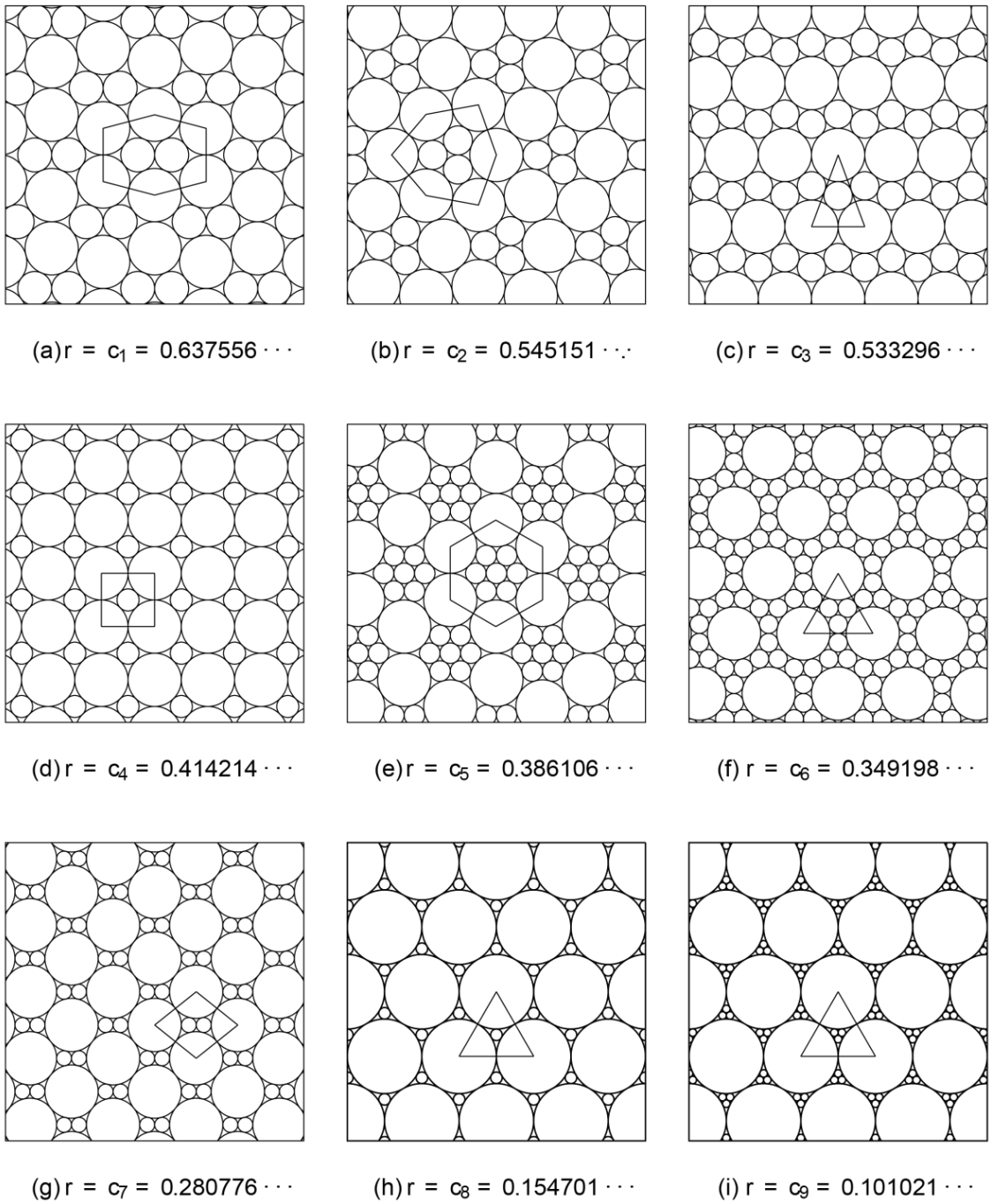

Figure 3.4: Close packing of discs of two sizes. The nine possible close packing disc radii ratios are displayed. The "r" values indicate the ratio between the two radii in each pattern.

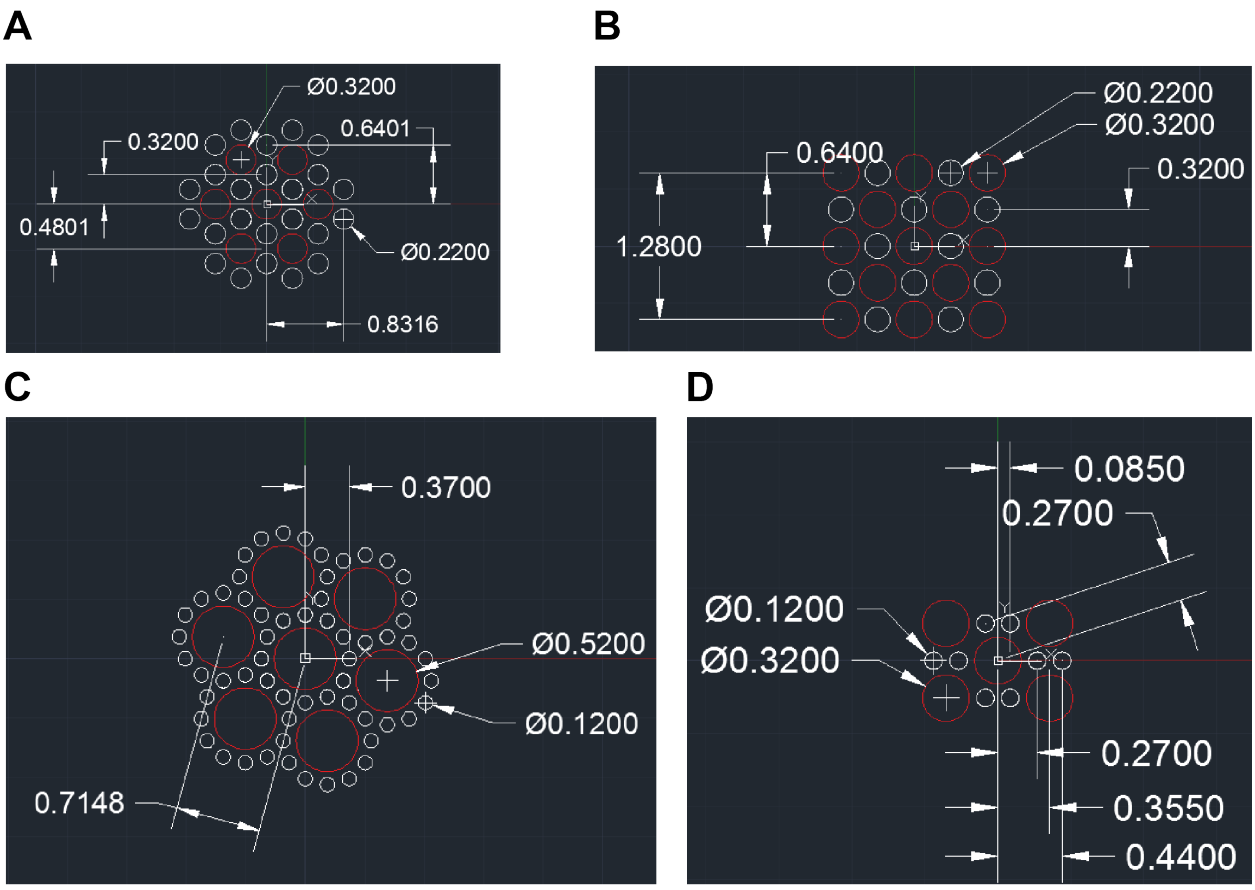

Figure 3.5: Plate pattern designs. Plate designs were constructed in AutoCAD. Additional space was added to the hole sizes to allow for easier threading of sacrificial fibers. (A) Hexagonal. (B) Squarer. (C) Dodecagonal. (D) Double Squarer.

Figure 3.5). The hexagonal pattern contains the greatest deviation from the ideal parameters due to its use in our previous microvascular mass transport studies. To obtain the modified parameters, the ideal parameters were scaled to be ˜20% larger than available fiber diameters. Then 50 μm was subtracted from one set of channel diameters. Finally, the results were rounded to the nearest available channel diameters.

3.4.2 Exchange Unit Fabrication

Fibers were treated according to the Vaporization of Sacrificial Components (VaSC) technique with some modifications.1 Briefly, tin oxalate is incorporated into PLA fibers through

Packing Pattern	Ideal Channel Diameter (μm)		Adjusted Channel Diameter (μm)		Measured Channel Diameter (μm)		Interchannel Distance (μm)	Packing Density (%)
	Large	Small	Large	Small	Large	Small		
Modified Hexagonal	350	54	300	200	318±5	207±9	52±6	57
Dodecagonal	500	175	500	100	503±8	99±3	51±8	61
Squarer	350	145	300	200	306±5	205±4	52±4	57
Double Squarer	300	84	300	100	312±5	100±6	53±2	55

Table 3.1: Packing pattern geometries. Ideal channel diameters represent the closest possible packing arrangement using the pattern. For practical fabrication, channel diameters were adjusted to compensate for membrane thicknesses and available channel sizes.

Figure 3.6: Custom spindle for fibers to wrap around. The spindel is built to ensure proper mixing of the catalyzing solution while reducing surface contact with the fibers.

entrapment within the swollen surface of the fibers. The incorporation of tin oxalate lowers the depolymerization temperature of PLA down to 200 °C. When placed under heat and vacuum, the solid PLA polymer depolymerizes into gaseous monomers which can be evacuated when placed within a template. 800 mL of treatment solution was used (400 mL deionized water, 400 mL TFE, 50 g tin oxalate, 20 g disperbyk-130, 0.5 g malachite green). Fibers were wound around a custom spindle and placed in the solution. The spindle comprised of six steel rods affixed around a central core with a mixer at the bottom (Figure 3.6). The solution with fibers was agitated with a digital mixer (IKA RW20) at 250 RPM for 48 h at 25° C.

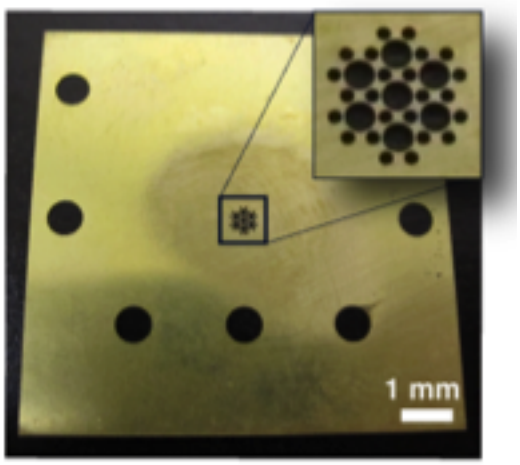

Figure 3.7: Laser-etched micromachined brass plates. Fibers are strung through the holes in the end caps, providing the desired pattern.

Polydimethylsiloxane (PDMS) was created using mixtures of the Slygard 184 silicone elastomer base and curing agent with a 10:1 ratio between base and curing agent inside paper cups. The mixtures were then degassed using a rough vacuum pump and glass bell jar for 15 minutes.

Treated fibers were patterned using laser micromachined brass plates manufactured by Hodge Harland at the University of Illinois at Urbana-Champaign (Figure 3.7). Fibers were strung through matching holes on a pair of plates which were then screwed onto a delrin mold box with dimensions of $25 \times 25 \times 25$ mm. The fibers were tensioned until taut on a custom board with pairs of guitar tuning pegs on either side (Figure 3.8,3.9). The degassed PDMS mixtures was poured into the mold and heated at 65°C for 1 h using a Breville Smart Oven to complete the polymerization reaction.

The units were then removed from the first mold and placed into a second mold box with dimensions of $25 \times 25 \times 50$ mm. The fibers were separated and threaded through PDMS end-caps which were screwed onto the mold box. Syringe needles (B-D PrecisionGlide 18G1 Needle) were inserted through the PDMS end caps and fibers were threaded through the needles. The needles were removed leaving the fibers in the end caps. The end caps were

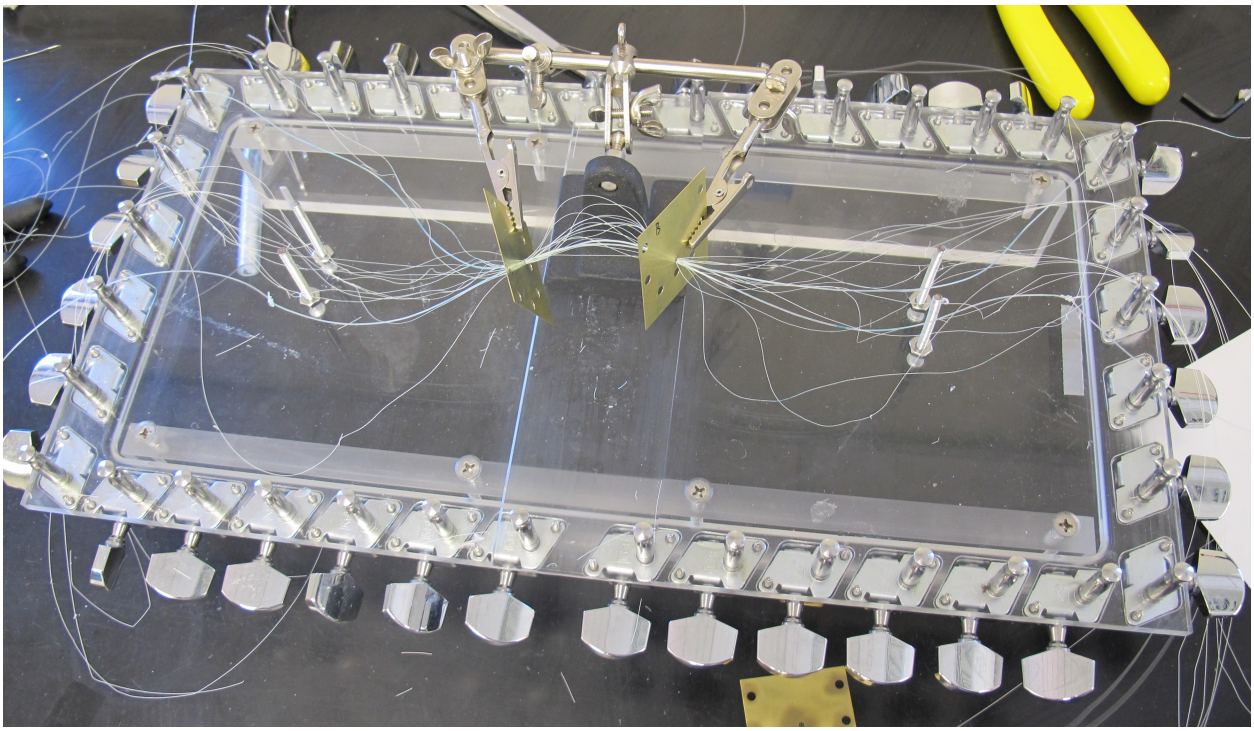

Figure 3.8: Example custom molding board. Guitar tuners on either side provide tensioning for fibers.

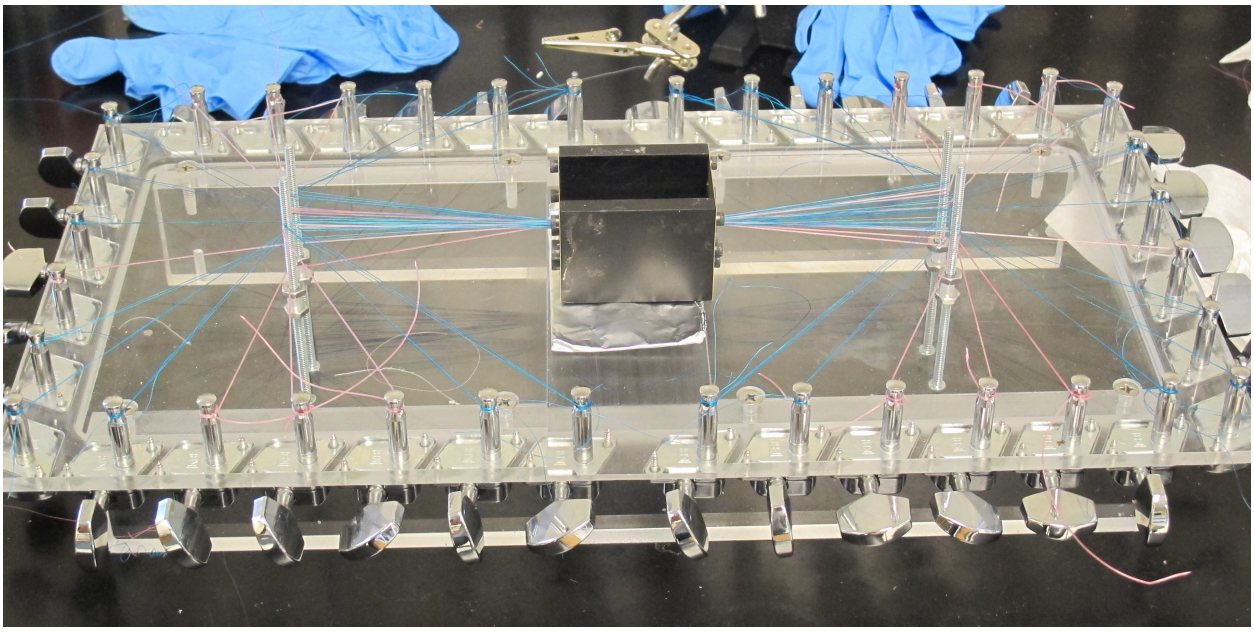

Figure 3.9: Assembled molding setup. Fibers are tensioned through the brass end caps using the tuning board. Metal rods in the board act as pullys to help tuning pegs along the side of the board to tension the fibers.

screwed onto the larger mold box and fibers were pulled taut by hand. A second mold of PDMS was then cast again at 65°C for 1 h (Figure 3.10). Longer samples were created using a 25 × 25 × 50 mm box as the first mold and 25 × 25 × 75 mm box as the second mold.

The vascular preforms were removed from the second mold. The remaining fibers extending out of the PDMS were then cut from the edges of the molded shape. The vascular preforms were placed into a sealed vacuum oven (JEIO Tech Vacuum Oven Model OV-11/12) and subjected to a vacuum of 10 torr and heated to 210 °C for 48 h.

3.4.3 Heat Transfer Experimental Details

A 250 mL solution of 10 μM Fluorescein in 10 mM Tris-HCl adjusted to a pH of 7.1 at 22 °C was prepared as the temperature probe. All liquid solutions and exchangers were degassed under vacuum prior to conducting the experiments. The exchangers were separated into warm and colder channels, with the small channels corresponding to the colder set and the larger channels corresponding to the warmer set. The temperature probing solution flowed through the warm and colder channels in separate runs to measure the temperature profiles of the exchangers. Water flowed through the opposite channel sets. Peristaltic pumps (Buchler Polystaltic Pump) were used to flow the fluids through the channels. A water bath was used to regulate the temperature of the fluid reservoirs. A syringe heating jacket (Syringe Heater, Pump Systems Inc.) surrounded a stainless steel pipe (1/4 Pipe Size ×3" Length) to heat the fluid entering the warm channels (Figure 3.11). Time lapsed images were taken with a Zeiss Axio Observer.A1 Microscope using a 2.5 X objective at intervals of 1 minute for 2 hours were taken to ensure that steady state temperature gradients were reached. The fluorescence intensity was set to the minimum possible intensity. The first 30 minutes of each run began with no heating to obtain a baseline intensity value for the room temperature. After the first 30 minutes, the heating jacket was turned on to a set point of 95 °C. While

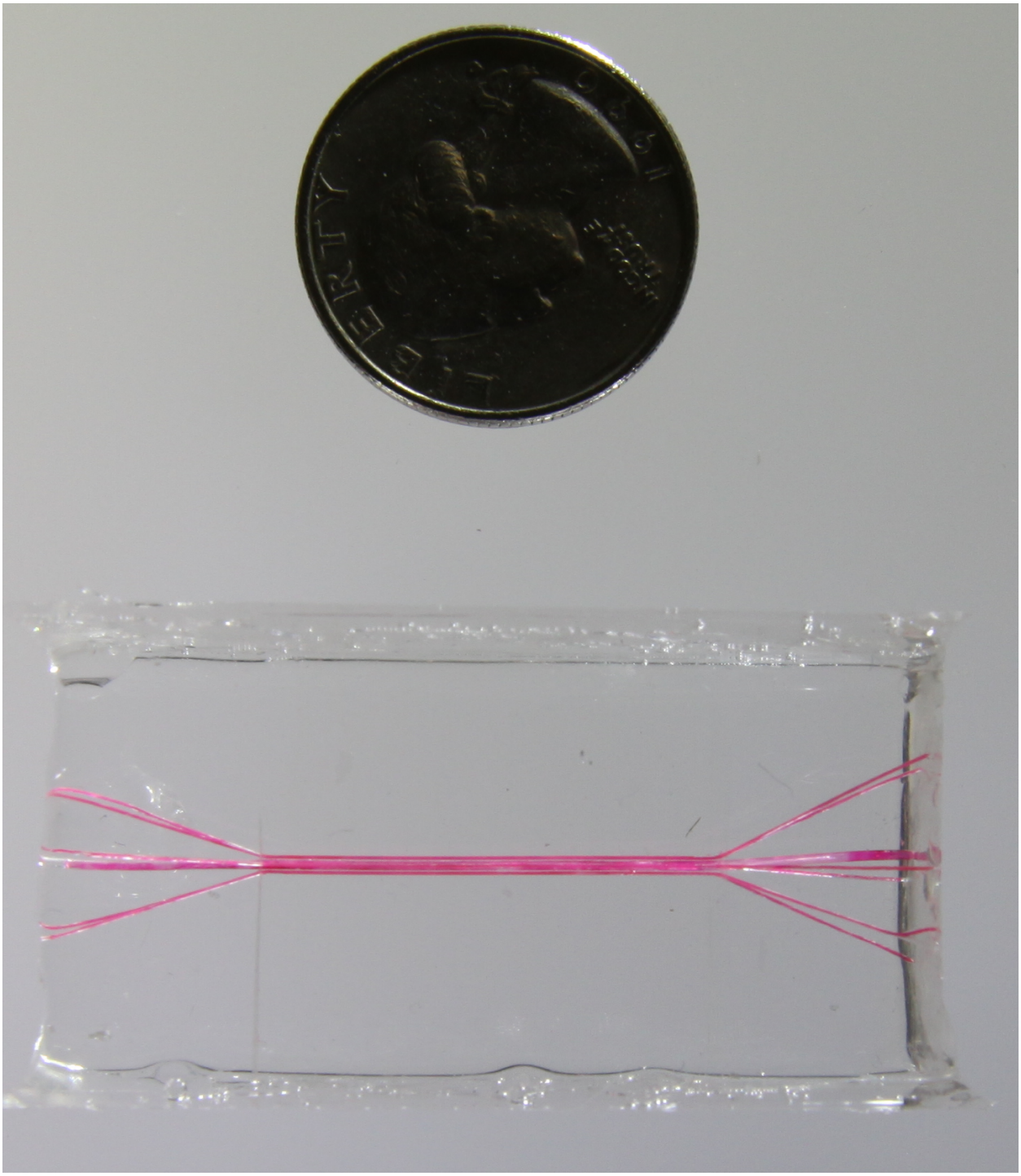

Figure 3.10: Assembled molding setup. Fibers are tensioned through the brass end caps using the tuning board. Metal rods in the board act as pullys to help tuning pegs along the side of the board to tension the fibers.

heat was lost between the heater and exchanger, the temperature profile provided by the temperature probe solution allowed for the precise measurement of the inlet temperatures.

3.4.4 Mass Transfer Experiment

1 mg of 5-(and-6)-carboxynaphthofluorescein diacetate dye was added to 6 mL of 30% monoethanolamine (MEA) to create the dyed solution. Each close packed structure was separated into fluid and gas channels, with the smaller channels corresponding to the fluid and the larger channels corresponding to the gas channels. The dyed MEA was loaded into the central fluid channels which were completely surrounded by gas channels. CO_2 was flowed through the gas channels at a flow rate of 1 mL/min per gas channel using a mass flow controller (SmartTrak 50 Mass Flow Controller). Time lapsed images were taken with a Zeiss Axio Observer.A1 Microscope using a 2.5 X objective at intervals of 6 seconds for 5 minutes (Figure 3.12). The fluorescence intensity was set to the minimum possible intensity. The microscope shutter was manually operated to prevent photo-bleaching of the dye.

3.5 Theoretical Details

3.5.1 COMSOL Model: Mass and Heat Transport

The COMSOL Multiphysics program was used to create models of the close packed patterns. The physical geometries of the units were generated using 8 mm long unit cells of the different patterns. Symmetric boundary conditions were placed along the edges of the unit cells to model the entire close packed geometries. Meshes composed of tetrahedrons were formed to approximate the physical geometries of the systems and allowed for numerical calculations within the model. Two sets of physics simulations modules were used (Laminar Flow and

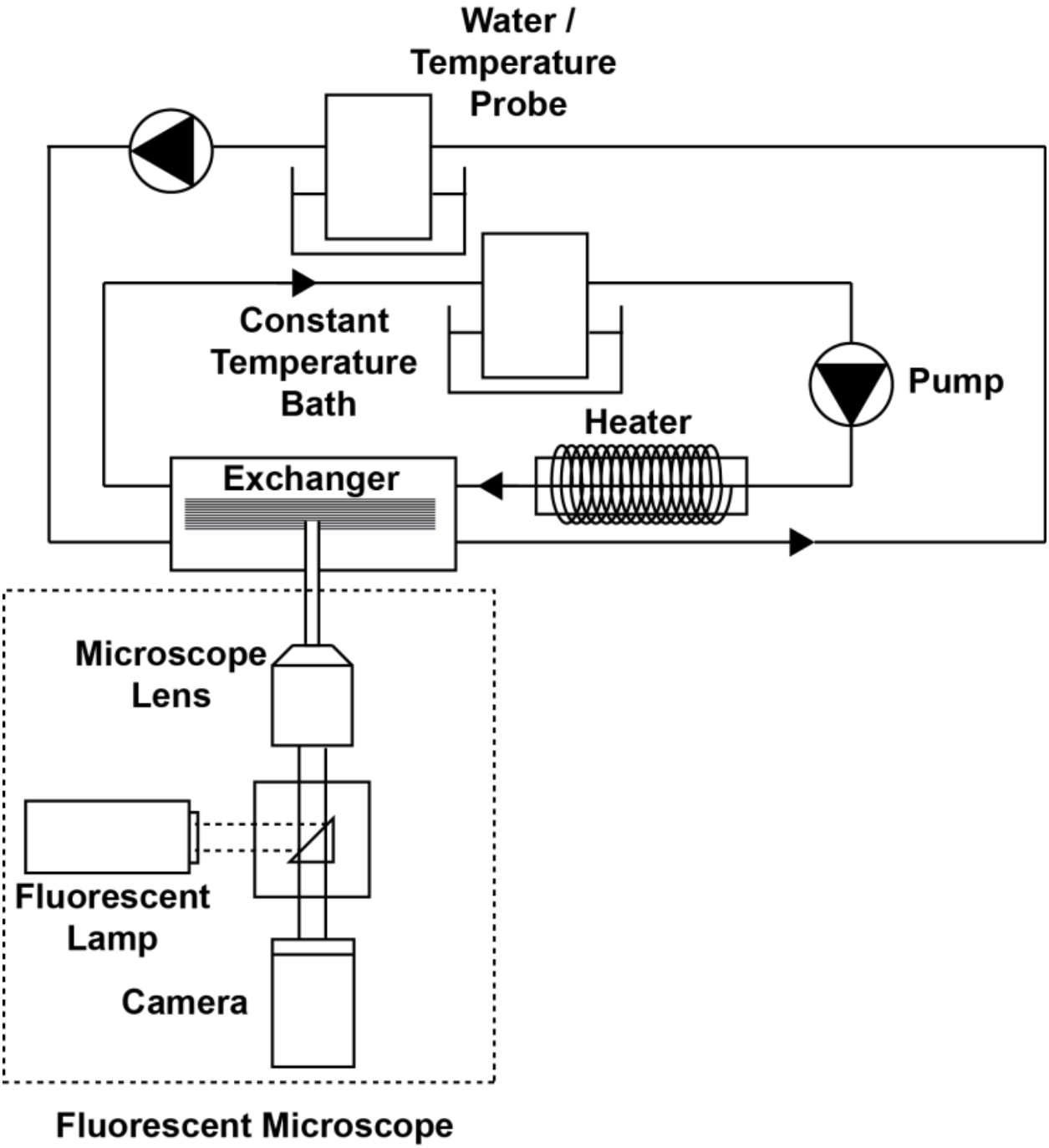

Figure 3.11: Heat transfer experimental schematic. The flows of the hot and cool fluids are controlled by peristaltic pumps. The fluorescent probe flows through either sets of channels to measure the temperature profile in both.

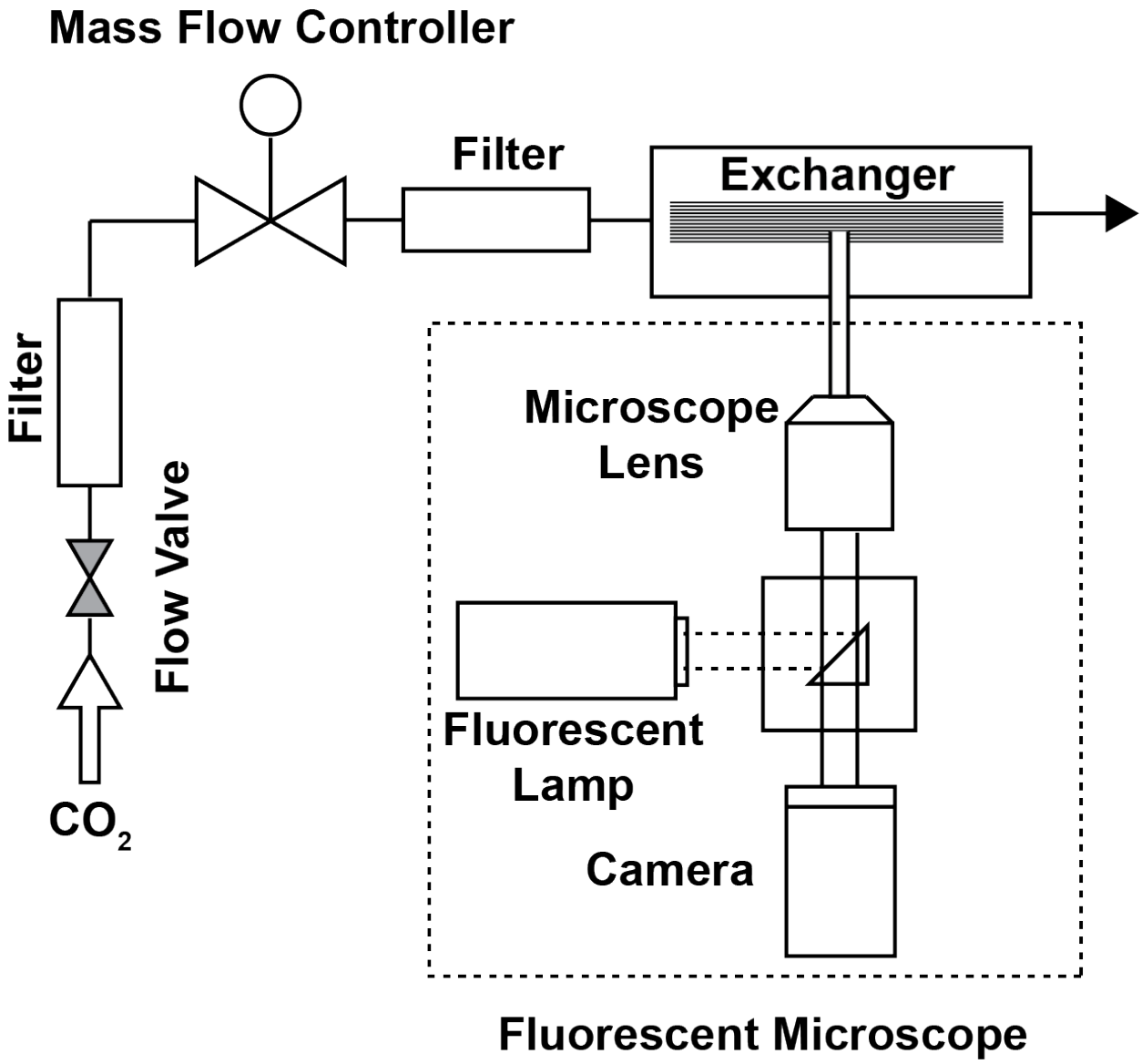

Figure 3.12: Mass transfer experimental schematic. The flow of CO_2 is controlled by a mass flow controller to maintain a constant flow rate. A pH sensitive fluorescent dye monitors the transfer of CO_2 from one set of channels to another under the observation of a fluorescent microscope.

Physics Module	**Location**	**Parameter**	**Value**
Laminar Flow	CO_2 Channels	Laminar inflow flow rate	1 cm^3/min per channel
		Entrance length	300 or 500 μm
	MEA Channels	Inflow Pressure	0 Pa
Transport of Diluted Species (All)	All	Velocity field	(spf/fp1)
Transport of Diluted Species (CO_2)	CO_2 Channels	Diffusion coefficient[6]	16 mm^2/s
		Inflow	45 mol/m3 (4.5 for 10% CO_2)
	MEA Channels	Diffusion coefficient[8]	1.51e-9 m^2/s
		Inflow	0 mol/m3
		Reaction equation[40, 42]	-6550*[CO_2]
	PDMS	Diffusion coefficient[41]	7.08e-10 m^2/s
Transport of Diluted Species (MEA)	Outer Channels	Diffusion coefficient[45]	9.32e-10 m^2/s
		Initial concentration	4900 mol/m3
		Reaction equation[40, 42]	-6.550*2* [CO_2][MEA]
Transport of Diluted Species (MEA-COOH-)	Outer Channels	Diffusion coefficient[45]	9.32e-10 m^2/s
		Initial concentration	0 mol/m3
		Reaction equation[40, 42]	6.550*[CO_2][MEA]

Table 3.2: Coefficients and parameters used in the mass transfer model.

Transport of Diluted Species) and the parameter definitions are as follows:

The program initially solved for the steady state velocities and pressures in the fluid and gas channels, assuming laminar flow. The solution parameters from the fluid and gas flows were then used to determine the time-dependent solution to the transportation of species within the model gas exchange unit. Similar methods were used to solve the heat transfer model using the Non-Isothermal Flow module (Table 3.3).

Physics Module	**Location**	**Parameter**	**Value**
Non-Isothermal Flow	All	Velocity field	(spf/fp1)
	Fluid Channels	Density	838.466+1.401*T-.003011*T2+3.718E-7*T3 kg/m3
		Heat Capacity at Constant Pressure	12010-80.41*T+.3099*T2-5.382E-4*T3+3.623E-7*T4 J/(kg*K)
		Thermal Conductivity	-0.8691+0.008949*T-1.564E-5*T2+7.975E-9*T3 W/(m*K)
		Dynamic Viscosity	1.3799566804-0.021224019151*T+1.3604562827E-4*T2-4.645090319E-7*T3+8.9042735735E-10*T4-9.0790692686E-13*T5+3.8457331488E-16*T6 Pa*s
	Hot Channels	Laminar inflow flow rate	0.2 cm^3/min per channel
		Entrance length	300 or 500 μm
		Temperature	45 °C
	Colder Channels	Laminar inflow flow rate	0.1 cm^3/min per channel (Countercurrent Direction)
		Entrance length	200 or 100 μm
		Temperature	25 °C
	PDMS	Density[43]	970 kg/m^3
		Heat Capacity at Constant Pressure[43]	1460 J/(kg*K)
		Thermal Conductivity[43]	0.15 W/(m*K)

Table 3.3: Coefficients and parameters used in the heat transfer model. Parameters not cited were built into the COMSOL materials database.

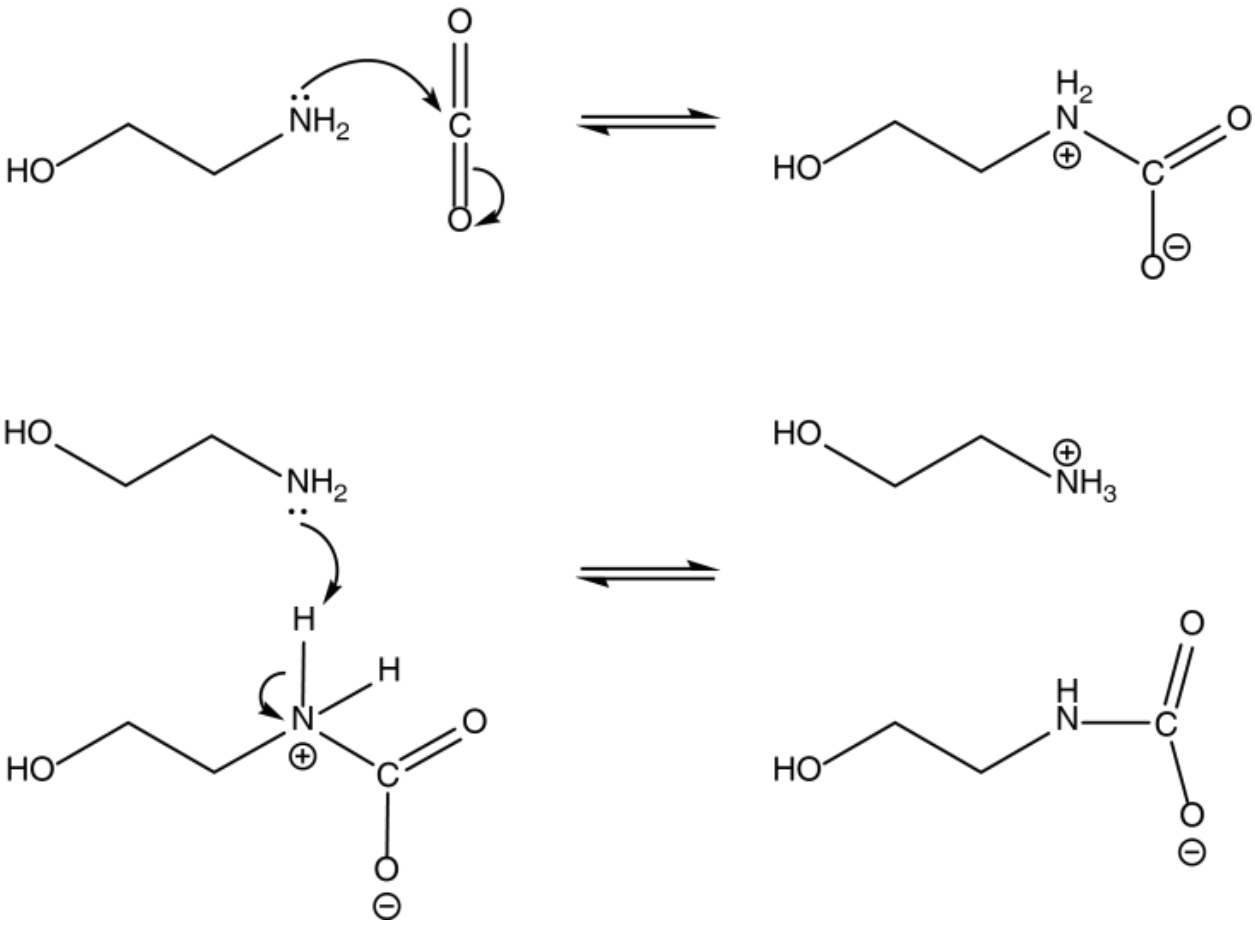

Figure 3.13: CO_2-MEA reaction mechanism. Heating the solution drives the reverse reaction, releasing CO_2.

3.5.2 CO_2 MEA Reaction Mechanism

The reaction between CO_2 and MEA is a two-step reaction mechanism which occurs through a zwitterion intermediate (Figure 3.13).[42–44] MEA and CO_2 react to form a zwitterion intermediate as the rate-determining step. Following this zwitterion formation, an acid-base reaction occurs between the zwitterion and another MEA to form carbamate.

3.5.3 Heat Transfer Calculations

The heat transfer coefficients were calculated based on the temperature gradient across the length of the channels using the log mean temperature differences and channel geometries.

ΔT_m = Log mean temperature difference (K)

$T_{H_{in}}$ = Hot channel inlet temperature (K)

$T_{H_{out}}$ = Hot channel outlet temperature (K)

TC_{in} = Colder channel inlet temperature (K)

$T_{C_{out}}$ = Colder channel outlet temperature (K)

Q = Heat transferred (W)

ρ = Fluid density (g/m^3)

Cp = Fluid heat capacity at constant pressure (J/g*K)

V = Volumetric fluid flow rate (m^3/s)

q = Heat flux (W/m^2)

A = Channel surface area (m^2)

h = Heat transfer coefficient ($W/m^2 * K$)

Nu = Nusselt number

Dh = Channel diameter (m)

k = thermal conductivity (W/m*K)

$$\Delta T_m = \frac{(T_{H_{in}} - T_{C_{out}}) - (T_{H_{out}} - T_{C_{in}})}{Ln\left[\frac{(T_{H_{in}} - T_{C_{out}})}{(T_{H_{out}} - T_{C_{in}})}\right]}$$

$$Q = rhoC_pV(T_{C_{out}} - T_{C_{in}})$$

$$q'' = \frac{Q}{A}$$

$$Nu = \frac{hD_h}{k}$$

3.5.4 Nusselt Numbers

The Nusselt numbers for the various patterns were also calculated (Figure 3c). A higher Nusselt number indicates higher convective heat transfer across a boundary while a lower number indicates higher conductive heat transfer (Figure 3.14). The "Hexagonal", "Squarer", and "Double Squarer" patterns obtained comparable Nusselt numbers (˜0.5) while the "Dodecagonal" pattern obtained the lowest (0.3). The Nusselt numbers obtained by the close-packed exchangers were lower in comparison to other exchange devices since the model exchange material, PDMS, is a poor conductor of heat.

3.5.5 Transfer Coefficient Correlations

The distances between the smaller and larger sets of channels were found for each close packed pattern. The distance was calculated from the edge of the smaller channel to the nearest edge of one of the larger channels (Figure 3.15). This distance was calculated over the entire arclength of the small channel and used to find the root mean square distance (RMS). Correlations between the RMS distance and the transfer coefficients were found.

Further investigation into the correlations was performed using the COMSOL models (Figure S14). When the RMS distances were normalized to 61.9 μm (Double Squarer distance),

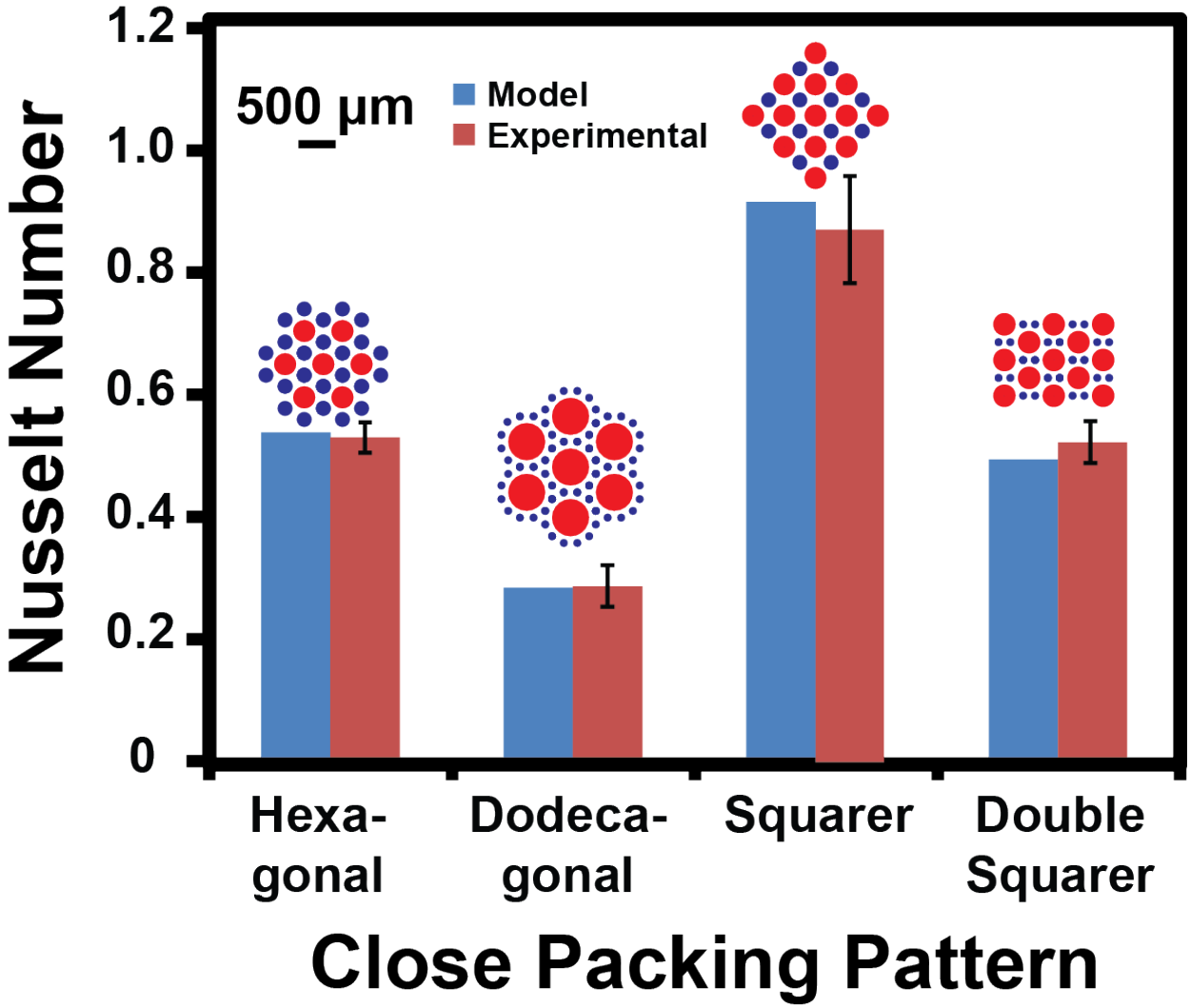

Figure 3.14: Nusselt Numbers. The "Hexagonal", "Squarer", and "Double Squarer" patterns obtain similar Nusselt numbers while the "Dodecagonal" pattern obtains the lowest. The largest discrepancy between model and experimental values is found in the "Squarer" pattern.

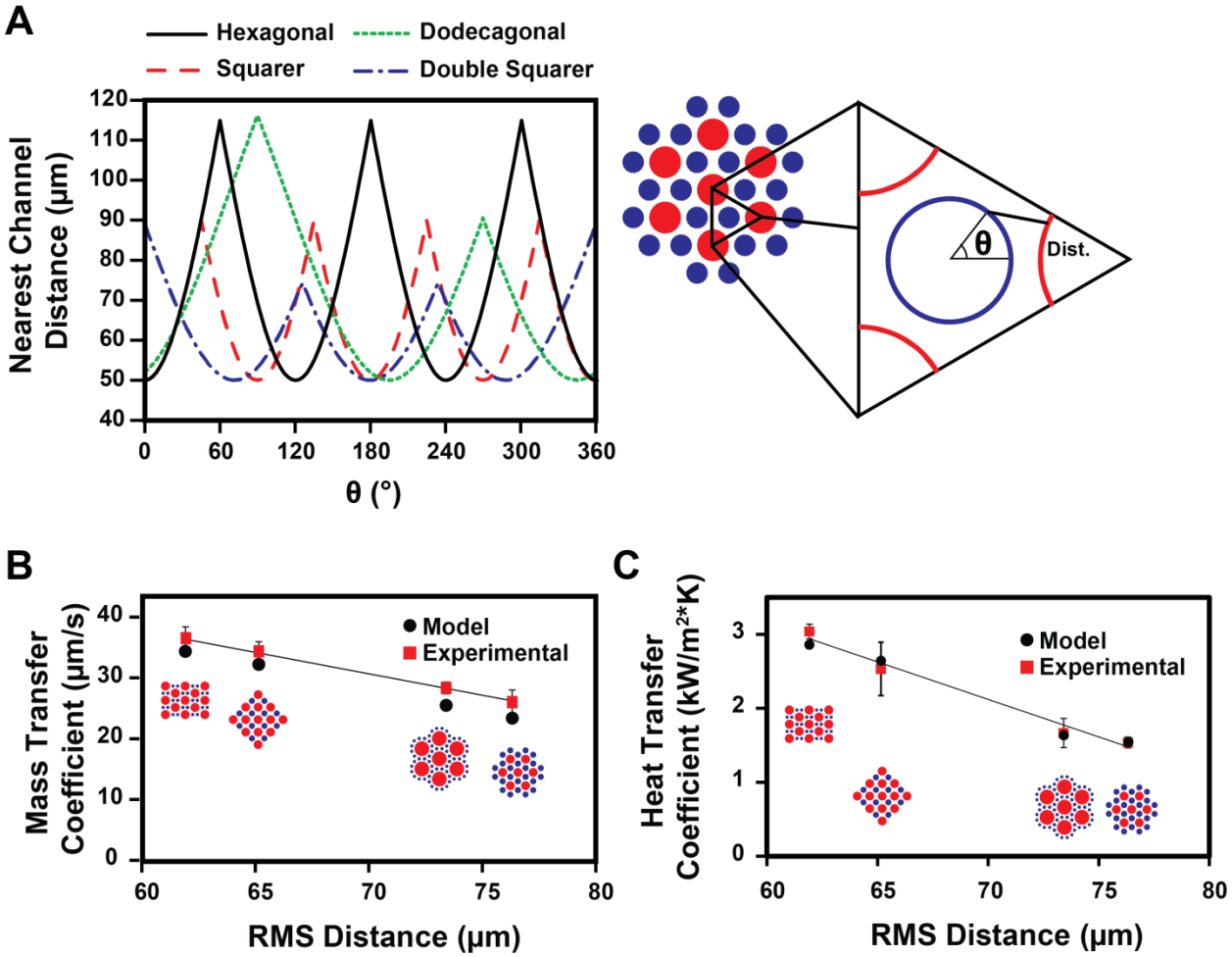

Figure 3.15: Mean distance correlation. (A) Distance calculation. Periodic behavior in determining the nearest channel distances is found. The Hexagonal pattern obtains the largest average nearest channel distance while the Double Squarer obtains the lowest. (B) Mass transfer correlations. A strong correlation between mass transfer coefficients and root mean square (RMS) distances is found. (C) Heat transfer correlations.

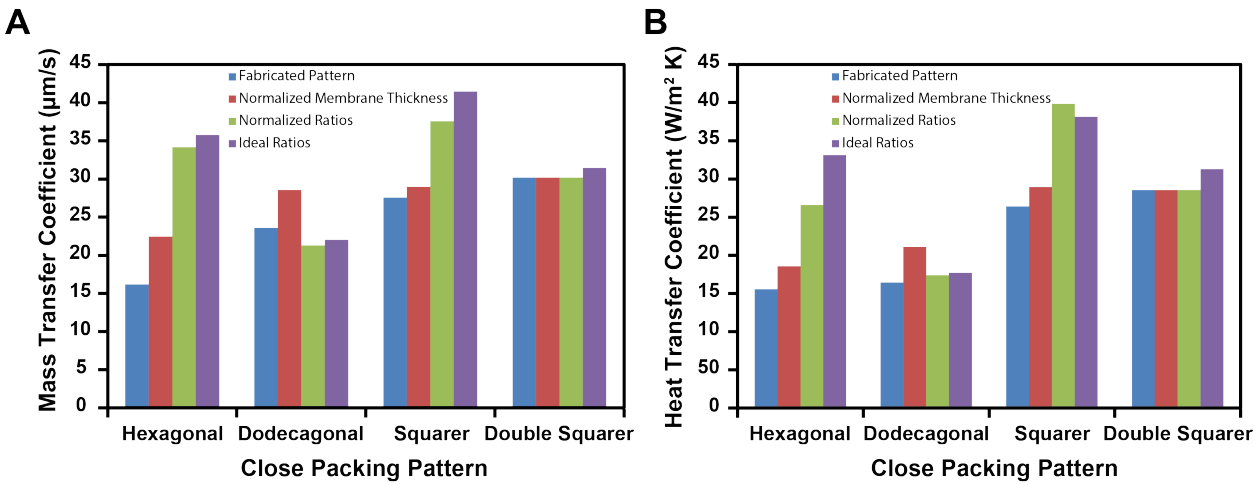

Figure 3.16: Transfer coefficients. (A) Mass Transfer Coefficients. (B) Heat Transfer Coefficients. Fabricated patterns were limited by fabrication. Thicknesses were normalized to 61.9 μm RMS distance between channels. Normalized ratios used 100 μm channels as the smaller channels, 300 μm channels as the larger ones, and maintained normalized RMS distances. Alternatively, ideal ratios between small and large channels were modeled, using 100 μm channels as the smaller ones and maintained normalized RMS distances.

the transfer coefficients maintained similar differences. Next, we examined the effects of normalizing the channel ratios to use 100 μm and 300 μm channel sizes, with normalized RMS distances. Last, we investigated an alternative pattern geometry set where the patterns were normalized to have the same minimum channel size (100 μm), RMS distance (61.9 μm), and larger channel size that matched with the ideal pattern ratio. It should be noted that these other patterns were not currently possible to fabricate due to low minimum inter-channel distances or unavailable fiber sizes. The ideal pattern ratios, normalized minimum channel size, and normalized RMS distances resulted in the Squarer pattern obtaining the highest transfer coefficients.

Last, the transfer coefficients were examined using channel diameters and membrane thicknesses resembling biologically scaled systems. Membrane thicknesses were set to a minimum of ˜1 μm (normalized to 3.8 μm RMS thickness). Minimum channel sizes were set to 5 μm and channel ratios were idealized. Flow rates were decreased by a factor of 100 for mass transfer models. Model lengths were reduced from 8000 μm to 800 μm. Transfer coeffi-

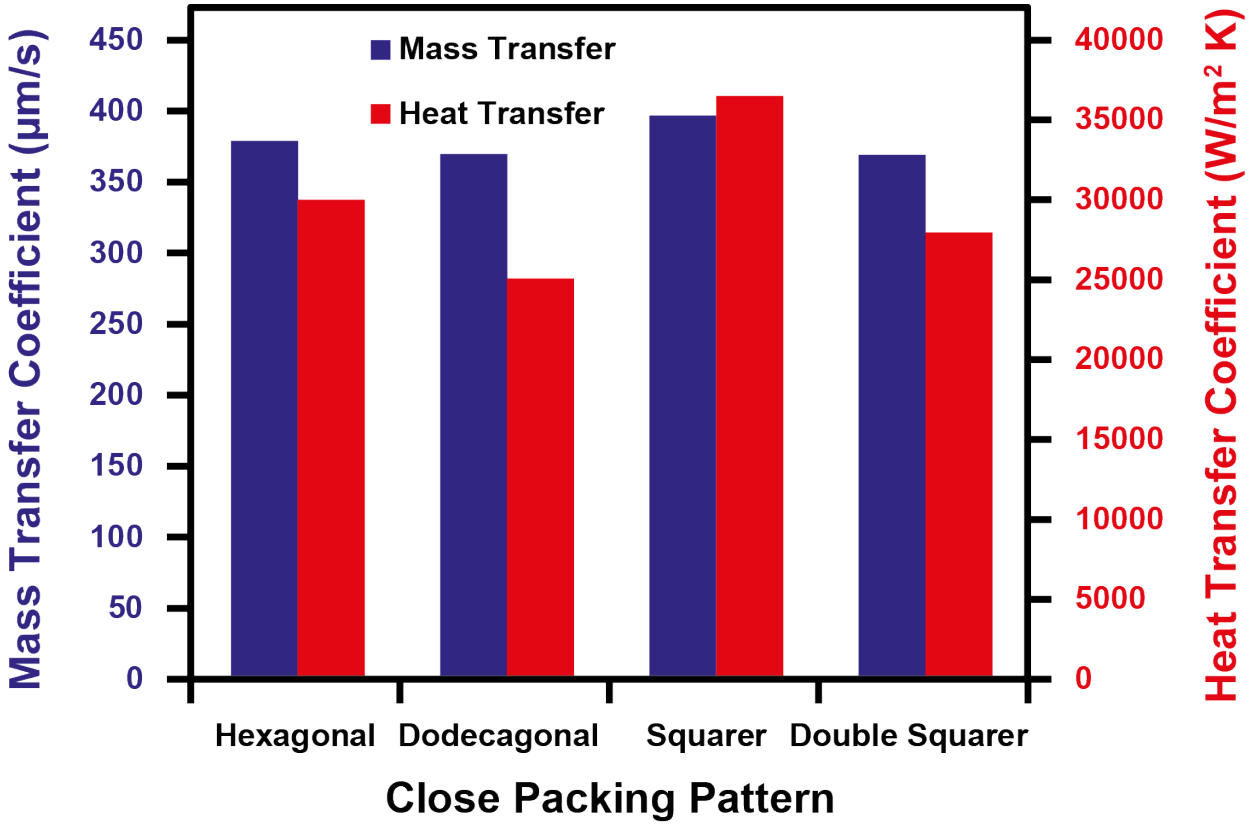

Figure 3.17: Biological scale transfer coefficients. Transfer coefficients were calculated for systems using biological sized channels and membrane thicknesses. 5 μm minimum diameter channels were used with ˜1 μm minimum membrane thickness (normalized to 3.8 μm RMS distance) and ideal channel ratios.

cients increased for all patterns.Trends remained consistant for both mass and heat transfer coefficients, but less pronounced for the mass transfer coefficients.

Bibliography

[1] Maxine A. McClain, Christopher T. Culbertson, Stephen C. Jacobson, Nancy L. Allbritton, Christopher E. Sims, and J. Michael Ramsey. Microfluidic Devices for the High-Throughput Chemical Analysis of Cells. *Analytical Chemistry*, 75(21):5646–5655, November 2003.

[2] Volker Hessel, Holger Lwe, and Friedhelm Schnfeld. Micromixersa review on passive and active mixing principles. *Chemical Engineering Science*, 60(8-9):2479–2501, April 2005.

[3] E Choban. Microfluidic fuel cell based on laminar flow. *Journal of Power Sources*, 128 (1):54–60, March 2004.

[4] A. Brunetti, F. Scura, G. Barbieri, and E. Drioli. Membrane technologies for CO_2 separation. *Journal of Membrane Science*, 359(1-2):115–125, September 2010.

[5] Geeta Mehta, Jay Lee, Wansik Cha, Yi-Chung Tung, Jennifer J. Linderman, and Shuichi Takayama. Hard Top Soft Bottom Microfluidic Devices for Cell Culture and Chemical Analysis. *Analytical Chemistry*, 81(10):3714–3722, May 2009.

[6] Aditya Balasubramanian, Robert Morhard, and Christopher J Bettinger. Shape-Memory Microfluidics. *Advanced Functional Materials*, 23(38):4832–4839, 2013.

[7] C. J. Bettinger, E. J. Weinberg, K. M. Kulig, J. P. Vacanti, Y. Wang, J. T. Borenstein, and R. Langer. Three-Dimensional Microfluidic Tissue-Engineering Scaffolds Using a Flexible Biodegradable Polymer. *Advanced Materials*, 18(2):165–169, January 2006.

[8] Christopher J. Hansen, Scott R. White, Nancy R. Sottos, and Jennifer A. Lewis. Accelerated Self-Healing Via Ternary Interpenetrating Microvascular Networks. *Advanced Functional Materials*, 21(22):4320–4326, November 2011.

[9] Du T. Nguyen, Y T. Leho, and Aaron P. Esser-Kahn. A three-dimensional microvascular gas exchange unit for carbon dioxide capture. *Lab Chip*, 12(7):1246–1250, March 2012.

[10] Du T. Nguyen, Y T. Leho, and Aaron P. Esser-Kahn. The Effect of Membrane Thickness on a Microvascular Gas Exchange Unit. *Advanced Functional Materials*, 23(1):100–106, January 2013.

[11] Ying Zheng, Peter W. Henderson, Nak Won Choi, Lawrence J. Bonassar, Jason A. Spector, and Abraham D. Stroock. Microstructured templates for directed growth and vascularization of soft tissue in vivo. *Biomaterials*, 32(23):5391–5401, August 2011.

[12] Leon M. Bellan, Matthew Pearsall, Donald M. Cropek, and Robert Langer. A 3D Interconnected Microchannel Network Formed in Gelatin by Sacrificial Shellac Microfibers. *Advanced Materials*, 24(38):5187–5191, October 2012.

[13] Leon M. Bellan, Tatiana Kniazeva, Ernest S. Kim, Alla A. Epshteyn, Donald M. Cropek, Robert Langer, and Jeffrey T. Borenstein. Fabrication of a Hybrid Microfluidic System Incorporating both Lithographically Patterned Microchannels and a 3D Fiber-Formed Microfluidic Network. *Advanced Healthcare Materials*, 1(2):164–167, March 2012.

[14] Nicolas Da Mota, David A. Finkelstein, Joseph D. Kirtland, Claudia A. Rodriguez, Abraham D. Stroock, and Hctor D. Abrua. Membraneless, Room-Temperature, Direct Borohydride/Cerium Fuel Cell with Power Density of Over 0.25 W/cm ^{2}. *Journal of the American Chemical Society*, 134(14):6076–6079, April 2012.

[15] J. Cooper McDonald and George M. Whitesides. Poly(dimethylsiloxane) as a Material for Fabricating Microfluidic Devices. *Accounts of Chemical Research*, 35(7):491–499, July 2002.

[16] Pei-Xue Jiang, Ming-Hong Fan, Guang-Shu Si, and Ze-Pei Ren. Thermalhydraulic performance of small scale micro-channel and porous-media heat-exchangers. *International Journal of Heat and Mass Transfer*, 44(5):1039–1051, March 2001.

[17] A. Khademhosseini, R. Langer, J. Borenstein, and J. P. Vacanti. Microscale technologies for tissue engineering and biology. *Proceedings of the National Academy of Sciences of the United States of America*, 103(8):2480–2487, February 2006. WOS:000235554900004.

[18] Ryan P. Lively, Ronald R. Chance, B. T. Kelley, Harry W. Deckman, Jeffery H. Drese, Christopher W. Jones, and William J. Koros. Hollow Fiber Adsorbents for CO $_2$ Removal from Flue Gas. *Industrial & Engineering Chemistry Research*, 48(15):7314–7324, August 2009.

[19] Dong Hyuck Kam and Jyoti Mazumder. Three-dimensional biomimetic microchannel network by laser direct writing. *Journal of Laser Applications*, 20(3):185, 2008.

[20] Matthew D. Determan, Dhruv C. Hoysall, and Srinivas Garimella. Heat- and Mass-Transfer Kinetics of Carbon Dioxide Capture Using Sorbent-Loaded Hollow Fibers. *Industrial & Engineering Chemistry Research*, 51(1):495–502, January 2012.

[21] Willie Wu, Christopher J. Hansen, Alejandro M. Aragn, Philippe H. Geubelle, Scott R. White, and Jennifer A. Lewis. Direct-write assembly of biomimetic microvascular networks for efficient fluid transport. *Soft Matter*, 6(4):739–742, 2010.

[22] Dongliang Wang, K Li, and W.K Teo. Preparation and characterization of polyvinylidene fluoride (PVDF) hollow fiber membranes. *Journal of Membrane Science*, 163(2): 211–220, November 1999.

[23] Dominic T Clausi and William J Koros. Formation of defect-free polyimide hollow fiber membranes for gas separations. *Journal of Membrane Science*, 167(1):79–89, March 2000.

[24] Willie Wu, Adam DeConinck, and Jennifer A. Lewis. Omnidirectional Printing of 3D Microvascular Networks. *Advanced Materials*, 23(24):H178–H183, March 2011.

[25] Gian Luca Morini. Single-phase convective heat transfer in microchannels: a review of experimental results. *International Journal of Thermal Sciences*, 43(7):631–651, July 2004.

[26] Poh-Seng Lee, Suresh V. Garimella, and Dong Liu. Investigation of heat transfer in rectangular microchannels. *International Journal of Heat and Mass Transfer*, 48(9): 1688–1704, April 2005.

[27] Weilin Qu and Issam Mudawar. Analysis of three-dimensional heat transfer in microchannel heat sinks. *International Journal of Heat and Mass Transfer*, 45(19):3973–3985, September 2002.

[28] Sung-Min Kim and Issam Mudawar. Analytical heat diffusion models for different microchannel heat sink cross-sectional geometries. *International Journal of Heat and Mass Transfer*, 53(19-20):4002–4016, September 2010.

[29] John N. Maina, Sikiru A. Jimoh, and Margo Hosie. Implicit mechanistic role of the collagen, smooth muscle, and elastic tissue components in strengthening the air and blood capillaries of the avian lung. *Journal of Anatomy*, 217(5):597–608, November 2010.

[30] Roger C. Wagner, Ritchie Froehlich, Fred E. Hossler, and S.Brian Andrews. Ultrastructure of capillaries in the red body (rete mirabile) of the eel swim bladder. *Microvascular Research*, 34(3):349–362, November 1987.

[31] J B Wittenberg and B A Wittenberg. The choroid rete mirabile of the fish eye. I. Oxygen secretion and structure: comparison with the swimbladder rete mirabile. *The Biological bulletin*, 146(1):116–136, February 1974.

[32] R E Brown, J D Brain, and N Wang. The avian respiratory system: a unique model for studies of respiratory toxicosis and for monitoring air quality. *Environmental health perspectives*, 105(2):188–200, February 1997.

[33] Tom Kennedy. Compact Packings of the Plane with Two Sizes of Discs. *Discrete & Computational Geometry*, 35(2):255–267, May 2005.

[34] L. F. Tth. *Regular Figures*. Pergamon Press, Oxford, 1964.

[35] C. N. Likos and C. L. Henley. Complex alloy phases for binary hard-disc mixtures. *Philosophical Magazine Part B*, 68(1):85–113, March 1993.

[36] J. Molnár. Unterdeckung und überdeckung der ebene durch kreise. *Mathematische Nachrichten*, 2:33–40, 1959.

[37] A. Heppes and J. Molnár. New results in discrete geometry II. *Matematikai Lapok*, 11: 330–355, 1960.

[38] Aaron P. Esser-Kahn, Piyush R. Thakre, Hefei Dong, Jason F. Patrick, Vitalii K. Vlasko-Vlasov, Nancy R. Sottos, Jeffrey S. Moore, and Scott R. White. Three-Dimensional Microvascular Fiber-Reinforced Composites. *Advanced Materials*, 23(32): 3654–3658, August 2011.

[39] Hefei Dong, Aaron P. Esser-Kahn, Piyush R. Thakre, Jason F. Patrick, Nancy R. Sottos, Scott R. White, and Jeffrey S. Moore. Chemical Treatment of Poly(lactic acid) Fibers to Enhance the Rate of Thermal Depolymerization. *ACS Applied Materials & Interfaces*, 4(2):503–509, February 2012.

[40] P. V. Danckwerts. The reaction of CO_2 with ethanolamines. *Chemical Engineering Science*, 34(4):443–446, 1979.

[41] T. C. Merkel, V. I. Bondar, K. Nagai, B. D. Freeman, and I. Pinnau. Gas sorption,

diffusion, and permeation in poly(dimethylsiloxane). *Journal of Polymer Science Part B: Polymer Physics*, 38(3):415–434, 2000.

[42] Jorge M. Plaza, David Van Wagener, and Gary T. Rochelle. Modeling CO_2 capture with aqueous monoethanolamine. *Energy Procedia*, 1(1):1171–1178, February 2009.

[43] James E Mark. *Polymer data handbook*. Oxford University Press, Oxford; New York, 2009.

[44] William M. Haynes, David R. Lide, and Thomas J. Bruno. *CRC handbook of chemistry and physics: a ready reference book of chemical and physical data*. CRC Press, Boca Raton (Fla.); London; New York, 2012.

[45] Erwin D. Snijder, Marcel J. M. te Riele, Geert F. Versteeg, and W. P. M. van Swaaij. Diffusion coefficients of several aqueous alkanolamine solutions. *Journal of Chemical & Engineering Data*, 38(3):475–480, July 1993.

[46] T. L Bergman and Frank P Incropera. *Fundamentals of heat and mass transfer*. Wiley, Hoboken, NJ, 2011.

[47] Bruce Roy Munson, Wade W Huebsch, and Alric P Rothmayer. *Fundamentals of fluid mechanics*. John Wiley & Sons, Inc., Hoboken, NJ, 2013.

[48] Seyed Mostafa Shameli, Tomasz Glawdel, Zhen Liu, and Carolyn L. Ren. Bilinear Temperature Gradient Focusing in a Hybrid PDMS/Glass Microfluidic Chip Integrated with Planar Heaters for Generating Temperature Gradients. *Analytical Chemistry*, 84 (6):2968–2973, March 2012.

Chapter 4

Hierarchical Microvascular Structures

4.1 Introduction

Our work in developing microvascular structures successfully mimicked the basic structure of an avian lung. We precisely positioned the arrangement of microchannels in three dimensions that allowed for efficient counter-current flow of fluids and gasses. However, and avian parabronchus contains an additional hierarchical layer. Rather than a simple membrane, the area surrounding the air pathways contain networks of blood vessels, providing even more surface area for the interaction between gas and liquids. In order to artificially mimic this system, we require two additional technologies in addition to our sacrificial template technologies: the ability to coat a three-dimensional microstructure with a polymembrane polymer and the ability to fabricate a co-continuous template with uniform length features.

4.2 Conformal Coatings

4.2.1 Introduction

The ability to coat and deposit materials onto surfaces is one of the most widely used techniques in materials science.[1–21] Coatings can improve the properties of many materials by changing their surface properties, such as in applications ranging from anti-corrosion to semiconducting.[1**?** –5] Processes such as chemical vapor deposition, atomic layer deposition, solution deposition, and layer-by-layer coatings allow for nano-scale depositions.[6–9] Other techniques such as spin coating, dip coating, and electroplating can form thicker coatings.[10–17] For separations applications involving polymeric membranes, a common method is hollow fiber spinning to template the polymeric membrane using solvent dissolution.[18–21] However, few techniques exist that form polymeric membranes with complicated 3D topologies.

Here we report a technique to fabricate microvascular membrane structures through the entrapment of a polymer membrane into a poly-lactic acid (PLA) template structure. No direct modification of the surface is necessary, making this technique applicable to a wide variety of materials. In order to coat complicated and fine structures, we sought a technique that did not require thin layer coatings, deposition, or reactivity at the surface. We found that the entrapment of biomolecules and catalysts onto the surfaces of poly-lactic acid by selectively swelling the surface to incorporate the materials had to potential to develop into a new coating method.[22–24] This procedure was modified to accommodate a variety of polymeric membrane materials. In the templating process, a swollen PLA template surface is used to entrap a membrane precursor from solution. Once entrapped, the precursor is cured to form a membrane conformed to the polymer surface. The polymer template can then be removed, leaving behind the newly formed hollow membrane in the same topology as the original template structure.

For this process, we have characterized the membrane thickness as a function of coating solution composition, structure sizes, and residence times and found that each variable can be used to control membrane thickness ranging from 400 nm to 4 μm. These studies were primarily performed using polydimethylsiloxane (PDMS) as the membrane material, but we also found that many commercial polymers are compatible with the entrapment technique. We demonstrated its application in various 3D structures including 3D printed templates and phase separated microstructures with feature sizes ranging from the millimeter range to the micron range. The membranes are strong enough to retain liquids and have porosities suitable for the selective separation of gases.

To perform an entrapment, an appropriate coating solution must be comprised of four elements: template (PLA), template solvent, template non-solvent, and membrane precursor (Figure 4.1). A pre-fabricated microstructure is placed into the coating solution, which swells the PLA template without fully dissolving it, and results in a thin area in which the template is swollen. The membrane precursor enters this swollen region and becomes entrapped when the surface de-swells. The structure is then de-swelled by either rinsing in a non-solvent, or by centrifugation to remove the coating solution. Once the template has been de-swollen, the membrane precursor can be cured, forming a 3D conformal coating of the template polymer structure. In this technique, several parameters affect the resulting membrane including the solution composition, template residence time, and the characteristic size scale of the template. PLA was chosen as the template, as it can be selectively removed through solvent dissolution or the Vaporization of a Sacrificial Component (VaSC), leaving behind a membrane shaped from the initial template.[25–27]

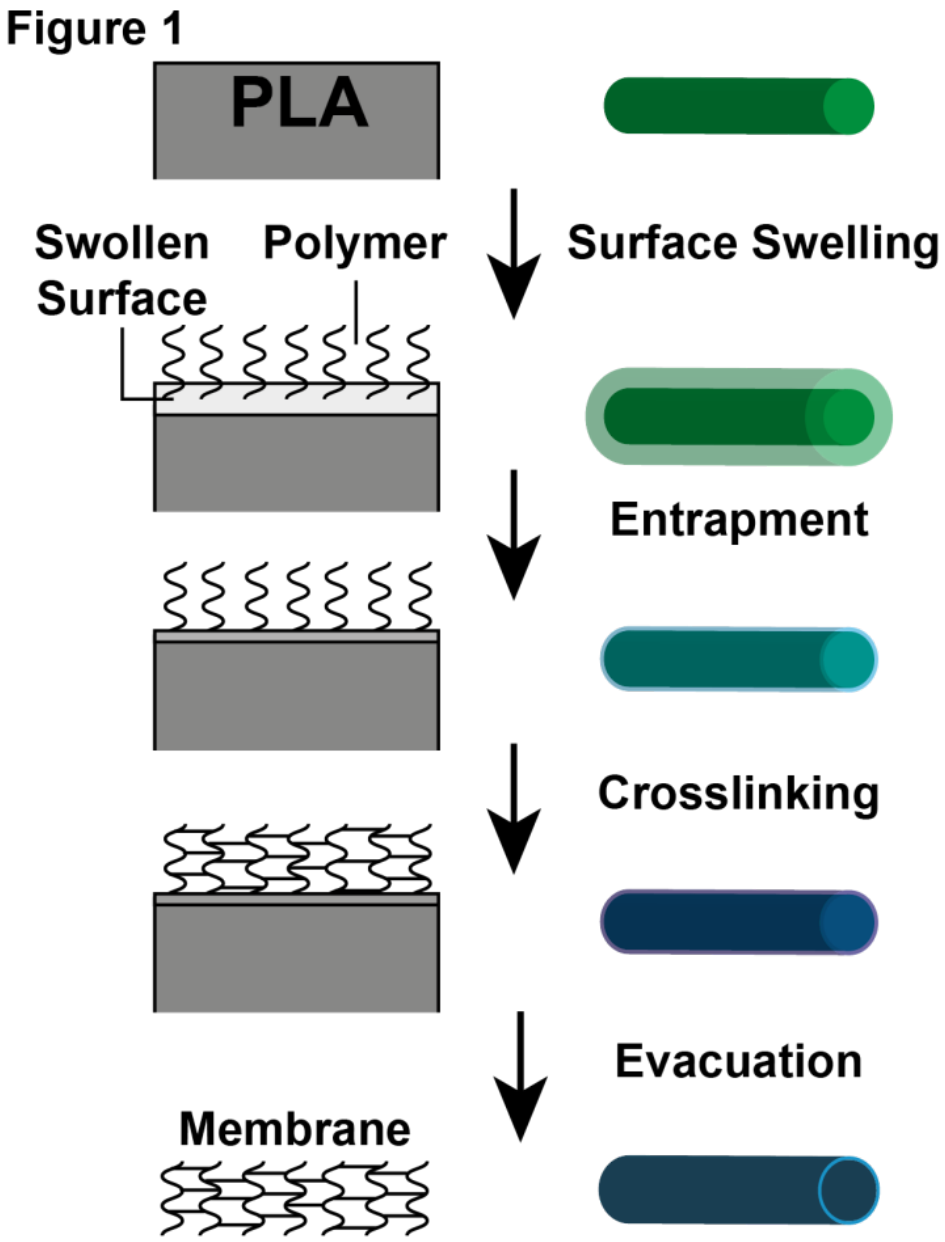

Figure 4.1: Entrapment process schematic. In the first step of the entrapment process, a polymer template is swollen in a solvent/nonsolvent mixture containing the membrane precursor. Next, the polymer template is de-swelled, entrapping the membrane precursor. The precursor is then cured to form the membrane at the surface of the template. Last, the template can be removed, leaving behind a hollow membrane conformed to the topology of the template.

4.2.2 Experimental

Materials: Polydimethylsiloxane (PDMS) was obtained from Dow Corning. Dioxane, hexane, acetone, isopropanol, N-Methyl-2-pyrrolidone (NMP), Dichloromethane (DCM), chloroform, monoethanolamine, polycaprolactone (average Mn 45,000), and poly(vinyl alcohol) (average Mw 85,000-146,000) were obtained from Sigma Aldrich. Dow Corning 736 Sealant, epoxy, urethane, and acrylic adhesives were purchased from McMasterCarr (part numbers 74515A32, 7541A83, 7448A22, and 75395A65, respectively). RTV 430 was obtained from Momentive. Poly(lactic) acid was supplied by Teijin Monofilament. Matrimid®was supplied by Hunaid Nulwala, Carnegie Mellon University.

General Entrapment Coating Procedure (for PDMS): PDMS precursor is made by mixing the PDMS base composed of alkene terminated siloxanes with the curing agent, a standard platinum hydro-silation chemistry, in a 10:1 ratio. The precursor is degassed under vacuum for 10 minutes. Next, a 10 mL ternary solution consisting of the precursor, dioxane (solvent), and hexane (non-solvent) is mixed at the desired concentrations. A 2 cm length of PLA fiber with the desired diameter, ranging from 100 μm to 500 μm, is placed into the coating solution. After times ranging from 1 minute to 2 hours, the fiber is removed and rinsed in hexane for 5 seconds. Last, the coated fiber is then heated to 85 °C for 30 minutes to cure the PDMS membrane.

Thickness Characterization: We characterized the thicknesses of the newly formed membranes with respect to the solution composition, residence time, and template size scale. The characterizations were conducted using PDMS as the membrane material and 300 μm PLA microfibers, pre-treated for the VaSC microfabrication technique, as the template structures.[27]27 The VaSC technique allows for the depolymerization of the PLA template, converting the solid template into gas under heat and vacuum. The general entrapment coating procedure was modified to accommodate a range of times, sizes, and compositions.

The coated fibers were placed in a secondary support casing of PDMS and removed via VaSC at 200 °C, resulting in a hollow microchannel within PDMS. Cross sections of the micro-channel were imaged using scanning electron microscopy (SEM). We distinguished the conformal membrane as it had different grain characteristics than the secondary support when imaged under SEM. We examined the cross-sections for quantitative measurements of the membrane thicknesses at several locations along the fiber circumference. Data was represented as average ± standard deviation (n=10). Using FTIR spectroscopy, the free-standing membranes fabricated through the entrapment method were confirmed to be PDMS, and not a mixture of PDMS and PLA (Appendix A.4).

Coatings on 3D Printed Structures: The 3D printed PLA templates were printed by RapidTech, a UCI user institution, using an Airwolf AW3D V5.5 3D printer. Designs for the 3D templates were obtained from Thingiverse (thingiverse.com). An initial PDMS membrane was coated onto the templates using a 12.5:75:12.5 (PDMS:Hexane:Dioxane) solution composition. The coating was performed with a residence time of 1 hour in the coating solution at an elevated temperature of 65 °C. This would partially cure the entrapped precursor, allowing for a thicker membrane and clearer visualization. The membrane was then fully cured at 85 °C for 30 minutes. For some experiments, an additional coating was added to increase the thickness of the membrane. For these experiments, two additional coatings of PDMS were performed using a similar coating method. However, the solution composition was 9:36:55 (PDMS:Hexane:Isopropanol) in order to swell the initial PDMS membrane rather than the PLA template. Once the PLA templates were coated with the additional membranes, sections of the membranes were removed to allow the PLA to exit the membrane. The PLA templates were removed using solvent dissolution in dioxane for over 24 hours. Solvent dissolution was used rather than VaSC since the solvent would readily enter the resulting membrane and aid its three dimensional suspension for clear visualization. The resulting hollow membranes were transferred to acetone for enhanced visual clarity due to the larger difference in index of refraction between PDMS and acetone over dioxane.

3D Microstructure Coatings: Micro-structured PLA templates were fabricated through the temperature induced phase separation of PLA.[28, 29] In temperature induced phase separation, a homogenous mixture of a polymer and solvent is made at an elevated temperature. Upon letting the homogenous mixture cool, the mixture becomes thermodynamically unstable and separates into a polymer lean phase and a polymer rich phase. Under the proper conditions, these phases can separate into a bi-continuous structure. Briefly, 9 wt% PLA was dissolved in a dioxane/water mixture (87:13 dioxane:water) at 85 °C. The solution was then phase separated by lowering the temperature to 15 °C for 1 hr. Last, the solution was frozen by immersing it into liquid nitrogen and the resulting frozen material was lyophilized for 8 hours to remove the dioxane and water, leaving a microporous bicontinous PLA. Following the fabrication of the template, multiple coatings were deposited onto the template following the procedure given for 3D-printed structure coatings. The coating solutions were removed using centrifugation as the dense pore structures of the template made solvent exchange very slow. The templates were then removed using the VaSC process.

Characterization: Characterization of membrane topologies were performed using SEM and X-ray computed tomography (μCT). SEM images were acquired using a Philips XL-30 FEG SEM. Three dimensional μCT images were acquired using an Xradia VersaXRMTM 410 CT system under 20X magnification. FTIR spectroscopy was conducted using a PerkinElmer System 2000 FTIR. Image processing was performed using the ImageJ image processing and analysis software. 3D reconstruction of the μCT slices were performed using the BoneJ plugin for ImageJ.

4.2.3 Discussion

Our primary interest was in controlling membrane thickness, so we examined the composition of the ternary solvent-nonsolvent-membrane precursor mixture and its effect on membrane

thickness (Figure 2). PDMS membranes were coated onto 300 μm diameter PLA fibers using ternary compositions (with ranges from 10-60% PDMS, 30-80% hexane, and 10-60% dioxane, by volume) with a residence time of 1 hr. Hexane was chosen as the solvent for PDMS while dioxane was the solvent for PLA. Other combinations of solvents might also be used. We found that in order to form a coating, all components of the ternary mixture must be miscible and that the template must not dissolve the template within the coating time scale. The mixture can step out of this coating region when the mixture contains a low concentration of hexane, high concentration of PDMS, or high concentration of dioxane. As a general trend, the thickest membranes occur close to the boundary between the coating region and the dissolution region. However, the thickness decreases once the mixture enters the dissolution region. Our operating hypothesis is that a smaller entrapping layer is being formed. With too high a dissolving solvent percentage, the outer edge of the entrapping layer may completely dissolve, resulting in a smaller entrapping layer once the fiber de-swells. (Figure 4.2)

Next, we examined the effects of the characteristic size of the template structure by coating fibers of different diameters, ranging from 100 to 500 μm. The coating residence time was 1 hr and the solution composition was 33:40:27 (PDMS: Hexane: Dioxane, volumetric ratio), a pairing we determined from previous experiments would create membranes of 1.7 $\pm$ 0.4 μm thickness in a 300 μm fiber. As the characteristic size increases, the thickness of the membrane also increases (Figure 4.3) ranging from 0.7 to 3.8 μm. Though not seen in these experiments, there is likely an upper limit to the change in membrane thickness with respect to the characteristic size. The maximum thickness should correspond roughly to the maximum swollen state of the template.

Last, we examined the effects of residence time spent in the entrapment solution. The coatings were performed on 300 μm diameter microchannels using a solution composition of 16:68:16 (PDMS : Hexane: Dioxane, volumetric ratio). This composition was chosen for its lower dioxane concentration so that the fiber would not dissolve during the range

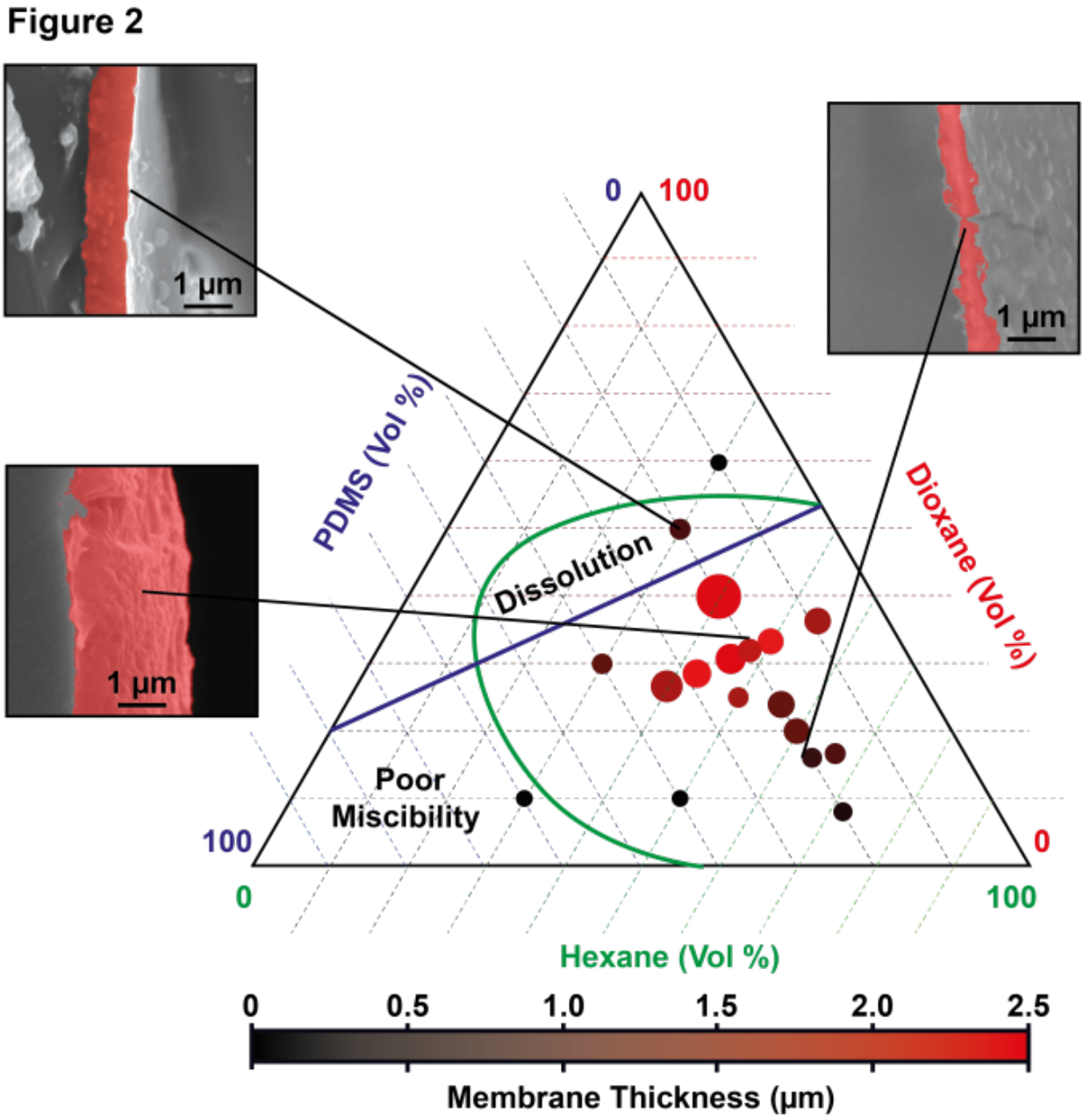

Figure 4.2: Effect of coating solution composition. The three parts of the coating solution are represented in a ternary plot of the solvent (dioxane), non-solvent (hexane), and membrane precursor concentrations (PDMS). Data is presented as average ± standard deviation (n=10). The size of the data points indicates the uncertainty in the thickness measurements, with larger circles having larger uncertainties. Above a threshold solvent concentration, the polymer template can dissolve, resulting in no membrane formation. When the composition is too high in the nonsolvent (if the precursor is not miscible in the nonsolvent), a region of poor miscibility exists which prevents the entrapment of the precursor. Conditions of good miscibility and large swelling (but not dissolution) are necessary to achieve the thickest membranes. For clarity, membranes are false colored red in SEM images.

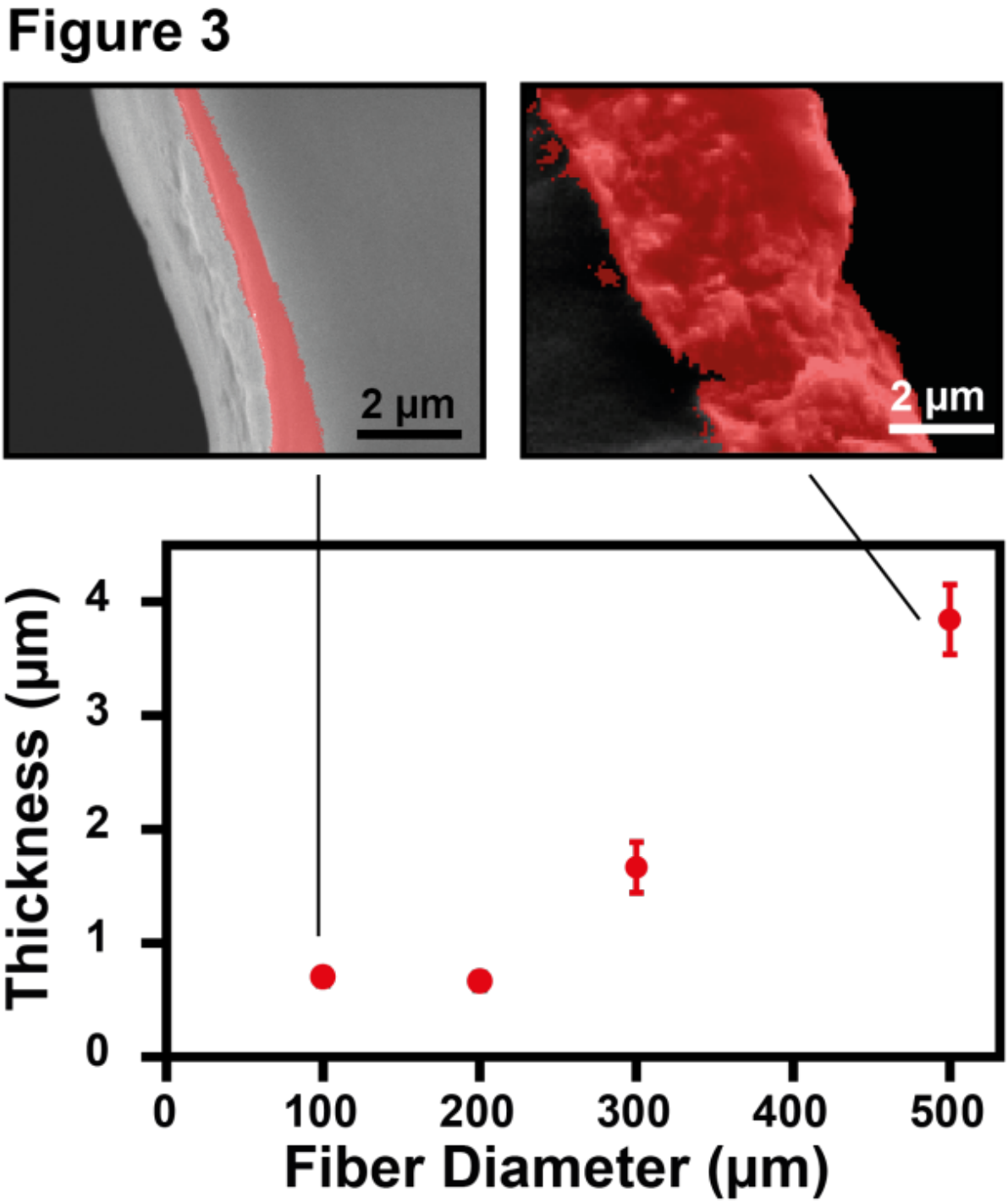

Figure 4.3: Template size scale. Several diameter PLA fibers were coated with the PDMS membrane. The thickness of the resulting membrane was measured. As the fiber diameter increased, so did the membrane thickness. Data is presented as average ± standard deviation (n=10). For clarity, membranes are false colored red in SEM images.

of residence times. Here, we observed that as the residence time increases, so does the membrane thickness (Figure 4.4). The membrane thicknesses were between 0.5 to 1.4 μm for residence times ranging from 1 to 120 mins. Unfortunately, longer residence times resulted in less uniform membranes (uncertainties increasing from $\pm$ 0.1 μm to $\pm$ 0.4 μm). Our current hypothesis is that the increased residence time creates a larger intermediate region of swollen PLA. When the region de-swells, the volume of entrapped polymer must return to the same initial volume. This larger change likely results in a decrease in uniformity.

After characterizing this technique with respect to the solution composition, characteristic size scale, and residence time, we tested the scope of polymers amenable to our solution coating technique. These polymers included other silicon-based rubbers, two-part adhesive epoxy mixtures, and conventional condensation polymers (Table 4.1). However, all of these employed the same general method of entrapping the membrane material in the template using a solvent-nonsolvent-membrane precursor solution. The membranes were coated onto 300 μm PLA fibers using a solution composition of 12.5:75:12.5 (membrane precursor: solvent: nonsolvent, volumetric ratio). Due to the different membrane materials, some had smaller miscibility regions. This composition was chosen to keep all membrane materials within the miscibility region. As we only wanted to verify membrane formation, the fibers were removed using solvent dissolution of the fibers. The presence of a hollow tube confirmed the membrane formation (Figure 4.7). The many different fabricated polymer membranes confirmed that this technique is compatible with a wide range of substrates, beyond the initial characterization of PDMS membranes. These polymeric membranes might find potential uses in high-surface area supports for separations, catalysis, and desalinization.

We then demonstrated the versatility of the coating method for various template geometries by coating a range of complicated 3D structures. One complicated structure formed was a helical microchannel pair (Figure 4.8). Two template PLA fibers are coated to form an initial membrane and then twisted together to form the helix. The fibers are surrounded

Figure 4

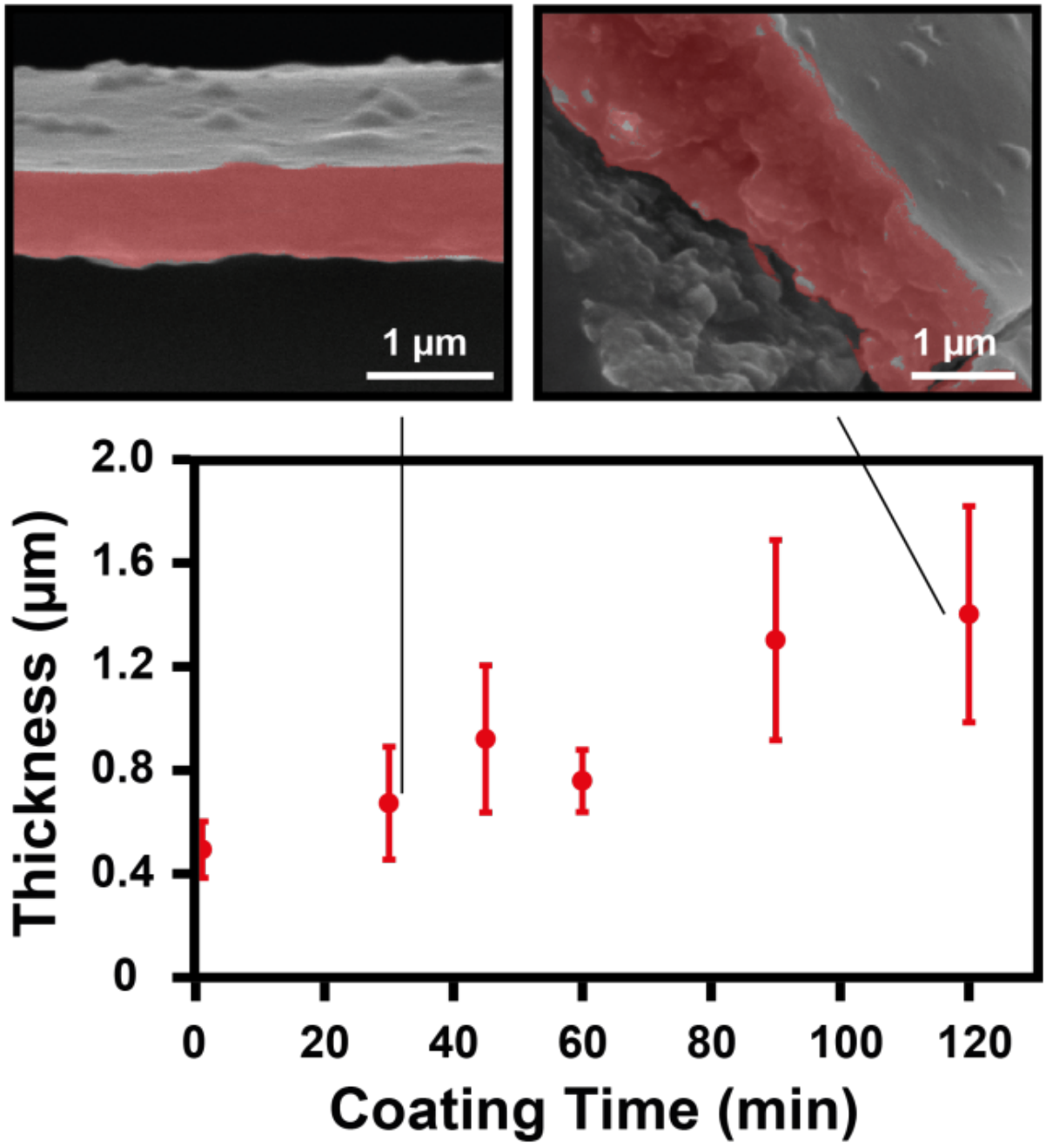

Figure 4.4: Template size scale. Several diameter PLA fibers were coated with the PDMS membrane. The thickness of the resulting membrane was measured. As the fiber diameter increased, so did the membrane thickness. Data is presented as average ± standard deviation (n=10). For clarity, membranes are false colored red in SEM images.

Membrane Base	Template Solvent	Template Nonsolvent
PDMS	Dioxane	Water
PDMS/PIM[30]	Dioxane	Hexane
Poly(vinyl) alcohol	Dioxane	Water
Polycaprolactone	Chloroform	Water
Nylon	Dioxane	Hexane/Water
Matrimid	DCM	NMP
Acrylic	Acetone	Hexane
Epoxy	DCM	Isopropanol
Polyurethane	DCM	Hexane
Dow Corning 736 Sealant	Dioxane	Hexane
Silicon RTV 430	Dioxane	Hexane

Table 4.1: Other entrapment membranes. A general screen of other possible membrane materials was conducted in order to determine if the entrapment method of membrane coating was a general technique. Some mixtures displayed poor miscibility, but still formed a coating.

by a support of bulk PDMS and removed using VaSC. The two resulting microchannels remain in close contact, but are separated by the initial membrane formed by the coatings with an estimated separation of 5 μm. Two different color dyes were flowed through each microchannel to confirm that there was no microscale leaking between the two microchannels. The ability to mechanically position separated microchannels at sub-micron distances can have potentially useful applications in microvascular designs.

We also used the helical structure to check for the presence of defects in the membrane by measuring its gas permeability. If defects were present, they would result in higher gas permeability than predicted for the membrane material. The permeability of the membrane was determined by measuring the mass transfer rate of CO_2 from one channel to the other in the pair using a colorimetric detection method.[25, 26] The membrane was calculated to have a permeability of 4300 Barrer, which is within the range of reported PDMS permeabilities.[20, 21] We also examined a microvascular system with known defects caused by the over-etching of the PDMS membrane.[26, 31] When defects are known to be present, the permeability was calculated to be 6100 Barrer (Figure 4.8).

We then determined if our technique was compatible with 3D printing by fabricating sets of hollow membrane structures using 3D printing of PLA (Figure 4.5). Following the entrapment of PDMS onto the 3D printed structures, the PLA was dissolved, leaving behind a hollow shell of the structure. These structures represented the largest size scale of the membrane coating process (5 mm). Multiple coatings of PDMS were also applied to these structures to aid in visual clarity and resulted in membrane thicknesses of 10 μm. The multiple coatings were obtained using a ternary coating solution designed to swell the initial PDMS coated layer rather than the PLA surface (PDMS, Hexane, and Isopropanol). This approach provides a unique pathway to fabricate hollow microstructures that could not otherwise be 3D printed, with potential uses in fields such as tissue engineering.

The last demonstration of the entrapment technique allowed for the coating of high specific surface area PLA formed through thermally induced phase separation (Figure 6).[28, 29] In thermally induced phase separation, a polymer/solvent/nonsolvent solution can phase separate to create a highly interconnected polymer network. Under optimal conditions, this network can be completely bi-continuous (spinodally phase separated), allowing for the formation of a conformal membrane structure. When followed by lyophilization and the removal of the solvent/nonsolvent mixture, the polymer retains this form and obtains a high specific surface area. These structures were coated with PDMS and evacuated to leave behind a hollow membrane microstructure. SEM imaging confirmed the presence of a conformal membrane microstructure. This allows for the creation of a free-standing, membrane structure with an estimated specific surface area of 57,000 m^2/m^3. The specific surface area was calculated using 3D reconstruction of the μCT slices. The image processing software automatically calculates the surface area of the 3D object and while the volume is the μCT scan volume. Surface areas were set as the interface between the membrane and air. However, the presence of defects in this membrane has not been verified.

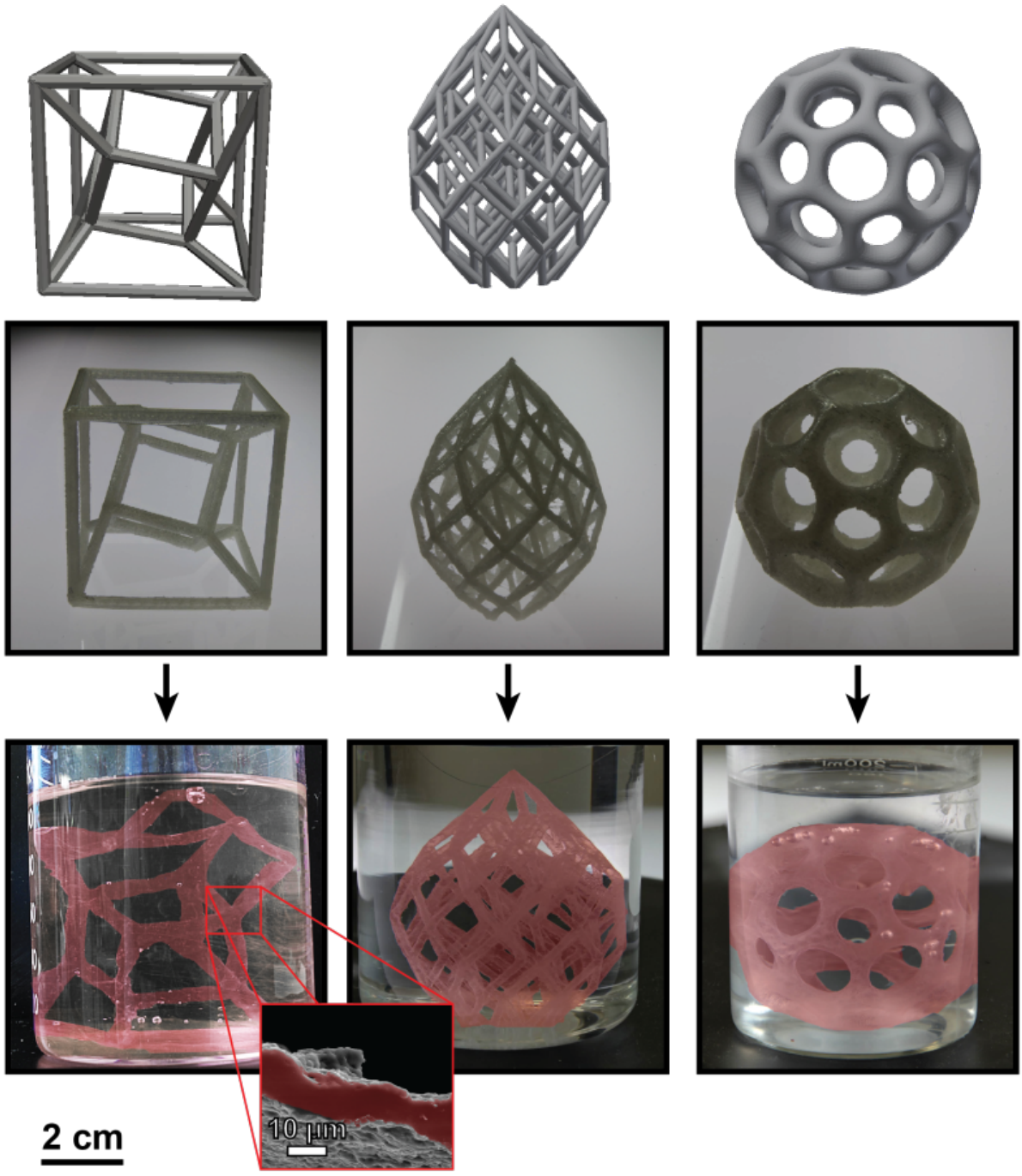

Figure 4.5: 3D printed template coatings. Using a 3D printer, several three-dimensional PLA structures were formed. Multiple coatings of PDMS were formed around these structures and the templates were evacuated leaving behind hollow membrane structures. The membranes were left in acetone and false colored red to maintain and highlight the membrane structure. For clarity, membranes are false colored red in SEM images.

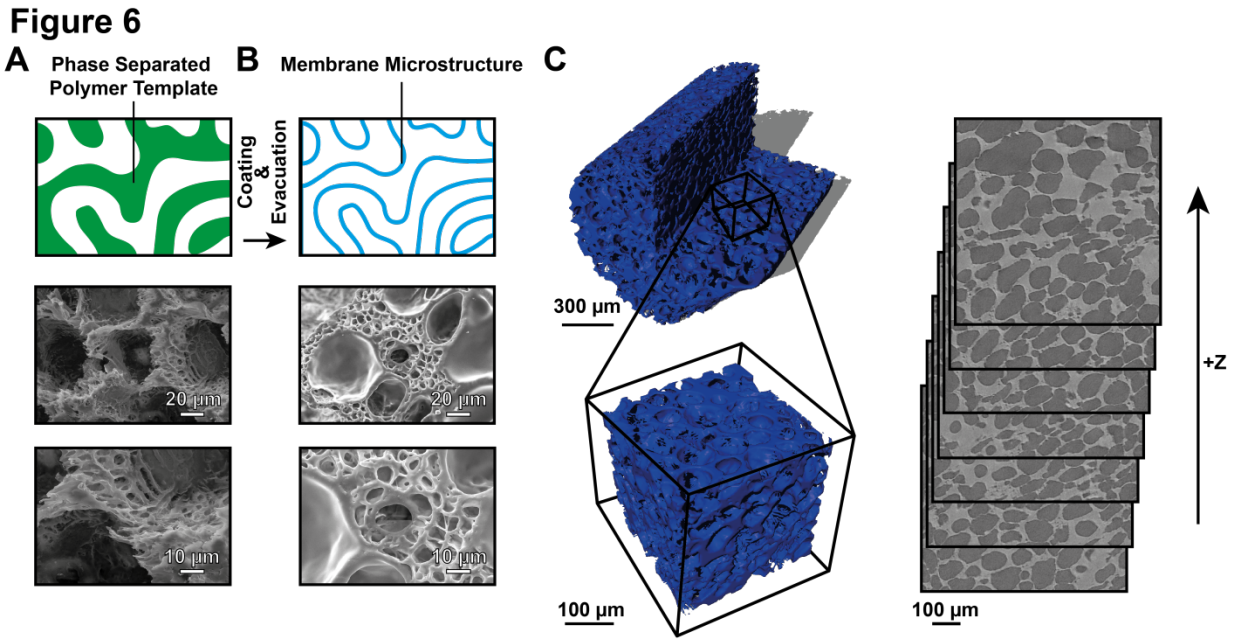

Figure 4.6: Thermally induced phase-separated template coatings. (A) Three dimensional microstructures were formed by thermally inducing phase separation of PLA, resulting in a highly interconnected and three-dimensional polymer microstructure. (B) Evacuated membrane structure. The thermally phase-separated structures were coated with PDMS and the templates were removed through the VaSC technique. (C) μCT membrane structure. A three-dimensional view of the template membrane structure is shown. The specific surface area of the structure was calculated using the BoneJ plugin for ImageJ during 3D reconstruction.

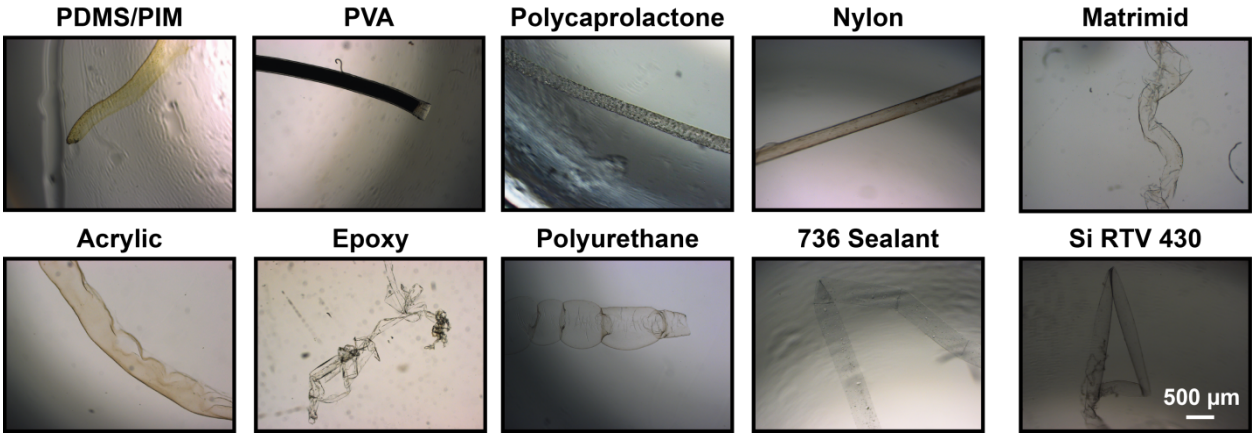

Figure 4.7: Hollow membranes. A variety of membranes for entrapped onto the surface of a PLA fiber template. The template was subsequently removed. The remaining membrane was imaged on an optical microscope and confirmed the presence of the coating.

4.2.4 Other Membrane Materials

A range of membranes separate from PDMS were coated around 300 μm diameter PLA fibers to determine the generality of the coating technique. For most membrane materials, the PLA templates were removed using solvent dissolution in dioxane for 24 hr. For membranes formed with nylon, matrimid, and polycaprolactone, the PLA template fibers were removed using 2 M NaOH for 72 hr. The polyvinyl alcohol (PVA) coated template was not fully evacuated during the 24 hr period in dioxane due to PVAs impermeability to dioxane. However, partial evacuation was observed.

4.2.5 Membrane Defect Detection

Defects in the membranes were detected using a colorimetric method of measuring mass transfer through the membrane. A helical membrane is fabricated with microchannels on either side of the membrane (Figure 4.8). CO_2 flowed through the one side of the membrane while monoethanolamine was loaded into the other side. CO_2 diffuses through the membrane and reacts with the monoethanolamine, forming a carbamic acid and lowering the pH of

the solution. The change in pH can be observed using a pH sensitive dye to quantify the transport of CO_2 through the membrane. Using phenolphthalein as the pH sensitive dye, the color shift occurs when there is 0.4 M MEA remaining to capture the CO_2 (2250 M CO_2). The change in concentration of MEA occurs as an exponential decay. The time to reach the concentration of 0.4 M MEA can then be used to find the initial rate of change in concentration and use as an approximate to the steady state conditions which is used to calculate the initial CO_2 flux. Using the CO_2 flux, mean membrane thickness, and membrane surface area, the permeability of the membrane can be estimated.

C(t) = Remaining MEA concentration (mol/m^3)

$t_{1/2}$ = Time to reach 50% color change (0.4 mol/m^3) (s)

t = time (s)

n_m = Number of MEA channels

r_m = MEA channel radius (m)

n_c = Number of CO_2 channels

n_m = CO_2 channel radius (m)

d = Nearest channel mean distance (m)

C(t)=$4900e^{\frac{ln0.0826}{t_{1/2}}} * t$

$$P = -\frac{\delta C(t)}{\delta t}|_{t=0} * \frac{1molCO_2}{2molMEA} * \frac{n_m \pi r_m^2}{n_c 2\pi r_c} * \frac{1kmol}{1000mol} * \frac{1}{101325Pa} * d * \frac{1Barrer}{3.348\times10^{-10}} \frac{m^2 sPa}{kmolm}$$

A previous report determined the mass transfer rate of a microvascular gas exchange unit with varying membrane thicknesses1. These thicknesses were controlled using an etching method. When the thicknesses decreased below 25 μm, defects in the membrane were known to appear. Using the mass transfer rates of the etched membrane, we found that the ap-

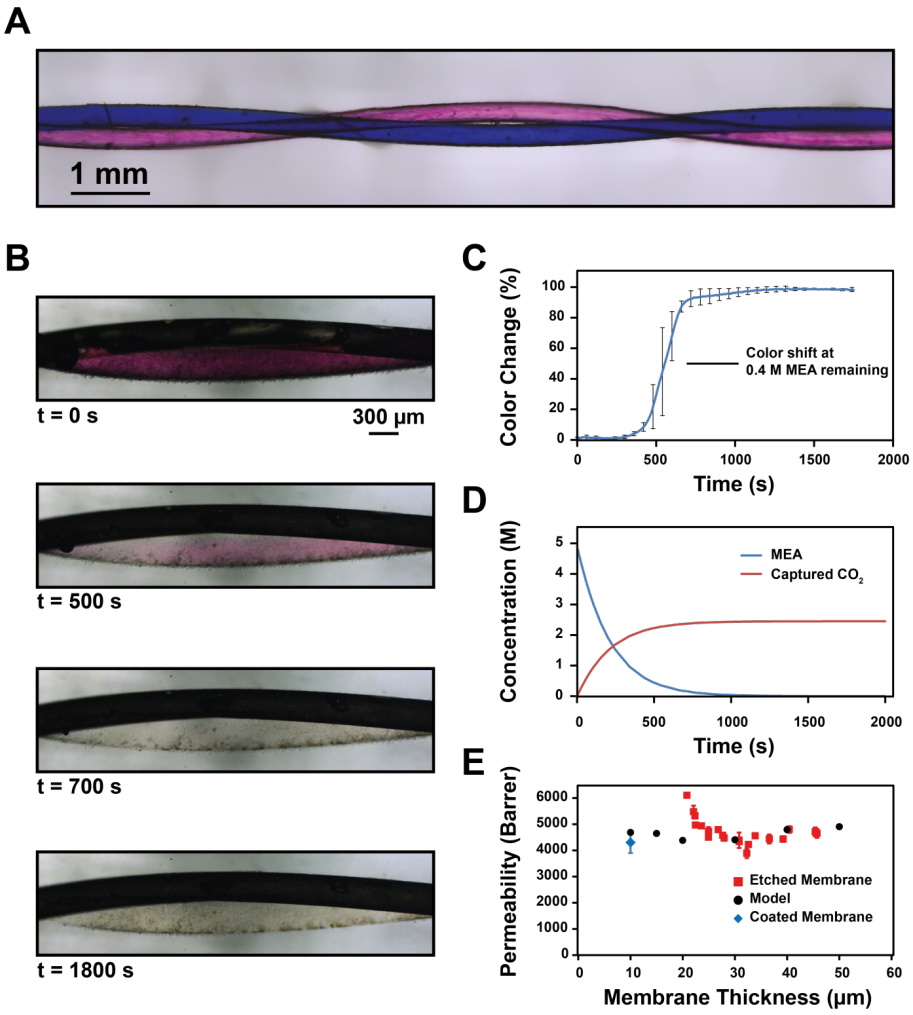

Figure 4.8: Permeability Measurements. (A) Helical microchannel. A helical microchannel system was formed by coating two 300 μm diameter fibers, twisting them together, and embedding the system in additional PDMS. Pink and blue dye are flowed through each channel to demonstrate their separation by the coated membrane. (B) Helical structure mass transfer measurements. A pH sensitive dye detects the absorption of CO_2 into MEA. The decrease in pH shifts the color of the dye from dark pink to clear. (C) Helical structure mass transfer data. The color change of a pH sensitive dye is used to measure the mass transfer of CO_2 from one microchannel to another, with a coated membrane in between the microchannels. The 50% color change corresponds to 0.4 M unreacted MEA. (D) Helical structure model data. A model was developed that predicts the change in MEA and CO_2 concentration within a microvascular mass transfer unit. The decrease in MEA concentration occurs as an exponential function. (E) Permeability data. The model predicts a permeability of 4600 Barrer, agreeing with literature values for PDMS. In the etched membranes, defects begin to appear near a 25 μm membrane thickness which correspond to higher permeability. In the helical structure, the permeability is 4300 $\pm$ 400 Barrers, agreeing with the model and literature values. This indicates that the membrane was defect free.

Concentration (% vol)			Thickness (μm)
Dioxane	Hexane	PDMS	
25	50	25	1.61 ± 0.09
20	60	20	1.00 ± 0.21
17	67	17	0.82 ± 0.10
16	64	20	0.59 ± 0.05
36	55	9	1.60 ± 0.23
33	50	17	2.43 ± 0.22
31	46	23	2.16 ± 0.32
29	43	29	2.38 ± 0.28
27	40	33	1.65 ± 0.36
8	72	20	0.34 ± 0.05
16	64	20	0.58 ± 0.08
24	56	20	1.01 ± 0.24
32	48	20	1.88 ± 0.16
40	40	20	2.16 ± 0.66
50	30	20	0.78 ± 0.10
30	30	40	0.94 ± 0.09
60	30	10	0.00 ± 0.00
10	50	40	0.00 ± 0.00
10	30	60	0.00 ± 0.00

Table 4.2: Entrapment Solution Composition Summary

pearance of defects correspond to an increase in membrane permeability. A computer model was also developed for this system and found that, as expected, the permeability should not change with the membrane thickness. The helical structure with a coated membrane was found to have the expected CO_2 permeability of PDMS, indicating that no defects were present in the membrane.

4.3 Polymerization Induced Phase Separation

4.3.1 Introduction

A hierarchical template is also required in order to fabricate a hierarchical microvascular structure, in conjuncture with three-dimensional conformal coatings. Several methods already exist for the fabrication of porous polymer scaffolds,[x-x] however few obtain similar morphological similarities to natural systems such as the avian lung. Further limitations arise in trying to find a fabrication method amenable to sacrificial fabrication techniques. Here we use polymerization induced phase separation (PIPS) in order to create a hierarchical template of polylactic acid. We were controlled the structure of the template through solution compositions and annealing times and obtained co-continuous three-dimensional microstructures.

4.3.2 Experimental

Materials: Styrene was obtained from Sigma Aldrich. Poly(lactic) acid(PLA) was supplied by Teijin Monofilament.

Template Fabrication: Poly(lactic) acid and styrene were mixed in set amounts, with PLA content ranging from 25 to 50 wt.%. The mixtures were heated to 100 °C for 4 hours to fully dissolve the PLA in the styrene. After full dissolution, the temperature was raised to 140 °C for 12 hours to polymerize the styrene to polystyrene (PS) and induce the phase separation of the PLA. The cured PLA\PS composite was then annealed at 190 °C for a set amount of time, varying between 0 to 120 minutes. Last, the PS was selectively removed from the composite material by dissolving it in cyclohexane. The cyclohexane was refreshed every 2 hours for 48 hours.

Hierarchical Template Fabrication: A square packed arrangement of stainless steel wires were set in place using PDMS mold. A PIPS template was created using 33 wt.% PLA. The template was not initially annealed and the PS was not yet selectively removed. The small portions of the template were placed over the wire pattern and placed in an oven at 190 °C for 2 hours to anneal. During the annealing time, the mixture liquidized and surrounded the wire pattern. After annealing, the wires were manually removed, leaving behind a hollow imprint within the PIPS template. Last, the PS in the PIPS template was selectively removed by dissolving it in cyclohexane.

Characteristic Length Scale Measurements: Sections of the templates were imaged on a scanning electron microscope with the high resolution setting. A fast Fourier transform (FFT) was performed on the image and then rotationally averaged. A peak in the power spectrum is obtained, which corresponds to the characteristic length scale of the quasi-periodic structure. The characteristic length scale L_c is measured between the origin and the peak g_0 in reciprocal space, with $L_c = 1/g_0$.

Characterization: Characterization of membrane topologies were performed using SEM . SEM images were acquired using a Philips XL-30 FEG SEM. Image processing was performed using the ImageJ image processing and analysis software.

4.3.3 Discussion

The PIPS process allows for more precise control over the features and structures of a microporous structure. In PIPS, poly(lactic) acid is initially dissolved in styrene (Figure 4.9). Following dissolution, the styrene is polymerized into polystyrene which induces the phase separation between the two polymers. The initial dissolution of PLA allows for the two phases to be well dispersed and co-continuous in the following the phase separation. Finally, the structures are annealed in order to control the characteristic size scale of the

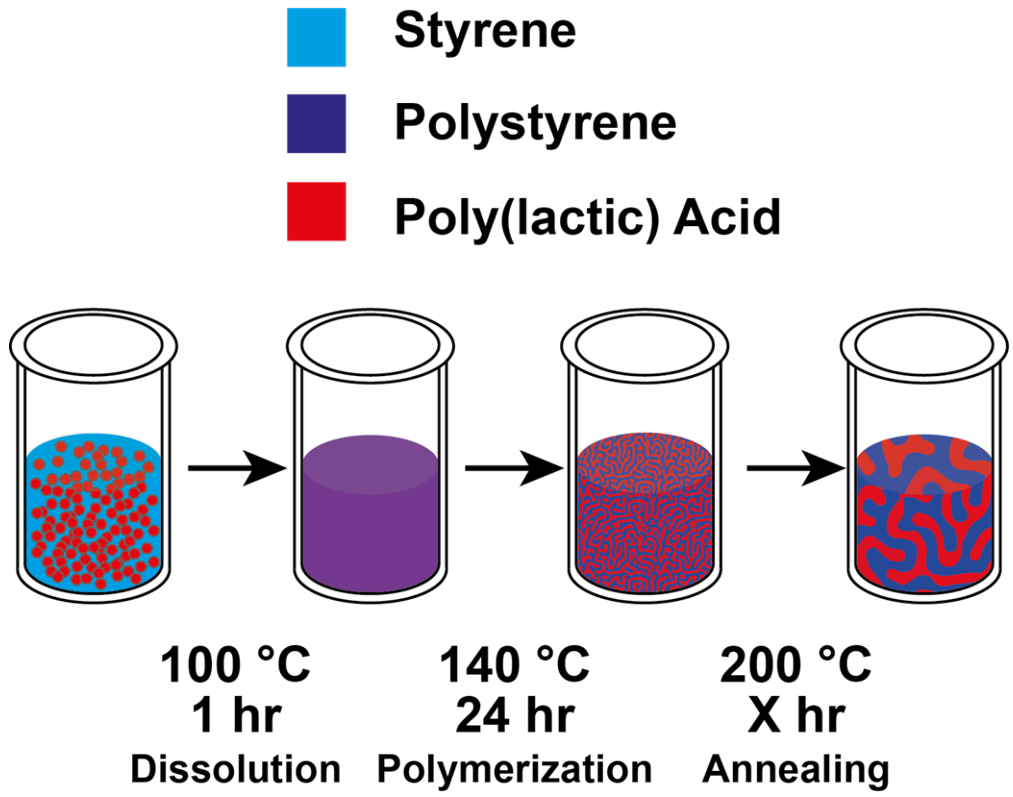

Figure 4.9: Polymerization Induced Phase Separation. First, poly(lactic) acid is dissolved in styrene. Next, the styrene is polymerized into polystyrene to induce phase separation. Last, the mixture is annealed at high temperatures to control characteristic lengths.

three-dimensional structures.

We examined the characteristic size features of the PIPS microstructures with respect to annealing time (Figure 4.10). We found that as we increased the annealing time, the characteristic length increased in a nonlinear manner. The characteristic lengths ranged from 4 μm to 10 μm for annealing times ranging from 0 to 120 minutes. At the annealing temperature, the two phases are mobile and are able coarsen in this melt state. Using the coarsening feature of PIPS, we could fabricate microstructures with varying degrees of specific surface areas.

We also examined the characteristic size features with respect to the polymer blend composition (Figure 4.11). We found that as the PLA content increased, there was no increase in the characteristic lengths of the PLA phase. However, the aggregate characteristic lengths

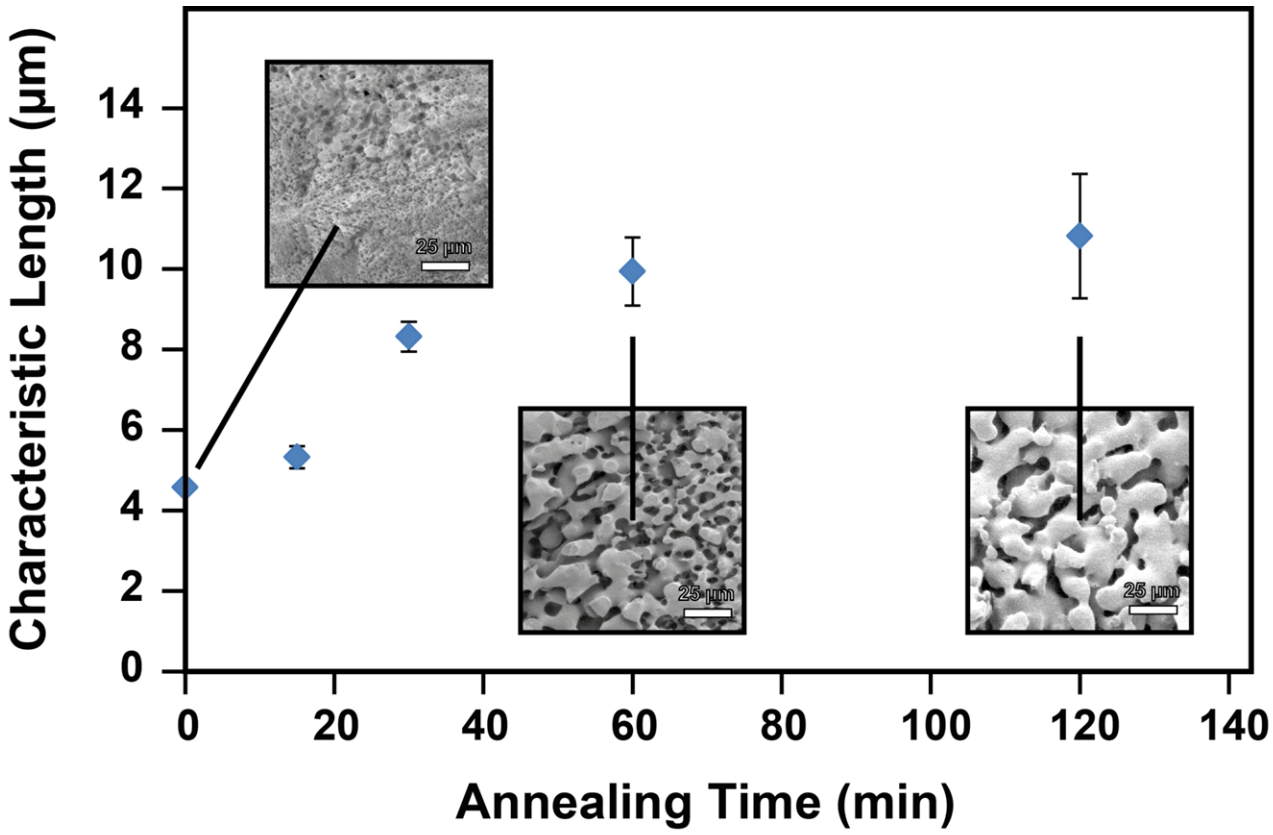

Figure 4.10: PIPS Annealing Time. SEM images were taken of PIPS structures at various annealing times. As the annealing time increased, so did the characteristic lengths.

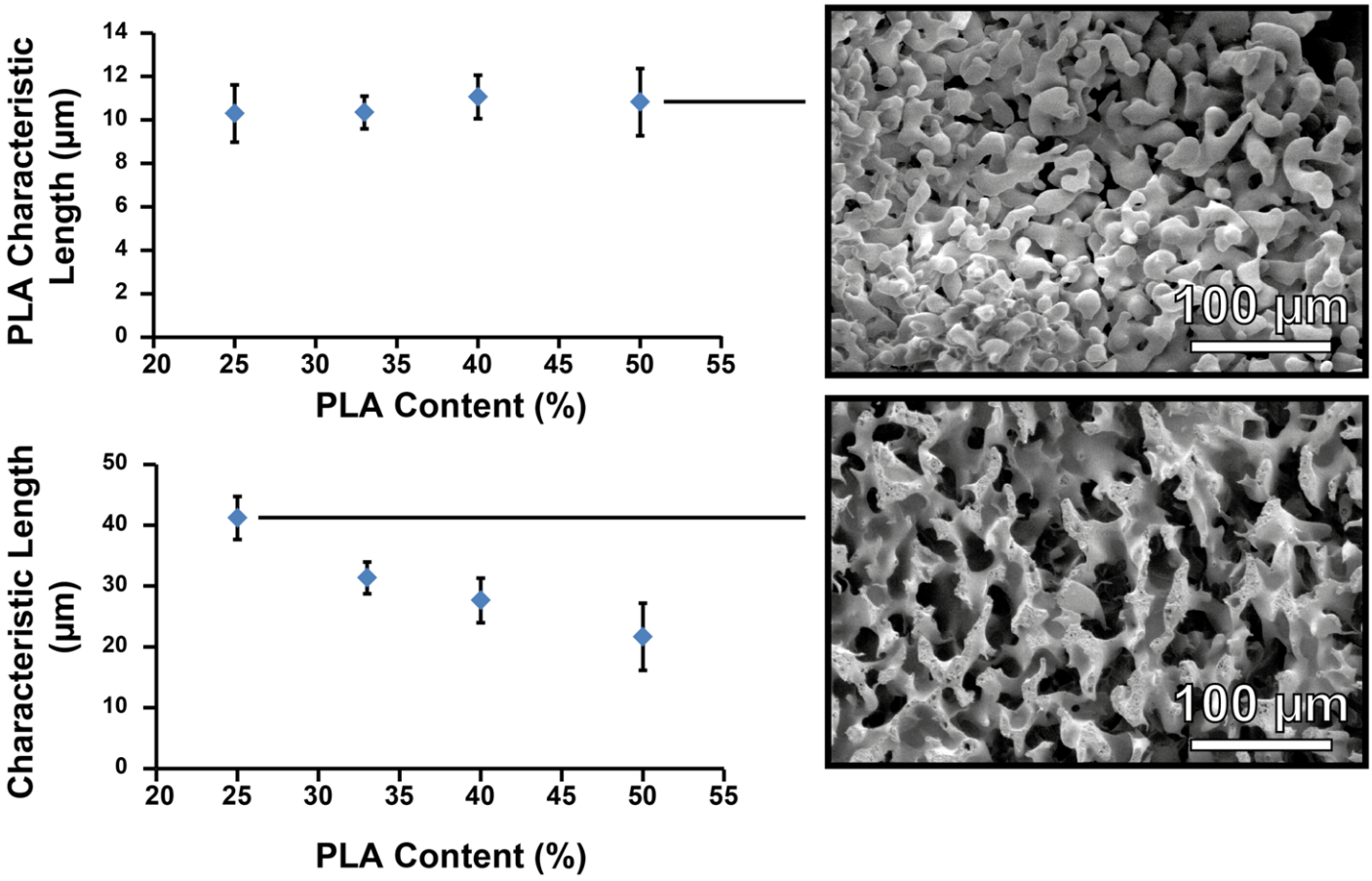

Figure 4.11: PIPS Mixture Composition. The characteristic lengths of the PIPS structures were examined with respect to the PLA/PS mixture composition. The characteristic lengths of the PLA phase did not change with respect to composition. Instead, only the characteristic length of the PS phase was affected.

increased as PLA content decreased. This indicated that with different solution compositions, only the characteristic length of the PS phase changed. Using the combination of annealing time and polymer blend composition would allow use to control both the sizes of the PLA phase and the PS phase independently.

We combined the PIPS microstructures with secondary sacrificial elements to form a hierarchical stricture (Figure 4.12). Stainless steel wires were used as a secondary template that the PIPS structure was fabricated around. When the wires were removed, they left behind a hollow imprint within the PIPS structure which acted as the initial tier of the hierarchy.

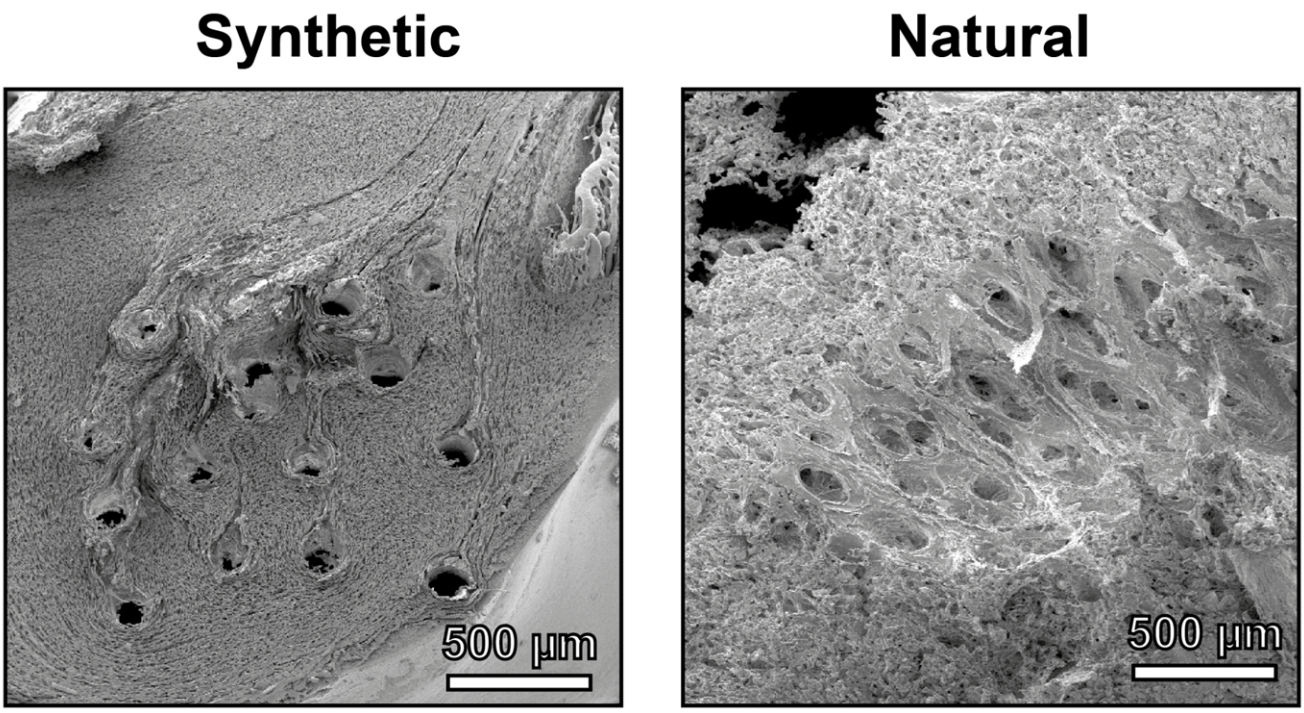

Figure 4.12: Hierarchical PIPS Microstructure. Using stainless steel wires, a secondary hierarchy was added to the structure. The structure was qualitatively compared to a natural avian parabronchus, indicating a good match.

Last, we combined the PIPS process with the conformal membrane coatings. A PLA content of 33 wt. % was used with an annealing time of 2 hours to form the PIPS microstructure. The coating process was then applied twice to the structure. Last, the PLA was selectively removed using a a 1M NaOH solution in a 50/50 wt/wt mixture of water and methanol. The result was a hollow microstructure matched to the initial PIPS template (Figure 4.13).

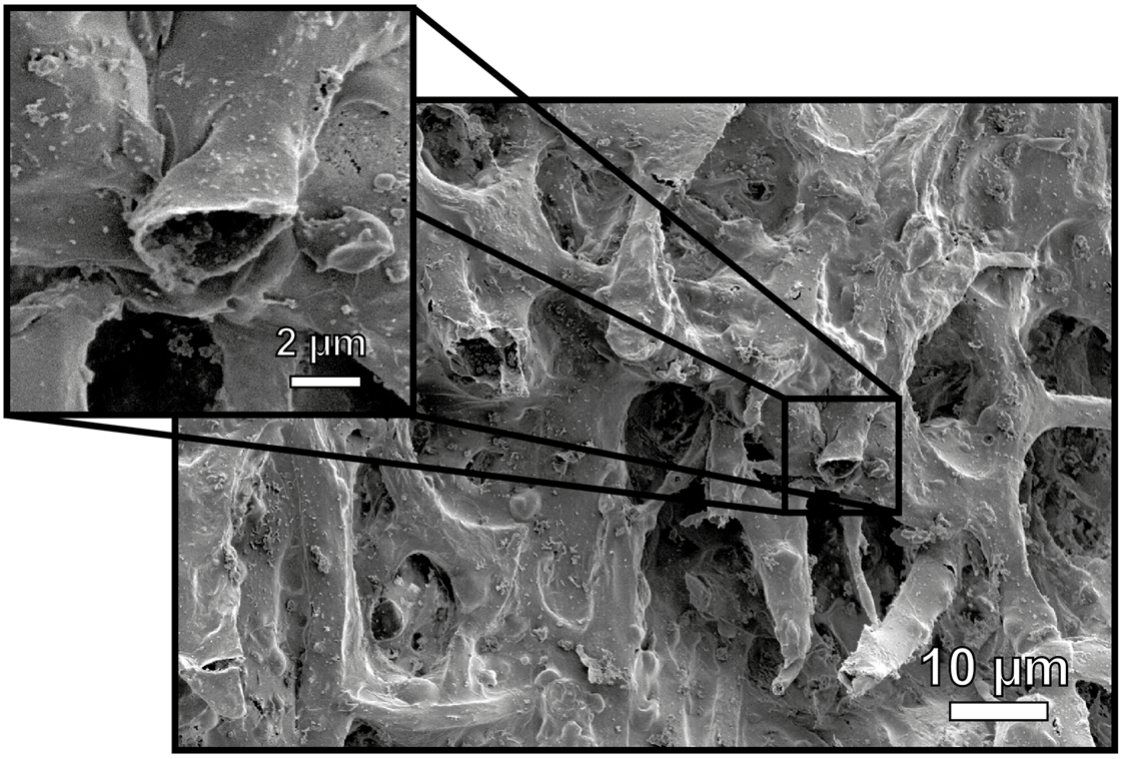

Figure 4.13: Hollow PIPS Membrane Microstructure. The combination of PIPS and conformal membrane coatings was used to create a hollow membrane microstructure.

Bibliography

[1] A. Talo, P. Passiniemi, O. Forsn, and S. Ylsaari. Polyaniline/epoxy coatings with good anti-corrosion properties. *Synthetic Metals*, 85(1-3):1333–1334, March 1997.

[2] Abdel Salam Hamdy. Advanced nano-particles anti-corrosion ceria based sol gel coatings for aluminum alloys. *Materials Letters*, 60(21-22):2633–2637, September 2006.

[3] Frederik C. Krebs. Fabrication and processing of polymer solar cells: A review of printing and coating techniques. *Solar Energy Materials and Solar Cells*, 93(4):394–412, April 2009.

[4] Liangbing Hu, Han Sun Kim, Jung-Yong Lee, Peter Peumans, and Yi Cui. Scalable Coating and Properties of Transparent, Flexible, Silver Nanowire Electrodes. *ACS Nano*, 4(5):2955–2963, May 2010.

[5] Sung Woo Oh, Seung-Taek Myung, Seung-Min Oh, Kyu Hwan Oh, Khalil Amine, Bruno Scrosati, and Yang-Kook Sun. Double Carbon Coating of $LiFePO_4$ as High Rate Electrode for Rechargeable Lithium Batteries. *Advanced Materials*, 22(43):4842–4845, November 2010.

[6] Gozde Ozaydin-Ince, Anna Maria Coclite, and Karen K Gleason. CVD of polymeric thin films: applications in sensors, biotechnology, microelectronics/organic electronics, microfluidics, MEMS, composites and membranes. *Reports on Progress in Physics*, 75 (1):016501, January 2012.

[7] Mikko Ritala and Jaakko Niinist. Chapter 4. Atomic Layer Deposition. In Anthony C Jones and Michael L Hitchman, editors, *Chemical Vapour Deposition*, pages 158–206. Royal Society of Chemistry, Cambridge, 2009.

[8] Wei Chen and Thomas J. McCarthy. Layer-by-Layer Deposition: A Tool for Polymer Surface Modification. *Macromolecules*, 30(1):78–86, January 1997.

[9] M. Knez, K. Nielsch, and L. Niinist. Synthesis and Surface Engineering of Complex Nanostructures by Atomic Layer Deposition. *Advanced Materials*, 19(21):3425–3438, November 2007.

[10] C.J. Brinker, G.C. Frye, A.J. Hurd, and C.S. Ashley. Fundamentals of sol-gel dip coating. *Thin Solid Films*, 201(1):97–108, June 1991.

[11] Ryan P. Lively, Joshua A. Mysona, Ronald R. Chance, and William J. Koros. Formation of Defect-Free Latex Films on Porous Fiber Supports. *ACS Applied Materials & Interfaces*, 3(9):3568–3582, September 2011.

[12] L. E. Stillwagon and R. G. Larson. Leveling of thin films over uneven substrates during spin coating. *Physics of Fluids A: Fluid Dynamics*, 2(11):1937, 1990.

[13] L. E. Scriven. Physics and Applications of DIP Coating and Spin Coating. *MRS Proceedings*, 121, February 2011.

[14] H Yanagishita, D Kitamoto, K Haraya, T Nakane, T Okada, H Matsuda, Y Idemoto, and N Koura. Separation performance of polyimide composite membrane prepared by dip coating process. *Journal of Membrane Science*, 188(2):165–172, July 2001.

[15] David B. Hall, Patrick Underhill, and John M. Torkelson. Spin coating of thin and ultrathin polymer films. *Polymer Engineering & Science*, 38(12):2039–2045, December 1998.

[16] C. J. Lawrence. The mechanics of spin coating of polymer films. *Physics of Fluids*, 31 (10):2786, 1988.

[17] A.B. Frazier and M.G. Allen. Metallic microstructures fabricated using photosensitive polyimide electroplating molds. *Journal of Microelectromechanical Systems*, 2(2):87–94, June 1993.

[18] Ryan P. Lively, Ronald R. Chance, B. T. Kelley, Harry W. Deckman, Jeffery H. Drese, Christopher W. Jones, and William J. Koros. Hollow Fiber Adsorbents for CO_2 Removal from Flue Gas. *Industrial & Engineering Chemistry Research*, 48(15):7314–7324, August 2009.

[19] Dominic T Clausi and William J Koros. Formation of defect-free polyimide hollow fiber membranes for gas separations. *Journal of Membrane Science*, 167(1):79–89, March 2000.

[20] A Corti. Carbon dioxide removal in power generation using membrane technology. *Energy*, 29(12-15):2025–2043, December 2004.

[21] Clem E. Powell and Greg G. Qiao. Polymeric CO_2/N_2 gas separation membranes for the capture of carbon dioxide from power plant flue gases. *Journal of Membrane Science*, 279(1-2):1–49, August 2006.

[22] Hefei Dong, Aaron P. Esser-Kahn, Piyush R. Thakre, Jason F. Patrick, Nancy R. Sottos, Scott R. White, and Jeffrey S. Moore. Chemical Treatment of Poly(lactic acid) Fibers to Enhance the Rate of Thermal Depolymerization. *ACS Applied Materials & Interfaces*, 4(2):503–509, February 2012.

[23] Rahul M. Rasal, Amol V. Janorkar, and Douglas E. Hirt. Poly(lactic acid) modifications. *Progress in Polymer Science*, 35(3):338–356, March 2010.

[24] Robin A. Quirk, Martyn C. Davies, Saul J. B. Tendler, and Kevin M. Shakesheff. Surface Engineering of Poly(lactic acid) by Entrapment of Modifying Species. *Macromolecules*, 33(2):258–260, January 2000.

[25] Du T. Nguyen, Y T. Leho, and Aaron P. Esser-Kahn. A three-dimensional microvascular gas exchange unit for carbon dioxide capture. *Lab Chip*, 12(7):1246–1250, March 2012.

[26] Du T. Nguyen, Y T. Leho, and Aaron P. Esser-Kahn. The Effect of Membrane Thickness on a Microvascular Gas Exchange Unit. *Advanced Functional Materials*, 23(1):100–106, January 2013.

[27] Aaron P. Esser-Kahn, Piyush R. Thakre, Hefei Dong, Jason F. Patrick, Vitalii K. Vlasko-Vlasov, Nancy R. Sottos, Jeffrey S. Moore, and Scott R. White. Three-Dimensional Microvascular Fiber-Reinforced Composites. *Advanced Materials*, 23(32): 3654–3658, August 2011.

[28] T Tanaka and D Lloyd. Formation of poly(l-lactic acid) microfiltration membranes via thermally induced phase separation. *Journal of Membrane Science*, 238(1-2):65–73, July 2004.

[29] Yoon Sung Nam and Tae Gwan Park. Biodegradable polymeric microcellular foams by modified thermally induced phase separation method. *Biomaterials*, 20(19):1783–1790, October 1999.

[30] Peter Budd, Elabas Elssalhen, Bader Ghanem, Saad Makhseed, Neil McKeown, Kadhum Msayib, Carin Tattershall, and Dong Wang. Solution-Processed, Organophilic Membrane Derived from a Polymer of Intrinsic Microporosity (Synthesis of PIM-1). *Advanced Materials*, 16:456–459, March 2004.

[31] S. Takayama, E. Ostuni, X. Qian, J. C McDonald, X. Jiang, P. LeDuc, M. H Wu, D. E Ingber, and G. M Whitesides. Topographical Micropatterning of Poly(dimethylsiloxane) Using Laminar Flows of Liquids in Capillaries. *Advanced Materials*, 13(8):570–574, April 2001.

[32] Leon M. Bellan, Tatiana Kniazeva, Ernest S. Kim, Alla A. Epshteyn, Donald M. Cropek, Robert Langer, and Jeffrey T. Borenstein. Fabrication of a Hybrid Microfluidic System Incorporating both Lithographically Patterned Microchannels and a 3D FiberFormed Microfluidic Network. *Advanced Healthcare Materials*, 1(2):164–167, January 2012.

[33] Ying Zheng, Peter W. Henderson, Nak Won Choi, Lawrence J. Bonassar, Jason A. Spector, and Abraham D. Stroock. Microstructured templates for directed growth and vascularization of soft tissue in vivo. *Biomaterials*, 32(23):5391–5401, August 2011.

[34] Aijuan Zhang, Mingjie Chen, Can Du, Huizhang Guo, Hua Bai, and Lei Li. Poly(dimethylsiloxane) Oil Absorbent with a Three-Dimensionally Interconnected Porous Structure and Swellable Skeleton. *ACS Applied Materials & Interfaces*, 5(20): 10201–10206, October 2013.

[35] Kathleen S. Toohey, Nancy R. Sottos, Jennifer A. Lewis, Jeffrey S. Moore, and Scott R. White. Self-healing materials with microvascular networks. *Nature Materials*, 6(8): 581–585, June 2007.

[36] C. J. Bettinger, E. J. Weinberg, K. M. Kulig, J. P. Vacanti, Y. Wang, J. T. Borenstein, and R. Langer. Three-Dimensional Microfluidic Tissue-Engineering Scaffolds Using a Flexible Biodegradable Polymer. *Advanced Materials*, 18(2):165–169, January 2006.

[37] Aditya Balasubramanian, Robert Morhard, and Christopher J Bettinger. Shape-Memory Microfluidics. *Advanced Functional Materials*, 23(38):4832–4839, 2013.

Chapter 5

Waste Heat Usage

5.1 Introduction

Our work in creating biomimetic microvascular structures allowed us to created efficient devices for the efficient absorption of CO_2 into a CO_2 absorbing solution. This aims to decrease the footprint of a carbon capture setup for the retrofitting of existing power plants. However, the issue of energy cost must also be addressed for practical implementation. For a conventional capture solvent, such as monoethanolamine (MEA), the largest energy cost comes from the regeneration of the solvent for cyclic use.

Here we demonstrate a system that uses low grade waste-heat from surfaces to provide energy for chemical reactions. To access the waste-heat, we fabricated a microvascular stripping system composed of microchannels, up to meters in length, conformed to heated ceramic and metal surfaces in complex three-dimensional configurations. Our initial system released CO_2 from a saturated MEA solution. MEA is a capture reagent currently used in pilot-scale plants, but is often cited as too energetically expensive for large-scale use.[4] In our microvascular system, we found that increased CO_2 release resulted from; (1) decreasing

the diameter of the microchannel, (2) increasing the surface temperature, and (3) increasing the solution residence time. Using high-speed photography, we observed a two-phase flow phenomenon in the form of bubbly, slug, and annular flow.[10, 11] We report a stripping rate of 1.9 mg/min for MEA in a 300 μm diameter microchannel conformed onto a surface heated to 125 °C.

The micron-scale features in large, distributed systems are essential for accessing heat transfer characteristics of two-phase release.[12–18] Methods of microvascular fabrication, such as the Vaporization of a Sacrificial Component (VaSC), lithographic techniques, direct-write approaches, and many others, can form these micron-sized features.[19–27] At the micron-scale, differences from the macro-scale arise as surface tension counteracts gravitational effects and laminar rather than turbulent flows are dominant.[28] The mechanisms of two-phase heat transfer and its relationship to gas nucleation is not yet fully understood, as the methods of characterizing these systems can vary widely.[29] However, we observed rapid and complete CO_2 release occurring only with channels below 300 μm in diameter, indicating the advantages of using micro-scale heat exchangers.

5.2 Experimental

We fabricated our microvascular waste-heat system using the VaSC process.[30] VaSC is a sacrificial polymer process to create long, cylindrical microchannels and vasculature conformed directly to a surface. The non-lithographic nature of VaSC is particularly suited for the formation of microvasculature directly on surfaces with complex 3D contours that allow direct access to waste-heat. Most other micro-vascular fabrication processes require initially flat substrates restricting their direct access many surfaces. Others such as 3D printing can be well suited for fabricating solid structures, but are less capable of forming hollow structures. In contrast to other heat exchanger fabrication techniques, the length, ease, and

conformability of VaSC allow this technique to adapt microchannels to pre-fabricated surfaces. However, VaSC has limitations in that it does not obtain the same structural precision as lithographic techniques. The fabrication process is also limited to materials which set at temperatures below 120 °C and can withstand temperatures above 200 °C.

In a generalized scheme of our experiments, VaSC is used to fabricate cylindrical microchannels on a heated surface. MEA (4.9 M) is saturated with CO_2 (0.5 mol CO_2/mol MEA). CO_2 is captured by MEA as the reaction between MEA and CO_2 forms carbamates via a zwitterionic intermediate. The saturated MEA flows through the microchannels at a controlled flow rate and surface temperature (Figure 5.1). The high temperature reverses the reaction, leading to the release of CO_2. As CO_2 releases from MEA, two phases appear within the microchannel and can be separated for future use or sequestration.

A waste-heat stripping system using this process can be formed around many heated surfaces, including those already present in combustion processes. We demonstrate coupling of VaSC with two-phase release through the microvascular retrofitting of a pre-existing and lab-available waste-heat source: a coffee mug (Figure 5.2a). Using multiple polydimethylsiloxane (PDMS) coatings as the microvascular embedding material, a 1.2 m long, 300 μm diameter microchannel was wrapped around a coffee mug five times and separated from the surface by 40 μm (Figure 5.3).

5.3 Results and Discussion

We released CO_2 from a saturated MEA solution (0.5 mol CO_2/mol MEA) by heating the mug as the solution flowed through the wrapped microchannel. As CO_2 reacts with MEA it lowers the pH of the solution.[31] We visualized the release of CO_2 by adding a pH sensitive dye, phenolphthalein.[32] As CO_2 is recovered, the solution returns to its original pH -

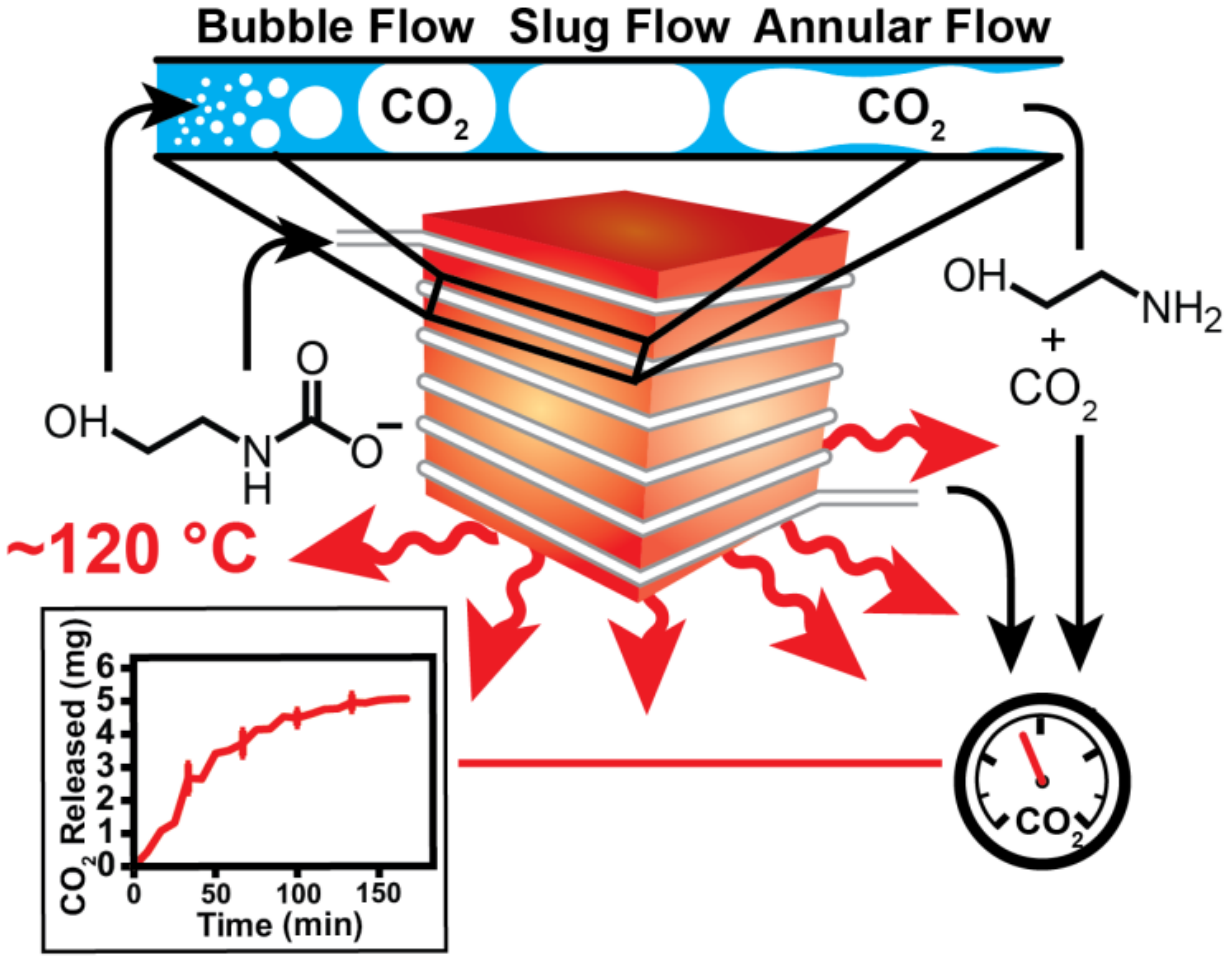

Figure 5.1: CO_2 stripping schematic. Monoethanolamine (MEA) saturated with CO_2 flows through a microvascular channel surrounding a heated surface and embedded within PDMS. The channel is heated to ˜1 20 °C, removing CO_2 from the solution. A two-phase flow profile develops within the microchannel from the released CO_2. The flow rate and concentration of CO_2 exiting the system are measured to calculate the total release of CO_2. A sample data set is provided.

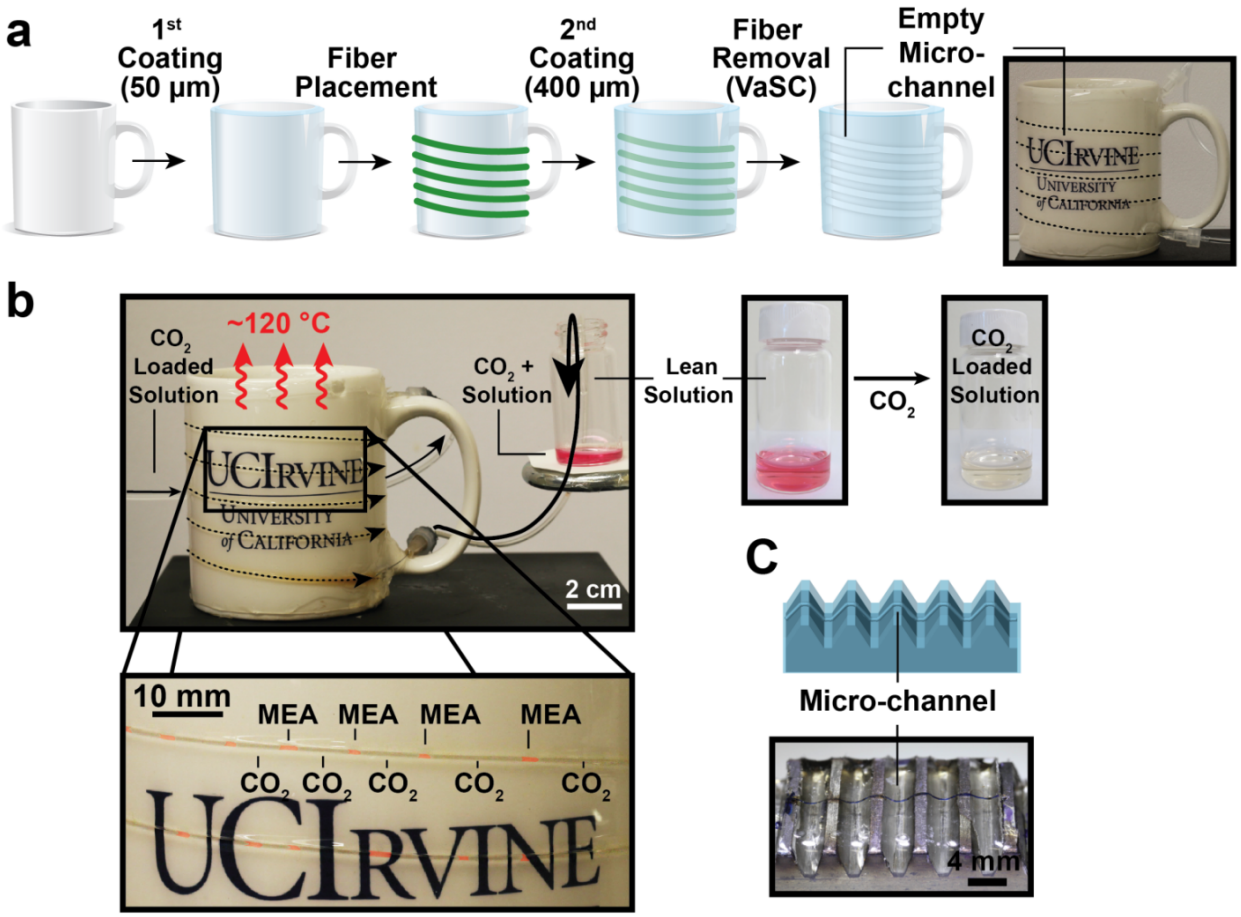

Figure 5.2: CO_2 stripping using waste-heat. (a) Fabrication of microchannels conformed to a coffee mug. First, a layer of PDMS coats the mug. Next, PLA elements are placed to match the contour of the mug. Another layer of PDMS then coats the fibers. Last, the PLA is depolymerized under heat and vacuum. The end result is a single microchannel conformed to the surface of the mug. (b) CO_2 release with the mug. Phenolphthalein dye was added to a CO2 saturated MEA solution, which shifts from clear to pink when CO_2 is released from the solution. The solution flowed through the microchannel at a rate of 0.1 mL/min. The average surface temperature of the mug was 120 °C. After one pass through the microvascular mug, a color shift occurs, indicating the release of CO_2. Scale bar is 2 cm in image and 10 mm in inset. (c) Microchannel on a rough surface. Scale bar, 4 mm.

going from pH ˜8 to ˜12. The dye reflects this change by shifting from clear to pink. To regenerate the solution, the mug was heated until the average surface temperature was 120 °C. After the mug reached thermal equilibrium, the CO_2 saturated solution flowed through the microchannel at a rate of 0.1 mL/min. Within one cycle, the color of the solution shifted from clear to pink, indicating the release of CO_2 (Figure 5.2b). The lean MEA solution was then re-saturated with CO_2 to quantify the amount of CO_2 released. This was calculated to be 0.10 mol CO_2/mol MEA (0.14 mol CO_2/mol MEA is released in conventional systems)[33], corresponding to a release rate of 1.9 mg CO_2/min.

Other stripping systems, such as packed columns and membrane contactors achieve higher fluxes of CO_2. However, when the release rates of these systems are scaled relative to the flow rates in our system, similar values are found (˜1-3 mg/min at 0.1 mL/min MEA flow rate).[34][7] However, our system stands in contrast as it can use waste heat energy due to its conformability to 3D contours. While the stripping mug demonstrated a practical surface for microstructure fabrication, not all heated surfaces are smooth and round. We verified the adaptability of the VaSC process by fabricating microchannels on a rough surface, a gear rack (Figure 5.2c). The fabrication process was similar to that of the mug, using multiple PDMS coating layers (Figure 5.4). Using VaSC, many surfaces could provide energy for chemical reactions through waste-heat recovery.

We then studied parameters affecting the release efficiency including channel diameter, surface temperature, and residence time. A smaller system (4.4 cm) was developed to quantify the release of CO_2 ((Figure 5.5)). The exhaust gas flow rate and CO_2 concentration were used to calculate the total release of CO_2, using an infrared CO_2 meter and mass flow-meter (Figure 5.6). Using thermocouples, we measured fluid input, fluid output, and surface temperatures to calculate the heat transfer coefficients (Table 5.1). Additional values such as Nusselt numbers and power input were also calculated (Appendix A.2).

First, we investigated the effect of channel diameter on the amount of CO_2 released from

Length Scale (μm)	Flow Rate (mL min^{-1})	T (°C)	Total CO2 Release (mg)	Initial Release Rate (mg min^{-1})	h (W m^{-2} K^{-1})
Hex.	0.05	125	29.8 ± 2.6	1.00 ± 0.17	70 ± 10
Hex.	0.1	125	19.0 ± 3.6	1.11 ± 0.28	80 ± 20
Hex.	0.2	125	12.7 ± 0.9	1.68 ± 0.65	170 ± 50
100	0.1	125	9.1 ± 1.7	0.69 ± 0.14	910 ± 140
200	0.1	125	4.9 ± 0.3	0.46 ± 0.02	570 ± 90
300	0.05	125	9.0 ± 1.1	0.55 ± 0.05	320 ± 50
300	0.1	125	5.1 ± 0.2	0.43 ± 0.02	430 ± 80
300	0.2	125	1.4 ± 0.1	0.23 ± 0.03	870 ± 170
1590	0.05	125	9.2 ± 1.2	0.53 ± 0.04	41 ± 4
1590	0.1	125	2.8 ± 0.4	0.24 ± 0.02	23 ± 3
1590	0.2	125	1.6 ± 0.6	0.24 ± 0.14	21 ± 7
300	0.1	105	0.8 ± 0.4	0.06 ± 0.04	73 ± 19
300	0.1	115	2.5 ± 0.4	0.24 ± 0.08	310 ± 40
300	0.1	125	5.1 ± 0.2	0.43 ± 0.02	430 ± 80
300	0.1	135	8.7 ± 0.9	0.84 ± 0.19	560 ± 140

Table 5.1: CO_2 release under experimental conditions. After multiple cycles, no further CO_2 releases from the solution and the total CO_2 release is recorded. The first several cycles give the largest release rates. These initial release rates most closely mimic a continous operation environment Heat transfer coefficents were calculated from fluid input, fluid output, and surface temperatures, coupled with CO_2 release rates. Surface area for the Hexagonal pattern uses all seven 200 μm diameter channels and the length scale is considered to be 200 μm

MEA using 100-300 μm diameter microchannels. We also examined a larger channel with a 1.59 mm diameter, as an example of a traditional size scale, and a hexagonally packed pattern of 200 μm diameter channels. For each experiment, the surface temperature was 125 °C and the solution flowed at a rate of 0.1 mL/min. Computational models of the temperature profiles within the channels were also developed (Figure 5.8). As the channel diameters decreased, we saw an increase in the total amount of CO_2 released. The 100 μm diameter microchannel obtained the highest heat transfer coefficient (910 W/m^{2}K). However, the dense, hexagonally packed arrangement of microchannels released the most CO_2 by more than a factor of two. Using packed patterns of micro-channels provides more efficient release of CO_2 than millimeter size channels. The result of the packed hexagonal structure also demonstrated that the release of CO_2 can be achieved while reducing the system footprint.

Next, we investigated the effect of surface temperature on the flow stripping process using a 300 μm diameter microchannel and a flow rate of 0.1 mL/min. We found that increasing the surface temperature also increased the total release of CO_2, with an increase from 125 °C to 135 °C nearly doubling the amount released. CO_2 is released from MEA at 100-120 °C in industrial processes, matching the release temperature of CO_2 detected in our system.[35] The ability to release CO_2 on surfaces with temperatures from 100 °C and higher may have practical applications since heat pipes can reach temperatures in excess of 120 °C.[36]

The last effect we investigated was the solution residence time using our two most diverse cases for comparison: the hexagonally patterned 200 μm and 1.59 mm diameter channels. The residence time was investigated via the MEA flow rate. In both cases, decreasing the MEA flow rate in the channel resulted in greater CO_2 release. The hexagonal pattern at a flow rate of 0.05 mL/min obtained the highest release rate of any parameter set (1.7 mg/min). While the slower flow rate allows for increased CO_2 release, it also limits the throughput of the microvascular system. For a full system, a balance must be achieved between throughput and CO_2 release efficiency.

Interestingly, little correlation between heat transfer coefficients and either total CO_2 release or initial release rate was found. Instead, the gas release correlated more strongly with power entering the system (Appendix A.5). This may be due to the chemical reaction taking place or the complex geometry of the system. An alternative calculation of the release rates was conducted through the visual analysis of the flow-stripping phenomenon using high-speed photography and a serpentine microchannel (Figure 5.10)[37, 38]. The release of CO_2 from MEA was observed predominantly as the slug flow profile under these conditions. When a slug flow pattern develops, the velocities of the gas phase allow for measurement of the pressure of the gas. Combining this with the volume of the gas phase, the ideal gas law is used to calculate the release rate of CO_2 within the microvascular system. Using this visual analysis, the CO_2 release rate was calculated to be 0.8 ± 0.2 mg/min (100 μm micro-channel, 125 °C, 0.1 mL/min), agreeing with the previously measured release rate.

We wanted to determine, for potential applications, what our current stripping rates would translate to on a larger scale. To give a sense of what might be possible, we performed a calculation of how much heated area would be required to recover the CO_2 captured from an automobile. Assuming a square packed arrangement of microchannels and a release rate of 0.8 mg/min per channel, 0.0565 m^2 of surface area would be required to recover the amount of CO_2 emitted from an automobile. The total system dimensions required corresponds approximately to the size of a laboratory notebook. In contrast to other heat exchangers, this exchanger volume could also be conformed directly to a heated area rather than located in a separate region. However, this volume only accounts for the heat exchanger dimensions and does consider other necessary system components that increase the size.

5.4 Fabrication

5.4.1 Stripping Mug Fabrication

To form the stripping mug, the Vaporization of a Sacrificial Component (VaSC) fabrication technique was employed.[25] Poly(lactic) acid (PLA) fibers (Teijin Monofilament, Germany) were treated with tin (II) oxalate (98%, Sigma-Aldrich, USA) in order to lower the depolymerization temperature of the fiber.[39] Polydimethylsiloxane (PDMS, Sylgard 184 Silicone Elastomer, Dow Corning, USA) was prepared by mixing the base with the curing agent (10:1, wt:wt). A layer of PDMS was then poured over the surface of a coffee mug and left on aluminum foil. After 5 minutes, the mug and foil were flipped upside down as the PDMS on the mug cured at 85 °C for 30 minutes. This flipping method allowed for a more even coating of PDMS on the surface. A 300 μm PLA fiber was wrapped around the mug five times, with both ends tied to the handle of the mug. Each wrap was spaced 11 mm from the previous wrap. A second coating was poured on the mug using same method. One last coating was performed with the mug starting upside down to create a uniform layer of PDMS over the fiber. The mug was heated at 212 °C under vacuum for 3 days to remove the PLA, leaving behind a hollow microchannel (Figure 5.3).

5.4.2 Rough Surface Microchannel Fabrication

A 9 cm long steel gear rack (20 pitch, 1/2" face width, and 1/2" height, McMaster-Carr) was used as the rough surface. To form microchannels conforming to the rough surface, a layer of PDMS was poured over the surface of the gear rack and cured at 85 °C for 30 minutes (Figure 5.4). After curing, a 200 μm PLA fiber was placed over the surface. A second coating was then poured over the surface and fiber. Another gear rack was used as a complementary surface to press the fiber into the teeth of the gear rack so that it would

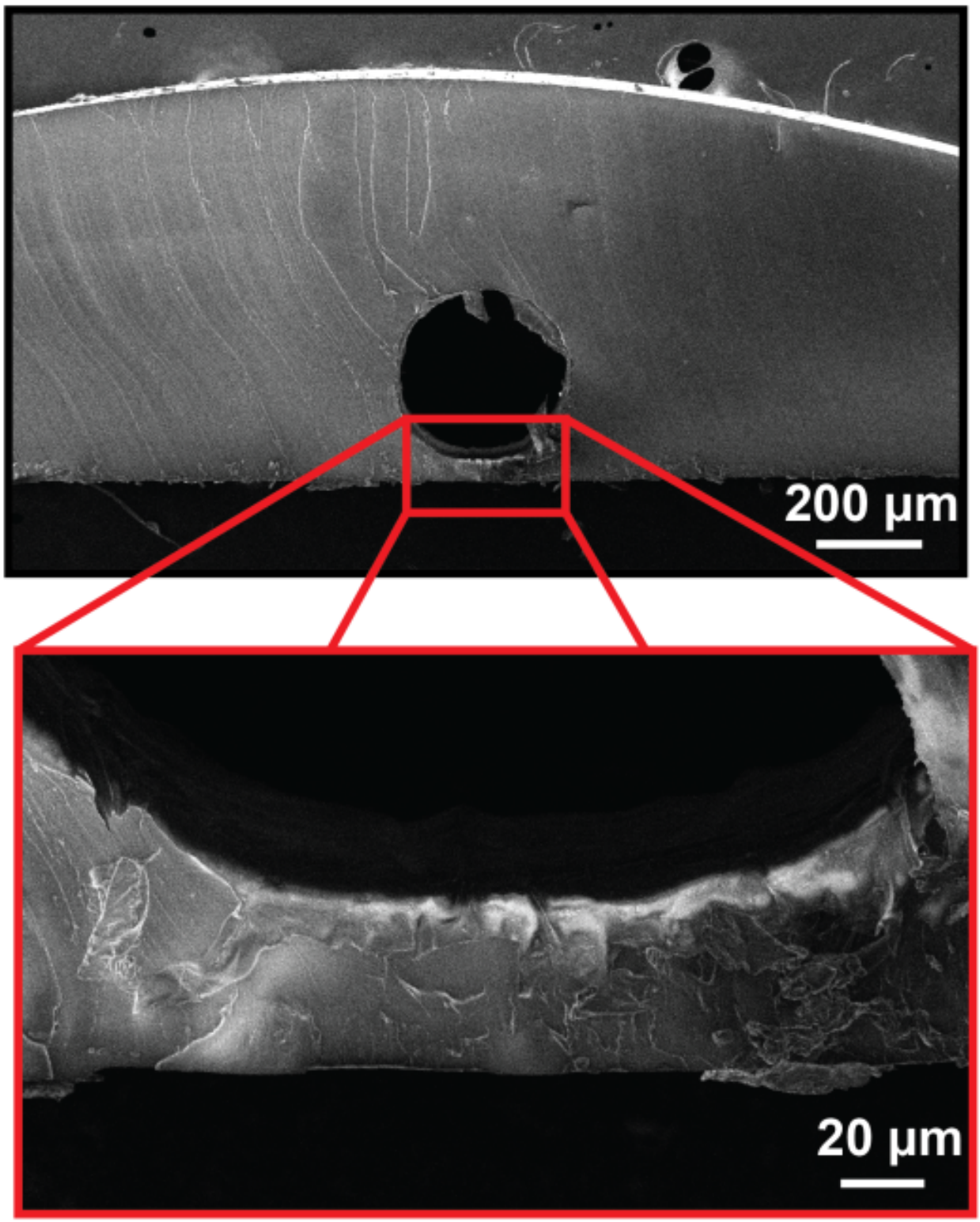

Figure 5.3: Stripping mug cross-section. The first layer of PDMS applied to the stripping mug creates a 40 μm thick coating before the fiber is conformed to the surface. The additional layers create a 400 μm thick coating above the fibers.

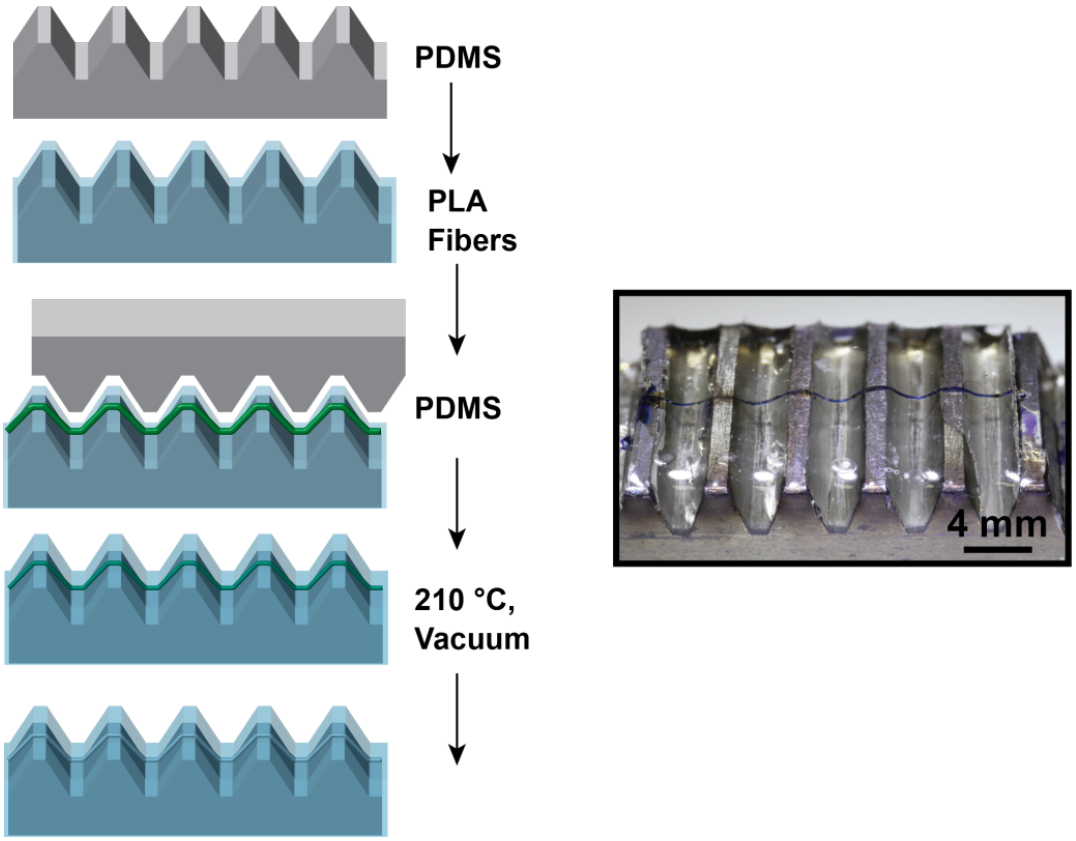

Figure 5.4: Rough surface microchannel. PDMS first coats a gear rack serving as the rough surface. A PLA fiber is placed on the surface and another gear rack is used to conform the fiber to the top of the first PDMS layer. Another layer of PDMS is cured over the fiber. Last, the fibers are depolymerized under heat and vacuum, leaving behind an empty microchannel conformed to the surface of the gear rack. Water dyed with methyl blue was loaded into the microchannel for visual clarity.

conform to the surface. The PDMS was left to cure overnight at room temperature. The second gear rack was removed and a final coating was performed to create a uniform layer of PDMS over the fiber. The gear rack was heated to 212 °C under vacuum for 3 days to evacuate the PLA.

5.4.3 Stripping Unit Fabrication

PLA fibers with the desired diameters were placed in a rectangular 3 in. long mold box. PDMS was prepared and then poured into the mold box until a height of 5 mm was reached.

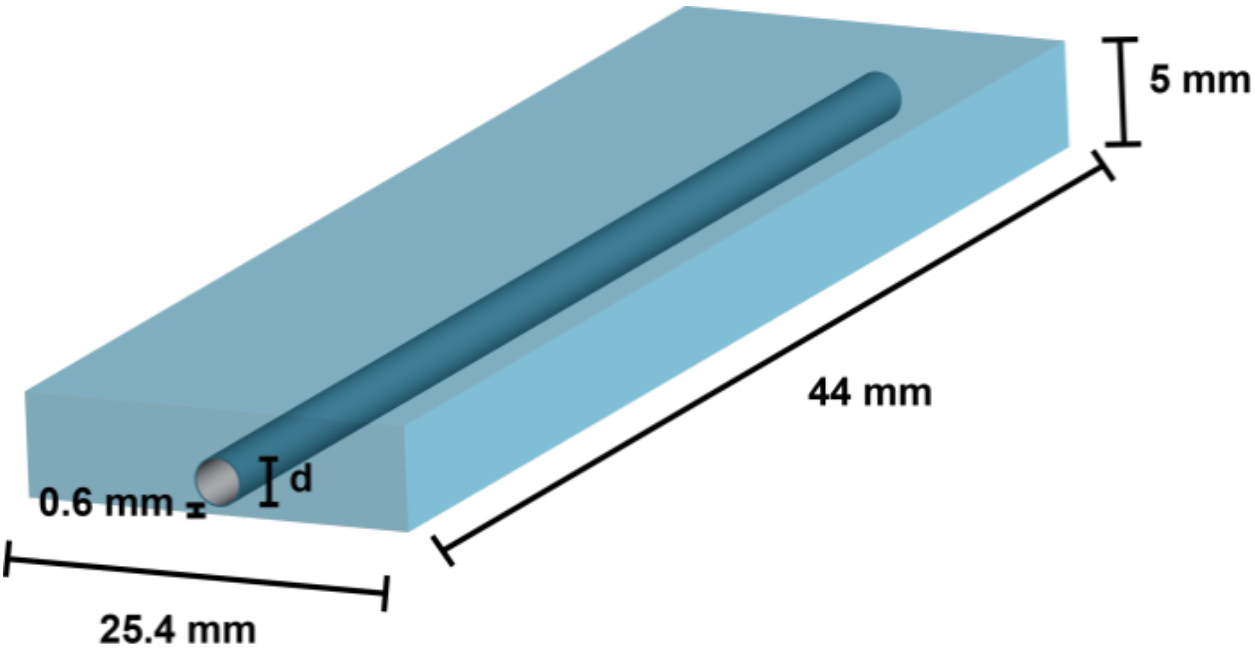

Figure 5.5: Stripping unit dimensions. The dimensions of the stripping unit were largely controlled by the size of the mold box. The distance between the bottom of the unit to the channel edge was determined by the thickness of a second PDMS coating. The channel diameter d varied depending on the experiment.

The box was then placed in an oven at 85 °C for 30 min to cure the PDMS. The unit was removed from the mold box and a layer of PDMS was cured on the bottom of the sample to obtain a uniform thickness of 0.6 mm for each sample from the channel edge to the heated surface. This second layer ensured that the distance from the heated surface to the bottom edge of the channels was consistent for each unit. The PLA fiber was evacuated from the PDMS by heating the sample to 212 °C under vacuum for 24 hours resulting in a hollow channel of the desired diameter. Last, each stripping unit was then cut to a length of 4.4 cm (Figure 5.5).

To fabricate the hexagonal pattern, a similar process was followed, but using a laser-cut brass patterning plate containing a hexagonal pattern.[25] The PLA fibers were strung through a pair of plates and the plates were placed onto both ends of the mold box. The fibers were tensioned to obtain a parallel set of fibers in a hexagonal pattern. The same procedures for creating a single microchannel were then followed.

A polyether ether ketone (PEEK) tube was used to form the larger 1.59 mm diameter channel instead of a PLA fiber. Similar steps as the other fabrication procedures were then followed until the evacuation step. Instead of heating the sample under vacuum, the tube was manually removed out from the PDMS, leaving a hollow channel.

5.4.4 Serpentine Microchannel Fabrication

A process similar to the VaSC technique was followed to fabricate the serpentine microchannel. Six PLA fibers with 100 μm diameters were strung through a laser cut plate with six horizontal holes separated by 100 μm. The plates and fibers were then placed in a 2" long mold box. PDMS was poured into the mold box until the fibers were fully covered. The box was placed in an oven at 85 °C for 30 minutes to cure the PDMS. The sample was removed from the mold box and the fibers were manually pulled from the PDMS, resulting in six parallel channels. The sample was cut into a length of 2.8 mm. A single PLA fiber was threaded through the six parallel channels resulting in a single serpentine pattern. A second layer of PDMS was poured to encompass the sample and a second curing step was performed. The PLA was removed from the PDMS by heating the sample up to 212 °C under vacuum for 24 hours, resulting in a serpentine microchannel.

5.5 CO_2 Release Measurement

To obtain monoethanolamine (MEA, Sigma-Aldrich, USA) saturated with CO_2, a 100 mL solution of 30% vol. monoethanolamine in DI water was first mixed. 30 mg of phenolphthalein (Sigma-Aldrich, USA) dye was then added to the solution. 7 mL of the MEA solution was withdrawn and placed within a scintillation vial. 100% CO_2 was flowed through the solution for 90 minutes at a rate of 20 mL/min. Further time was spent flowing CO_2 through

the solution until 10 wt% of CO_2 in the solution was reached, as measured by an analytical balance. Additional aliquots of CO_2 saturated MEA were made as necessary.

A 1 mL syringe was loaded with the CO_2 saturated MEA solution. The syringe was placed onto a syringe pump (NE-1000, New Era Pump Systems Inc.), and connected to a stripping unit. For phase separation, one end of a 1/16 in. tubing (Ultra-Chemical-Resistant Clear Tygon PVC Tubing, McMaster-Carr, USA) was glued to a 1mL syringe. The other end of the tubing was connected to a mass flow meter (Cole-Palmer Low-Cost Gas Mass Flowmeter, 0-20 sccm). The flow meter was directly connected to an infrared CO_2 meter (COZIR Wide-Range 100% CO_2 Meter, CO_2Meter, Inc.) to detect the concentration of CO_2 exiting the microchannel. An aluminum block (3.0 $\times$ 4.0 $\times$ 0.75 in., McMaster-Carr) was placed on a hot plate to moderate and control the temperature of the stripping unit (Figure 5.6). The unit was placed between the aluminum block and a 38 g PDMS weight. The weight was placed on top of the sample to ensure close contact with the heating plate and to reduce convective cooling effects on the top surface of the sample. The system was heated for 2 minutes to thermal equilibrium.

Each pumping cycle consisted of a pumping, first pause, withdrawal, and second pause phase. The pumping phase pumped the CO_2 saturated solution through the channel at the desired flow rate until 1 mL of solution was flowed through. The system then paused for 3 minutes and the sample was raised from the heating plate to cool down. This prevented unmeasured CO_2 release during the withdrawal phase. The CO_2 meter was flushed with N_2 until the CO_2 meter read a CO_2 concentration of less than 0.5%. The pump withdrew the MEA solution at a rate of 0.2 mL/min for 2 minutes. The stripping unit was placed onto the heating plate and left on for a second pause phase lasting 2 minutes. The pumping cycle was repeated for 3 hours for each experiment. After each trial, the flow meter and CO_2 meter were flushed with N_2 for 10 minutes. A new phase separating syringe was prepared for each experiment.

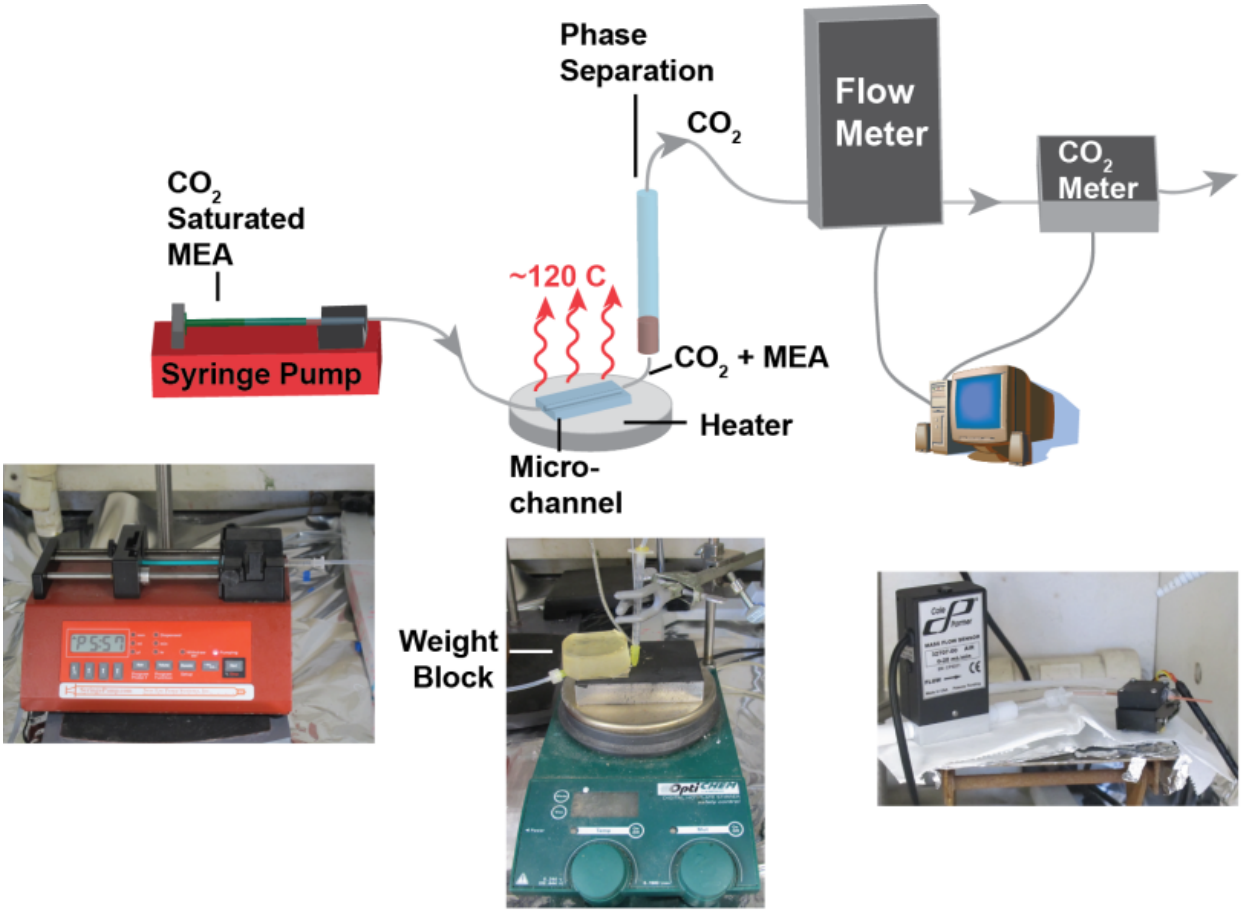

Figure 5.6: CO_2 release measurement setup. A syringe pump is used to continuously pump and pull CO_2 saturated MEA through a microchannel. The microchannel is heated with an aluminum block on a hot plate. As CO_2 is released from the microchannel, the liquid and gas phases are separated by gravity in a syringe. The continuous flow of MEA forces the gas through a flow meter and then a CO_2 meter which are used to calculate release of CO_2.

5.6 CO_2 Release Calculation

The total release of CO_2 from the channels was calculated using a combination of the flow rate and concentration of CO_2 measurements (Figure 5.7). First, the flow rate was converted from a voltage output to a mass flow rate, compensating for the effect of CO_2 concentration on the mass flow meter output.

fv = Flow Rate (V)

c = Concentration (% CO_2)

f = Flow Rate (mL/sec)

$$f = fv(V) \times 4\left(\frac{mL}{minV}\right) \times \left(\frac{min}{sec}\right) \times \left(1 - \left(\frac{c(\%CO_2)}{100}\right) \times 0.261\right)$$

The flow rate multiplied by the concentration was then integrated to obtain the total amount of CO_2 flowed through the system.

T = Total CO_2 Release (mg)

t_f = final integration time (s)

t_{dsat} = Desaturation time (s)

$$T = 1.98\left(\frac{mgCO_2}{mLCO_2}\right) \times \int_0^{t_f}\left(\frac{mL}{sec}\right) \times \frac{c(\%CO_2)}{100}dt$$

To plot the total release over time, the range of integration was varied from 0 to t_{dsat}.

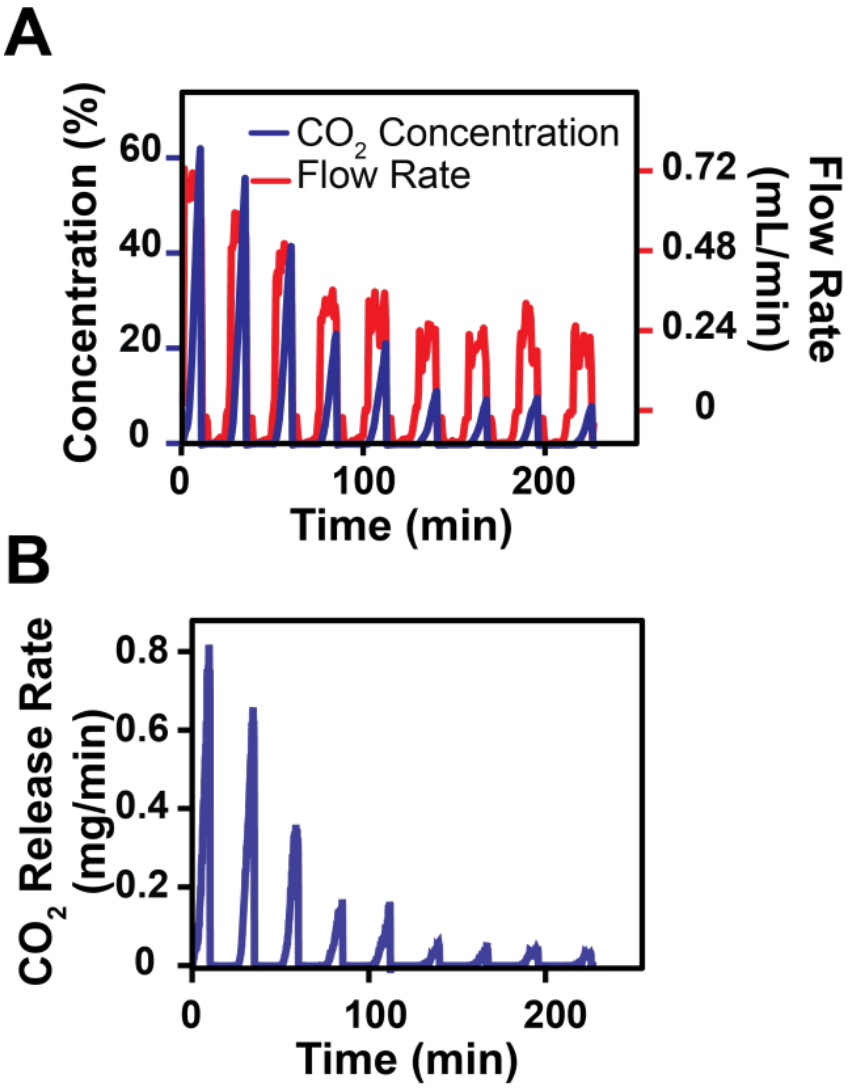

Figure 5.7: Sample CO_2 release data and calculation. (A) Raw data output. MEA flowed through a 100 μm diameter microchannel at a flow rate of 0.1 mL/min and a surface temperature of 125 °C. The mass flow-meter and IR CO_2 meter measure the flow rate and concentration of CO_2 simultaneously. Several peaks/plateaus appear due to the cyclic pumping of the CO_2 saturated MEA solution. (B) Calculated CO_2 release rates. Release rates are found by combining the CO_2 concentration and flow rate. Integrating the release rate with respect to time results in the total amount of CO_2 released.

5.7 COMSOL Model Channel Heat Gradient

For each channel diameter and pattern, the COMSOL finite element modeling program was used to estimate the heat gradient in the vertical direction (Figure 5.8). The model was performed assuming convective cooling on the side edges of the stripping unit, but not the top edge due to the presence of the PDMS block. A surface temperature of 125 °C and a flow rate of 0.1 mL/min were used. Only single phase flow was used to estimate the temperature gradient as the exact two-phase flow heat transfer mechanisms are still under investigation. The model parameters were set for both CO_2 and water to serve as the upper and lower bound estimates of the temperature gradient (Figure 5.9a,b). From the model, we found that as the channel diameter increased, so did the temperature gradient in the vertical direction. Additionally, we observed that the temperature gradient was larger at the ends of the unit. Within the central portion of the unit, the largest temperature difference between the top and bottom of the channel was found to be only ˜1 °C for the gas phase. For the liquid phase, the temperature difference is higher at ˜8 °C due to the higher heat capacity of water. The largest temperature differences occurred in the hexagonally packed 200 μm diameter microchannels and the 1.59 mm diameter channel. A large temperature gradient was observed at the edges of the channel due to the sample boundaries. The average temperature across the entire channel was also calculated (Figure 5.9c). In the gas phase, the average temperatures were uniform. In the liquid phase, the average temperature decreased as the channel diameter decreased, suggesting the importance of the two-phase heat transfer enhancement on the micron scale. While the model is only an approximation to the experiment, it suggests that the vertical temperature gradient due to the change in channel size is not the only contributor to the enhanced release of CO_2

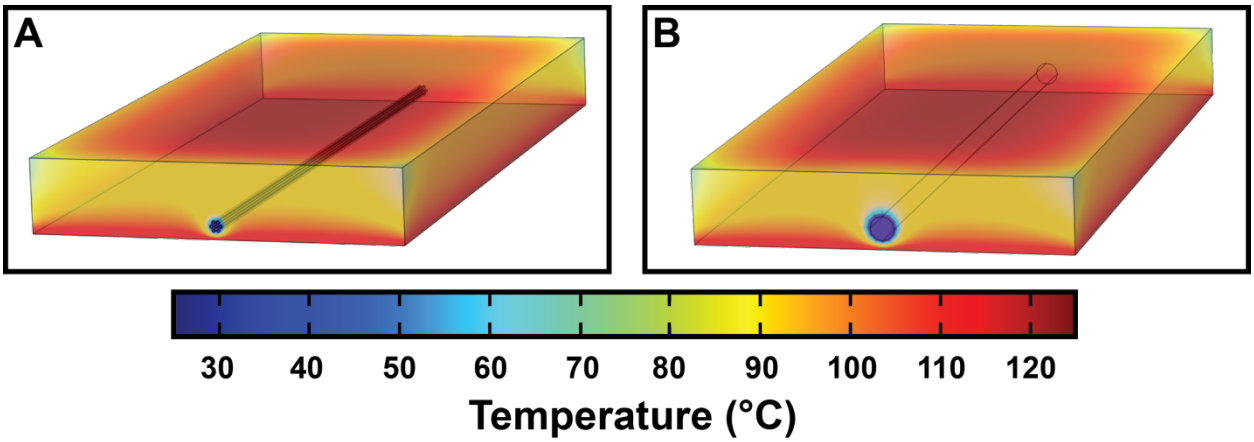

Figure 5.8: COMSOL Heat Transfer Model. The temperatures in the channels are estimated using a single phase flow of either liquid or gas. The dimensions and flow conditions are set to match the experimental conditions. (A) Hexagonal microchannel arrangement model. (B) 1.59 mm channel diameter model.

5.8 High Speed Optical Analysis

A Vision Research Phantom v7.3 high-speed camera was used to image the flow-stripping process. MEA dyed with methyl blue (0.3 mg dye/mL solution) was saturated with CO_2 to reach 10 CO_2 wt%. The camera was mounted on a vertical camera rail with a 1-5X lens. A serpentine microchannel was mounted on a glass slide to stabilize its position and then placed on a hot plate. The hot plate temperature was adjusted until the serpentine microchannel temperature reached 125 °C. The MEA loaded with CO_2 was flowed through the microchannel at the desired flow rate. The camera captured 4938 frames during an exposure time of 30 μs and frame rate of 150 μs/frame. Images were processed in ImageJ.

The change in pressure was calculated using the friction factor and pressure gradient. The calculation was based on a model of slug flow in microchannels with diameters less than 1 mm.[37, 38, 43, 44] Using the high speed videos of the release of CO_2, the sum of the gas and liquid velocities for a gas bubble/liquid slug pair was measured (5.10). The change in volume of the gas bubble was also measured.

ρ = Liquid density (kg/m^3)

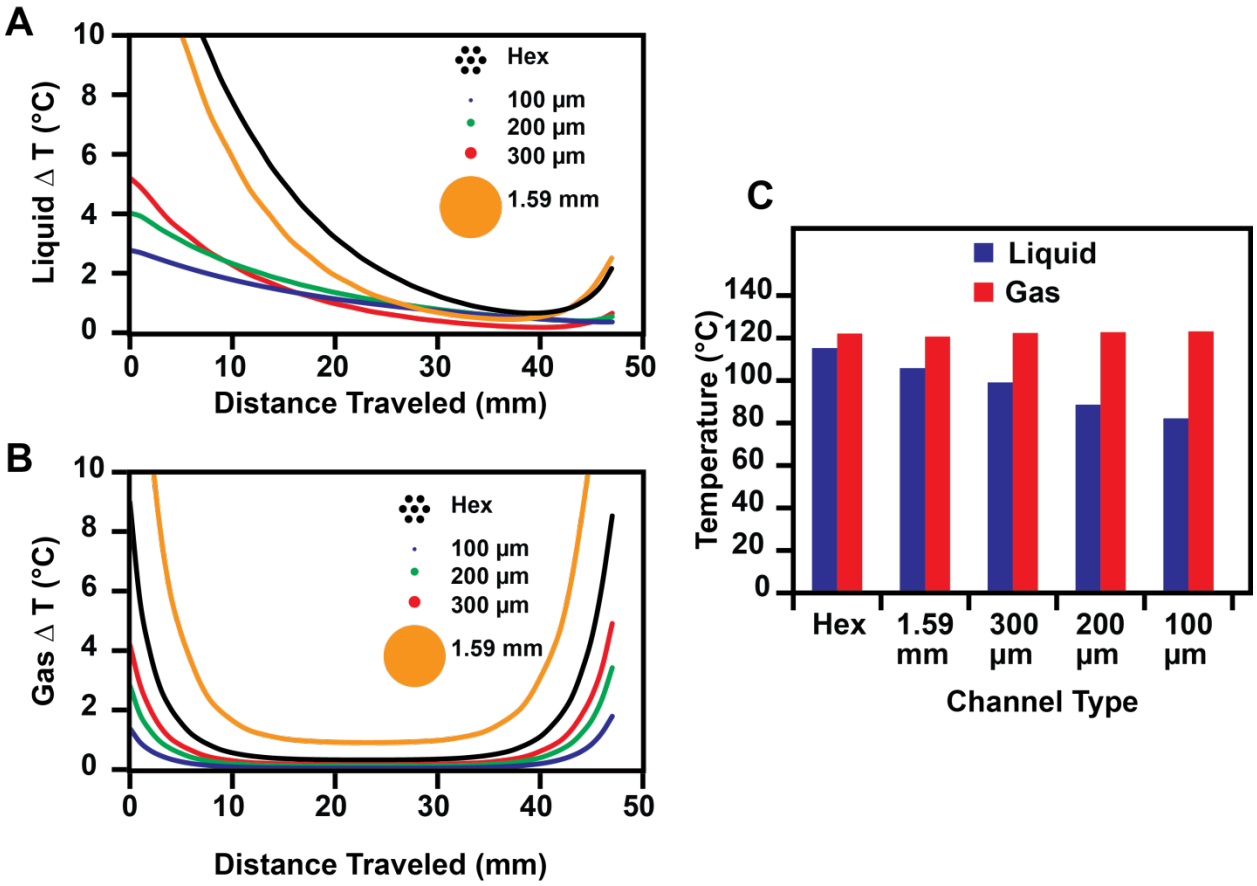

Figure 5.9: COMSOL model results. (A) Liquid vertical change in temperature. As the fluid travels through the channel length, the temperature gradient decreases for all channel diameters. The high heat capacity of water results in a longer path length to reach a gradient minimum. (B) Gas vertical change in temperature. In the gas phase, the temperature gradient is more uniform due to the lower heat capacity. At the edges of the channels, a larger gradient occurs due to exposure to an outside environment. (C) Average temperatures. In the liquid phase, the average channel temperature decreases as the channel diameter decreases. In the gas phase, the average temperature is uniform with respect to channel diameters and patterns.

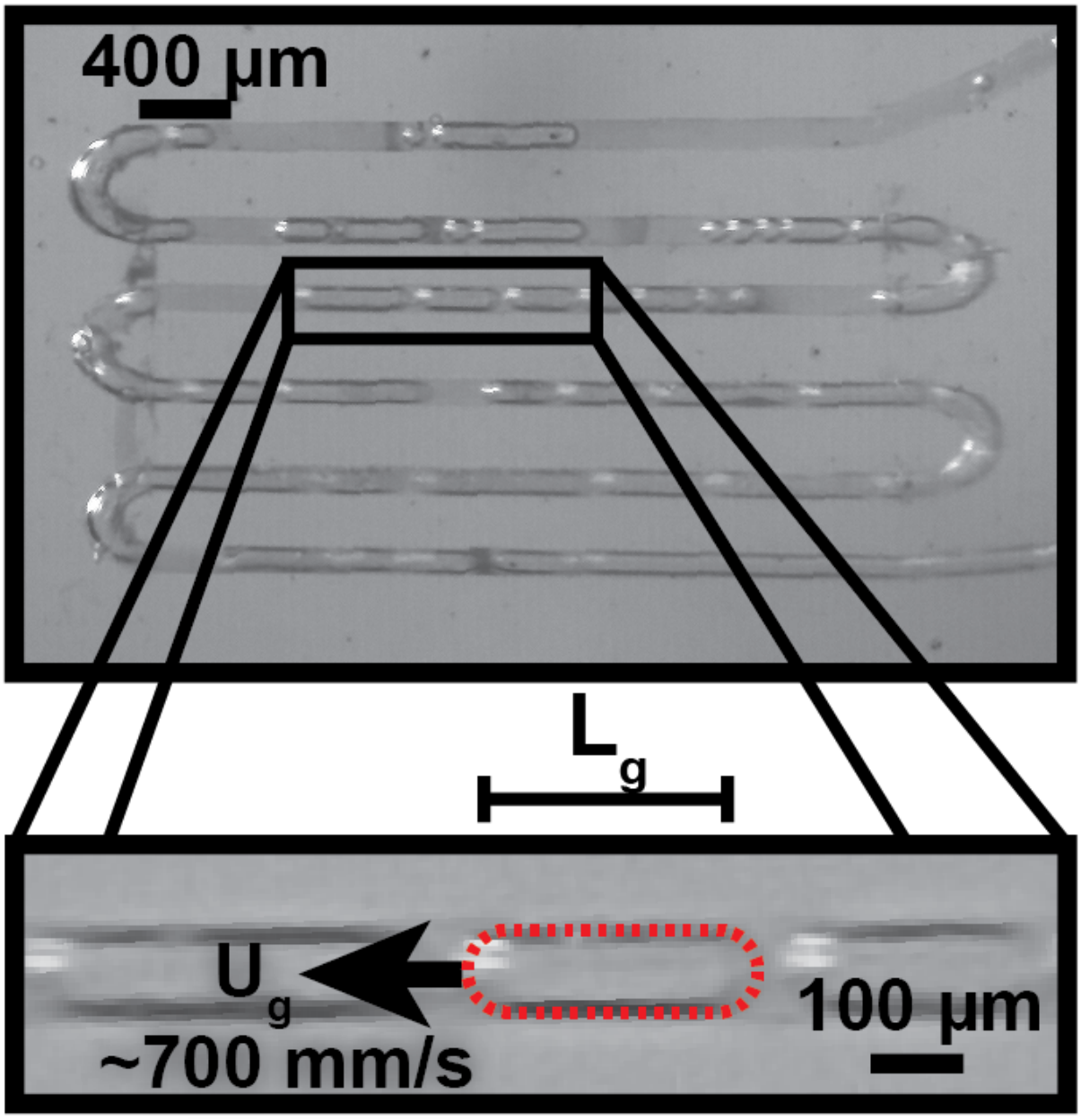

Figure 5.10: CO_2 stripping from MEA in a serpentine, 100 μm diameter microchannel. The two-phase profile was observed predominantly in the form of either slug flow or annular flow. By measuring the volume and velocities of the CO_2 gas plugs, the release rate of CO_2 can be calculated using high-speed photography. Image resolution decreases as the release of CO_2 increases flow velocity. Scale bar is 400 μm in image and 100 μm in inset.

D = Channel diameter (m)

U_{gl} = Sum of the gas and liquid velocities

μ = Viscosity of the liquid (Pa*s)

σ = Surface tension (N/m)

Q_l = Volumetric flow rate (m^3/s)

L_s = Liquid slug length (m)

Re = Reynolds number based on the liquid properties and sum of the gas and liquid velocities

Ca = Capillary number based on the liquid properties and the sum of the gas and liquid velocities

A = Channel cross-section area (m^2)

U_l = Liquid velocity (m/s)

Ca_b = Capillary number based on the liquid properties gas velocity

D_b = Gas bubble diameter (m)

A_b = Gas bubble cross-sectional area (m^2)

δ = Correction on the liquid slug length for the amount of liquid in the slug surrounding the nose and tail of a gas bubble (m)

a = Fit parameter

f_s = Slug friction factor

P = Pressure (Pa)

$Re = \frac{\rho D U_{gl}}{\mu}$

$Ca = \frac{\mu U_{gl}}{\sigma}$

$A = \pi \left(\frac{D}{2}\right)^2$

$U_l = \frac{Q_l}{A}$

$Ca_b = \frac{\mu(U_{gl} - U_l)}{\sigma}$

$D_b = D\left(1 - \frac{0.67 Ca_b^{2/3}}{1 + 3.34 Ca_b^{2/3}}\right)$

$A_b = \pi \left(\frac{D_b}{2}\right)^2$

$\delta = \frac{D_b}{3}$

$a = \frac{7.16 \times 3^{2/3}}{32} \frac{A}{A_b} \left(\frac{Ca}{Re}\right)^{1/3} \left(Ca_b^{1/3} + 3.34 Ca_b\right)^{-1}$

$f_s = \frac{16}{Re}\left(1 + a \frac{D}{L_s + \delta} \left(\frac{Re}{Ca}\right)^{0.33}\right)$

$\frac{dP}{dx} = -\frac{2\mu U_l}{D^2} f_s Re$

To estimate the pressure drop, values of $\sigma = 0.0401$ (N/m), $\mu = 6.03 \times 10^{-4}$ (Pa s), $=$ 1010 (kg/m3), $D = 100 \times 10^{-6}$ (m), $Q_l = 1.67 \times 10^{-9} (m^3)$, and $L_s = 150 \times 10^{-6}$ (m) were used.[45, 46] The inlet pressure was measured as 75895 Pa by a differential pressure transducer (PC mountable wet/wet differential pressure sensor, Cole-Palmer). The ideal gas law was used to calculate the overall CO_2 release rate using the pressure temperature, and gas volume. Initial and final time points were measured for individual bubbles.

dt = Change in time between initial and final time points (s)

x = Distance travelled by gas bubble from inlet (m)

n = Average number of gas bubbles in the microchannel

P = Absolute pressure in gas bubble (Pa)

V = Gas bubble volume (m^3)

R = Gas constant (J/mol K)

T = Temperature (K)

$P = P_0 - x \times \frac{dP}{dx}$

$rate = \frac{P_f V_f - P_i V_i}{RT}(molCO_2) \times \frac{1}{dt} \times 44.01 \left(\frac{gCO_2}{molCO_2}\right) \times \left(\frac{mg}{g}\right) \times \left(\frac{sec}{min}\right) \times n$

The average number of gas bubbles in the microchannel was estimated to be 20. The results of the calculations are summarized in Table S1. The average release rate for the 100 μm diameter microchannel was 0.76 $\pm$ 0.2 mg/min.

5.9 Surface Area Use Estimation

To estimate necessary surface area to strip the CO_2 output of an automobile, several assumptions were used. A car is estimated to release an average of 241 g CO_2/km,[47] and was assumed to travel at 100 km/hr. A CO_2 stripping rate of 0.8 mg/min was used for a 100 μm diameter microchannel with a 5 cm length and 1 cm layer thickness. First, the total number of units necessary was calculated.

ACO_2 = Automotive CO_2 release rate (g/km)

Av = Automotive velocity (km/hr)

S = Stripping rate (mg/min)

U = number of units necessary

$$U = 1000\left(\frac{mg}{g}\right) \times ACO_2\left(\frac{g}{km}\right) \times Av\left(\frac{km}{hr}\right) \times \frac{1}{60}\left(\frac{hr}{min}\right) \times \frac{1}{0.8}\left(\frac{min}{mg}\right)$$

The number of units required was multiplied by the surface area of the channels, assuming a square packed arrangement of the channels, separated by 50 μm

Cd = Channel diameter (m)

Cl = Channel length (m)

T = Structure thickness (m)

Sa = Surface Area necessary (m^2)

$$Sa = \frac{U \times (Cd + 50 \times 10^{-6})(m) \times Cl(m)}{T(m)/(Cd + 50 \times 10^{-6})(m)}$$

Bibliography

[1] P. Friedlingstein, R. A. Houghton, G. Marland, J. Hackler, T. A. Boden, T. J. Conway, J. G. Canadell, M. R. Raupach, P. Ciais, and C. Le Qur. Update on CO_2 emissions. *Nature Geoscience*, 3(12):811–812, November 2010.

[2] Howard J. Herzog. Peer Reviewed: What Future for Carbon Capture and Sequestration? *Environmental Science & Technology*, 35(7):148A–153A, April 2001.

[3] Timothy J. Skone. Carbon Dioxide Capture from Existing Coal-Fired Power Plants. Technical Report DOE/NETL-401/110907, U.S. Department of Energy, November 2007.

[4] J. P. Ciferno, T. E. Fout, A. P. Jones, and J. T. Murphy. Capturing Carbon from Existing Coal-Fired Power Plants | AIChE. *Chemical Engineering Progress*, 105:33–41, April 2009.

[5] Mohammad R.M. Abu-Zahra, Lon H.J. Schneiders, John P.M. Niederer, Paul H.M. Feron, and Geert F. Versteeg. CO_2 capture from power plants. *International Journal of Greenhouse Gas Control*, 1(1):37–46, April 2007.

[6] Owen J. Curnow, Susan P. Krumdieck, and Elizabeth M. Jenkins. Regeneration of Carbon Dioxide Saturated MonoethanolamineGlycol Aqueous Solutions at Atmospheric Pressure in a Packed Bubble Reactor. *Industrial & Engineering Chemistry Research*, 44(4):1085–1089, February 2005.

[7] Sakarin Khaisri, David deMontigny, Paitoon Tontiwachwuthikul, and Ratana Jiraratananon. CO_2 stripping from monoethanolamine using a membrane contactor. *Journal of Membrane Science*, 376(12):110–118, July 2011.

[8] S. Moazzem, M.G. Rasul, and M.M.K. Khan. A Review on Technologies for Reducing

CO_2 Emission from Coal Fired Power Plants. In Mohammad Rasul, editor, *Thermal Power Plants*. InTech, January 2012.

[9] Ryan P. Lively, Ronald R. Chance, and William J. Koros. Enabling Low-Cost CO_2 Capture via Heat Integration. *Industrial & Engineering Chemistry Research*, 49(16): 7550–7562, August 2010.

[10] K.A. Triplett, S.M. Ghiaasiaan, S.I. Abdel-Khalik, and D.L. Sadowski. Gasliquid two-phase flow in microchannels Part I: two-phase flow patterns. *International Journal of Multiphase Flow*, 25(3):377–394, April 1999.

[11] John W. Coleman and Srinivas Garimella. Characterization of two-phase flow patterns in small diameter round and rectangular tubes. *International Journal of Heat and Mass Transfer*, 42(15):2869–2881, August 1999.

[12] Weilin Qu and Issam Mudawar. Flow boiling heat transfer in two-phase micro-channel heat sinksI. Experimental investigation and assessment of correlation methods. *International Journal of Heat and Mass Transfer*, 46(15):2755–2771, July 2003.

[13] Dong Liu and Suresh V. Garimella. Flow Boiling Heat Transfer in Microchannels. *Journal of Heat Transfer*, 129(10):1321–1331, 2007.

[14] V. Dupont and J. R. Thome. Evaporation in microchannels: influence of the channel diameter on heat transfer. *Microfluidics and Nanofluidics*, 1(2):119–127, December 2004.

[15] C.L. Ong and J.R. Thome. Macro-to-microchannel transition in two-phase flow: Part 2 Flow boiling heat transfer and critical heat flux. *Experimental Thermal and Fluid Science*, 35(6):873–886, September 2011.

[16] Stefan S. Bertsch, Eckhard A. Groll, and Suresh V. Garimella. Review and Compara-

tive Analysis of Studies on Saturated Flow Boiling in Small Channels. *Nanoscale and Microscale Thermophysical Engineering*, 12(3):187–227, September 2008.

[17] S. Garimella, J. D. Killion, and J. W. Coleman. An Experimentally Validated Model for Two-Phase Pressure Drop in the Intermittent Flow Regime for Circular Microchannels. *Journal of Fluids Engineering*, 124(1):205–214, 2002.

[18] Tannaz Harirchian and Suresh V. Garimella. Flow regime-based modeling of heat transfer and pressure drop in microchannel flow boiling. *International Journal of Heat and Mass Transfer*, 55(4):1246–1260, January 2012.

[19] Leon M. Bellan, Matthew Pearsall, Donald M. Cropek, and Robert Langer. A 3D Interconnected Microchannel Network Formed in Gelatin by Sacrificial Shellac Microfibers. *Advanced Materials*, 24(38):5187–5191, October 2012.

[20] C. J. Bettinger, E. J. Weinberg, K. M. Kulig, J. P. Vacanti, Y. Wang, J. T. Borenstein, and R. Langer. Three-Dimensional Microfluidic Tissue-Engineering Scaffolds Using a Flexible Biodegradable Polymer. *Advanced Materials*, 18(2):165–169, January 2006.

[21] Jeffrey T. Borenstein, Malinda M. Tupper, Peter J. Mack, Eli J. Weinberg, Ahmad S. Khalil, James Hsiao, and Guillermo Garca-Cardea. Functional endothelialized microvascular networks with circular cross-sections in a tissue culture substrate. *Biomedical Microdevices*, 12(1):71–79, September 2009.

[22] Willie Wu, Christopher J. Hansen, Alejandro M. Aragn, Philippe H. Geubelle, Scott R. White, and Jennifer A. Lewis. Direct-write assembly of biomimetic microvascular networks for efficient fluid transport. *Soft Matter*, 6(4):739–742, 2010.

[23] Willie Wu, Adam DeConinck, and Jennifer A. Lewis. Omnidirectional Printing of 3D Microvascular Networks. *Advanced Materials*, 23(24):H178–H183, June 2011.

[24] Du T. Nguyen, Y T. Leho, and Aaron P. Esser-Kahn. The Effect of Membrane Thickness on a Microvascular Gas Exchange Unit. *Advanced Functional Materials*, 23(1):100–106, January 2013.

[25] Du T. Nguyen, Y T. Leho, and Aaron P. Esser-Kahn. A three-dimensional microvascular gas exchange unit for carbon dioxide capture. *Lab on a Chip*, 12(7):1246, 2012.

[26] David C. Duffy, J. Cooper McDonald, Olivier J. A. Schueller, and George M. Whitesides. Rapid Prototyping of Microfluidic Systems in Poly(dimethylsiloxane). *Analytical Chemistry*, 70(23):4974–4984, December 1998.

[27] J. Cooper McDonald and George M. Whitesides. Poly(dimethylsiloxane) as a Material for Fabricating Microfluidic Devices. *Accounts of Chemical Research*, 35(7):491–499, July 2002.

[28] Satish G. Kandlikar. Heat Transfer Mechanisms During Flow Boiling in Microchannels. *Journal of Heat Transfer*, 126(1):8–16, 2004.

[29] Wei Li, Kun Liu, Ryan Simms, Jesse Greener, Dinesh Jagadeesan, Sascha Pinto, Axel Gnther, and Eugenia Kumacheva. Microfluidic Study of Fast GasLiquid Reactions. *Journal of the American Chemical Society*, 134(6):3127–3132, February 2012.

[30] Aaron P EsserKahn, Piyush R Thakre, Hefei Dong, Jason F Patrick, Vitalii K VlaskoVlasov, Nancy R Sottos, Jeffrey S Moore, and Scott R White. Three-Dimensional Microvascular FiberReinforced Composites. *Advanced Materials*, 23(32):3654–3658, August 2011.

[31] Nichola McCann, Duong Phan, Xiaoguang Wang, William Conway, Robert Burns, Moetaz Attalla, Graeme Puxty, and Marcel Maeder. Kinetics and Mechanism of Carbamate Formation from CO_2(aq), Carbonate Species, and Monoethanolamine in Aqueous Solution. *J. Phys. Chem. A*, 113(17):5022–5029, 2009.

[32] Ram Wasudeo Sabnis. *Handbook of acid-base indicators.* CRC Press, Boca Raton, 2007.

[33] Majeed S. Jassim and Gary T. Rochelle. Innovative Absorber/Stripper Configurations for CO_2 Capture by Aqueous Monoethanolamine. *Industrial & Engineering Chemistry Research*, 45(8):2465–2472, April 2006.

[34] James T. Yeh, Henry W. Pennline, and Kevin P. Resnik. Study of CO_2 Absorption and Desorption in a Packed Column. *Energy & Fuels*, 15(2):274–278, March 2001.

[35] G. T. Rochelle. Amine Scrubbing for CO_2 Capture. *Science*, 325(5948):1652–1654, September 2009.

[36] John B Heywood. *Internal combustion engine fundamentals.* McGraw-Hill, New York, 1988.

[37] Milad Abolhasani, Mayank Singh, Eugenia Kumacheva, and Axel Gnther. Automated microfluidic platform for studies of carbon dioxide dissolution and solubility in physical solvents. *Lab on a Chip*, 12(9):1611–1618, 2012.

[38] Milad Abolhasani, Mayank Singh, Eugenia Kumacheva, and Axel Gnther. Cruise control for segmented flow. *Lab on a Chip*, 12(22):4787, 2012.

[39] Hefei Dong, Aaron P. Esser-Kahn, Piyush R. Thakre, Jason F. Patrick, Nancy R. Sottos, Scott R. White, and Jeffrey S. Moore. Chemical Treatment of Poly(lactic acid) Fibers to Enhance the Rate of Thermal Depolymerization. *ACS Applied Materials & Interfaces*, 4(2):503–509, February 2012.

[40] Michael. Caplow. Kinetics of carbamate formation and breakdown. *Journal of the American Chemical Society*, 90(24):6795–6803, November 1968.

[41] P.V. Danckwerts. The reaction of CO_2 with ethanolamines. *Chemical Engineering Science*, 34(4):443–446, January 1979.

[42] Hong-Bin Xie, Yanzi Zhou, Yingkai Zhang, and J. Karl Johnson. Reaction Mechanism of Monoethanolamine with CO_2 in Aqueous Solution from Molecular Modeling. *The Journal of Physical Chemistry A*, 114(43):11844–11852, November 2010.

[43] Michiel T. Kreutzer, Freek Kapteijn, Jacob A. Moulijn, Chris R. Kleijn, and Johan J. Heiszwolf. Inertial and interfacial effects on pressure drop of Taylor flow in capillaries. *AIChE Journal*, 51(9):2428–2440, September 2005.

[44] M. J. F. Warnier, M. H. J. M. Croon, E. V. Rebrov, and J. C. Schouten. Pressure drop of gasliquid Taylor flow in round micro-capillaries for low to intermediate Reynolds numbers. *Microfluidics and Nanofluidics*, 8(1):33–45, May 2009.

[45] Trine G. Amundsen, Lars E. i, and Dag A. Eimer. Density and Viscosity of Monoethanolamine + Water + Carbon Dioxide from (25 to 80) °C. *Journal of Chemical & Engineering Data*, 54(11):3096–3100, November 2009.

[46] Gonzalo Vzquez, Estrella Alvarez, Jos M. Navaza, Raquel Rendo, and Eva Romero. Surface Tension of Binary Mixtures of Water + Monoethanolamine and Water + 2-Amino-2-methyl-1-propanol and Tertiary Mixtures of These Amines with Water from 25 °C to 50 °C. *Journal of Chemical & Engineering Data*, 42(1):57–59, January 1997.

[47] EPA. *Light-Duty Automotive Technology, Carbon Dioxide Emissions, and Fuel Economy Trends: 1975 Through 2011*, March 2012.

Chapter 6

Photothermal Release of CO_2 from Capture Solutions

6.1 Introduction

Using waste heat provided an alternative energy source for the desorption of CO_2 from MEA. However, this still ultimately draws energy from the power plant. We explored the use of solar energy as a means of using an energy source completely separate from the power plant in order to further reduce energy costs.

Recently, the Halas group reported a nanoparticle system for photo-thermal steam generation with 80% of the absorbed light energy converting water into steam.[9, 10] Intriguingly, the vapor generation was observed even when the bulk solution remained below boiling temperatures. The concept of nanoparticle heating has also been previously reported for use in amine scrubbing for microgravity environments.[11] Here we demonstrate the regeneration of CO_2 capture liquids using actinic light and light absorbing nanoparticles of carbon black (NCB), with an aqueous capture solution reaching bulk temperatures of 50 °C. This

mechanism of regeneration is not exclusive to aqueous systems as photothermal release of CO_2 also occurred in a CO_2 binding organic liquid (CO_2BOL).[12, 13] We characterized the photothermal effect by measuring the quantity of CO_2 released with respect to the incoming actinic light. The solution regeneration efficiency of CO_2 increased with higher carbon black concentration and higher initial temperatures. The largest regeneration efficiency was found to be 3.6 mol CO_2/MJ using 65 °C initial temperature, 0.1 wt% NCB, with MEA as the CO_2 capture fluid. The highly localized heat and regeneration provided by nanoparticles enables new approaches for solar energy use in carbon capture and release.

Gold and carbon black nanoparticles are strong absorbers of light and can generate water vapor in the presence of sunlight.[9, 10, 14–18] In the hypothesized mechanism, a gas film initially forms around the nanoparticles (Figure 6.1). The gas films lower thermal conductivity insulates the nanoparticle surface - increasing its surface temperature. The gas volume surrounding the nanoparticle grows until the gas is released at the bulk solution surface. Once released, the nanoparticle returns to the solution and reinitiates the process. In an alternative hypothesis, the collective heating effect of the nanoparticles raises the liquid temperature to the boiling point.[19] Nucleation centers, such as small gas bubbles or NCB, can diffuse through the liquid and enter a superheated area which initiates the vapor formation.

6.2 Experimental

For ease of use and cost, we chose commercially available carbon black nanoparticles (Cabot, N115) for all experiments. Many carbon blacks exist with varying particle sizes, aggregate sizes surface areas, surface chemistry, and other properties. Carbon black N115 was specifically chosen as it was previously used in nanofluid studies.[10, 16] Carbon black absorbs a broad range of radiant energy wavelengths, including visible and IR radiation.[16] Before use, nanoparticles were pre-treated to increase their water solubility. 5 g of the carbon black

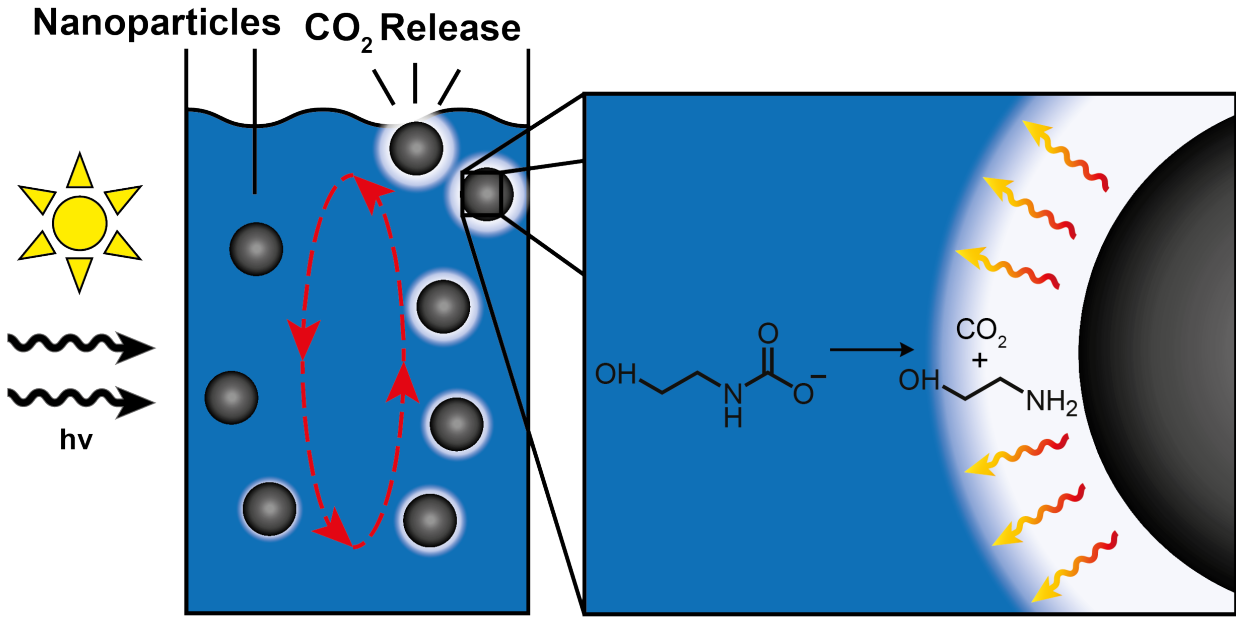

Figure 6.1: Carbon black nanoparticle CO_2 regeneration. Carbon black nanoparticles absorb actinic light and convert it to thermal energy, resulting in a high local temperature near the nanoparticle surface. At the surface, CO_2 is regenerated from MEA, forming a gas bubble around the nanoparticle. The bubble can grow large enough to force the nanoparticle to the surface of the fluid and release CO_2.

nanoparticles were added to 100 mL of 30% H_2O_2 in a round bottom flask and boiled while stirring for 24 hours. The solution was then filtered and dried at 85 °C under vacuum for 24 hours. The pretreated carbon black was dispersed into a capture liquid (7 molal/4.9 molar/30 wt% MEA in H_2O, CO_2BOL) under ultrasonic vibration for 20 minutes, producing a capture fluid and nanoparticle dispersion, also known as a nanofluid.

The regeneration efficiency was measured using the CO_2 release rate and actinic light (Figure 6.3 a). A 50 mL round bottom flask containing 40 mL of the NCB/capture fluid mixture was loaded gravimetrically with CO_2 by bubbling the solution with pure CO_2 to 10 wt% (0.5 mol CO_2/mol MEA) loading. The flask was then connected to a constant air flow of 0.2 L/min and stirred at 500 rpm. The light source was turned on, initiating the photothermal release of CO_2 into the gas detection stream. To remove any evaporating liquids from the system, the gas stream was filtered through condensing and drying tubes. Last, to measure CO_2 concentration, the output of the system flowed through an IR CO_2 meter. Concentration and flow rate were combined to calculate the release rate of CO_2. Experiments were run in triplicate. Repeated measurements and comparisons to mass balance measurements were also conducted to validate the methodology (Figure 6.2). Light sources included LED lights or photography spotlights with powers of 0.8 W and 2.6 W respectively (incident to the flask). The refraction and Fresnel reflection of light resulted in 85% of the incident light passing into the flask (Figure 6.5). The intensity output was measured using an Ambient Weather TM-206 Solar Power Meter with a spectral sensitivity range of 400 nm to 1100 nm. Each system was characterized with respect to the amount of radiant energy required per mol of CO_2 released.

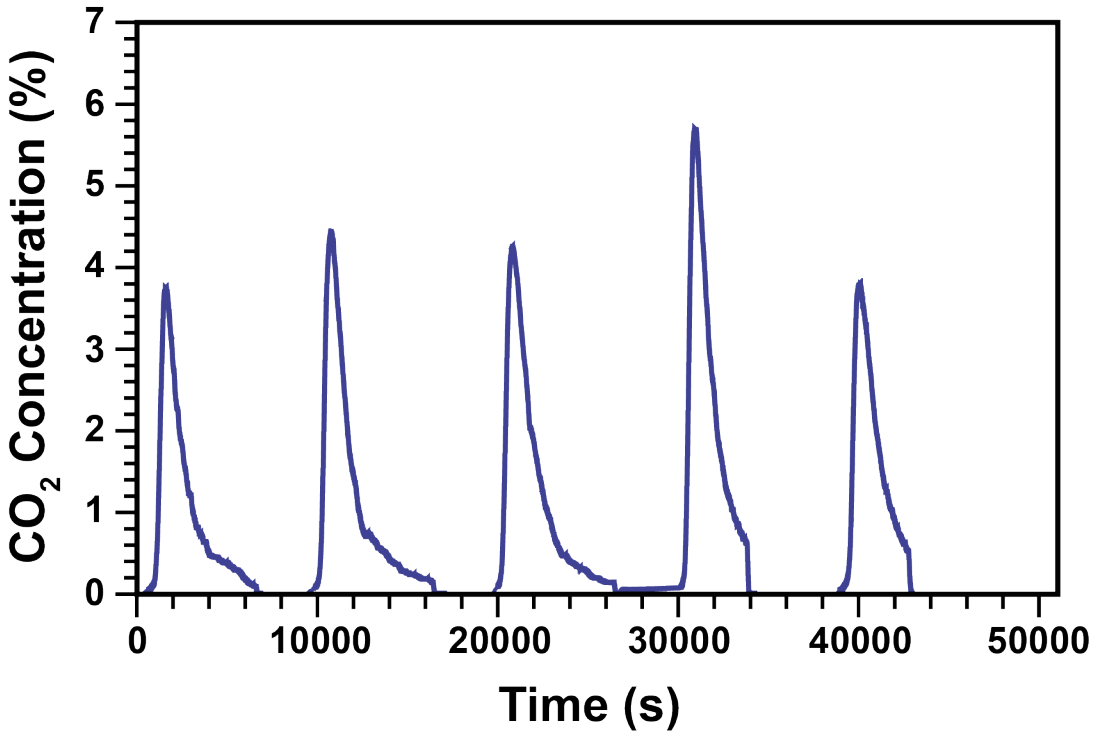

Figure 6.2: Repeated CO_2 measurement. 5 trials were conducted, resulting in 10% differences.

6.2.1 CO_2 Measurment Calibration

The repeatability of the photothermal CO_2 release was initially measured over the course of 5 trials using 30 wt% MEA loaded to 10 wt% CO_2 (Figure 6.2). Nanoparticle concentrations were set to 0.2 % wt. Total CO_2 release was found to be within 10% uncertainty. The CO_2 measurement setup was also compared to the mass loss as measured by a mass balance of the liquid. The difference between the values measured by the CO_2 meter and the mass balance of the liquid for all 5 runs are under 7% difference. The largest differences indicate that the meter measures less mass loss as compared to the mass balance. This difference could be attributed to additional loss of water that would not be measured by the CO_2 meter.

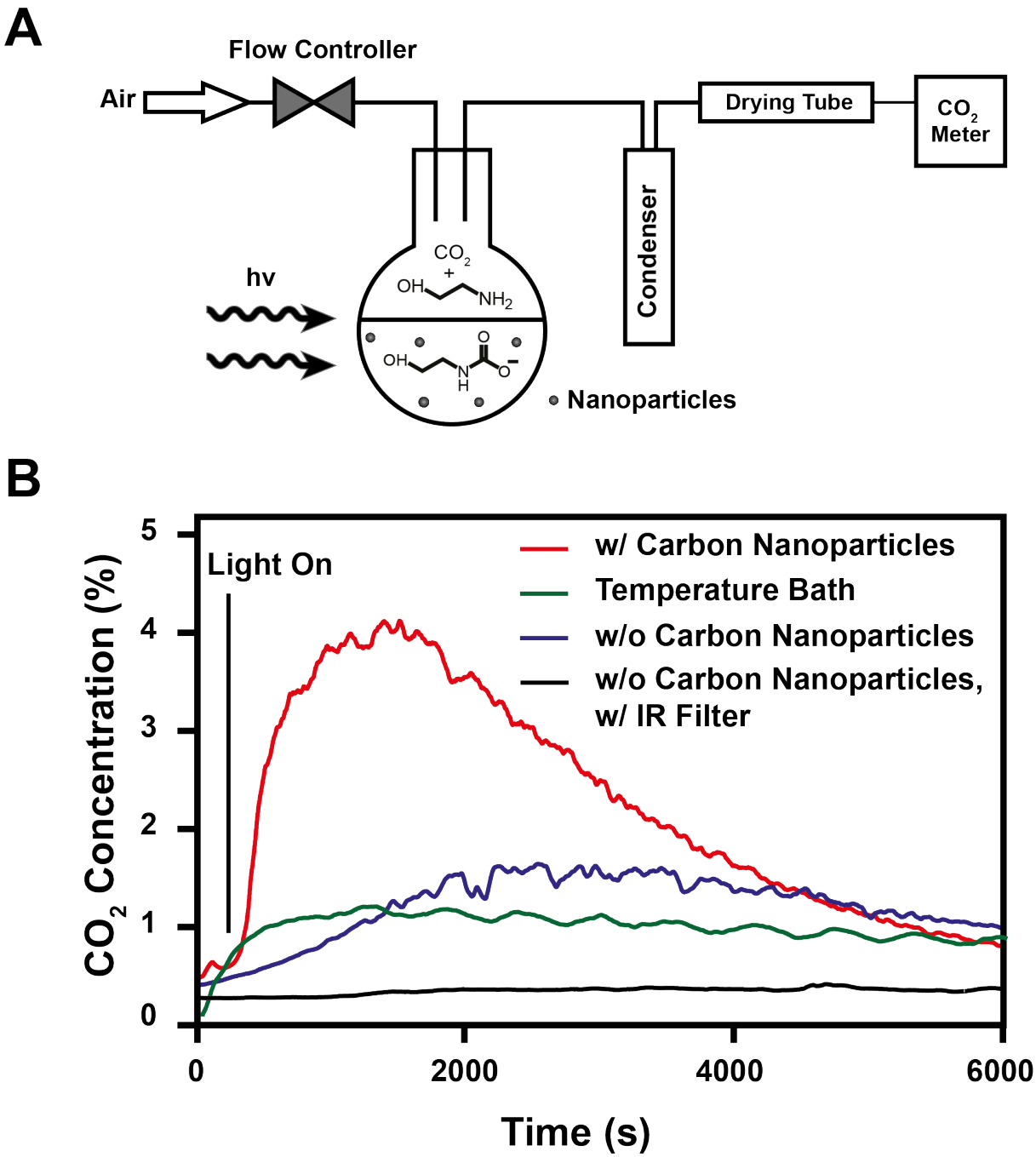

Figure 6.3: CO_2 regeneration measurements. (A) Experimental schematic. Carbon black nanoparticles added to a carbon capture fluid, such as MEA. Air flows through the flask, across a condenser and drying tube, finally reaching a CO_2 meter. Light shines through the flask, releasing CO_2 - measured by the CO_2 meter. The concentration of CO_2, light irradiance, and flow rate are used to calculate the regeneration efficiency. (B) Representative data. Release of CO_2 is triggered by light in MEA. After 2,000 sec, the maximum amount of CO_2 is released and the release rate of CO_2 slows. Some CO_2 is released without carbon black due to the IR transmittance of the light source, resulting in increased bulk fluid temperatures.

Trial	Measured CO_2 Release (g)		% Difference
	CO_2 Meter	Mass Balance	
1	0.604	0.645	6.4
2	0.748	0.741	0.9
3	0.763	0.760	0.4
4	0.680	0.726	6.3
5	0.624	0.636	1.9

6.3 Results and Discussion

More CO_2 was released when NCB was present in the solution and was confirmed by ^{13}C NMR (Figure 6.3 b). Some CO_2 was also released when NCB was absent from the solution. The release of CO_2 without NCB can be explained by two factors. First, water and glass absorb IR radiation (inherent in both solar and actinic light). This absorption results in a bulk solution temperature increase (up to 50 °C) that releases detectable amounts of CO_2. Second, the stream of air, used for measurements, has a low partial pressure of CO_2. The low partial pressure shifts the vapor equilibrium, further releasing CO_2. When an IR filter was applied, the CO_2 concentration within the detection stream was reduced to <0.5% indicating that IR is largely responsible for background release. For further experiments, to simulate potential use, IR filters were not applied as solar energy includes IR wavelengths. As a comparison to the photothermal method, a 50 °C water bath was also used to induce the release of CO_2. The total regeneration of CO_2 was similar to the solution without carbon black, though the profiles were distinctive. To support that photothermal release of CO_2 was not due to bulk heating or the low partial pressure of CO_2 in our apparatus, we compared release profiles of a bulk temperature bath to a computational model of CO_2 solubility in MEA (Figure 6.6).[20]

As the nanoparticles enhanced release of CO_2, we examined CO_2 release as a function of NCB concentration in solution. MEA was used as the capture fluid and was illuminated by the 2.6 W light source. We found that higher concentrations of nanoparticles resulted in

higher regeneration efficiencies (Figure 6.4 a). Solutions with no nanoparticles still released some CO_2, but at lower levels due to IR absorption. Bulk solution temperatures reached 50 °C (Figure 6.8). A possible hypothesis for the enhanced solution regeneration is that the increased concentration, and therefore number of nanoparticles, created greater surface area for the localized heating and nucleation of CO_2. Concentrations of nano-particles above 0.15 wt% did not result in higher regeneration efficiencies. Above this concentration, all light was absorbed by the nanofluid and no further absorption occurred. The addition of the NCB to the solution also increased the working capacity of the fluid within the examined region from 1wt% CO_2 in solution (with no NCB) to 2.3 wt% CO_2 in solution (at 0.2 wt% NCB).

Next, we examined the effects of the bulk solution temperature on regeneration efficiency. In most solution regeneration configurations, the temperature of the incoming CO_2 rich solution is elevated above room temperature as the reaction with CO_2 is exothermic. The bulk temperature of the solution was modulated by flowing preheated water through the solution via a stainless steel tube. This internal heating method was used to minimize the shading of the nanoparticle solution. The NCB concentration was 0.1 wt%. As expected, higher initial temperatures resulted in increased regeneration efficiency (Figure 6.4 b). At higher temperatures, the energy difference between the initial state and the regeneration state is lower. The high initial temperature allows more of the photo-thermal energy to release CO_2 and regenerate the fluid since less energy is spent heating the solution to the higher temperatures. The largest efficiency in the scope of this report was found at 65°C (3.6 mol CO_2/MJ).

Last, as many capture and release schemes do not use aqueous amines, we examined if the photothermal CO_2 release was compatible with a non-aqueous alkyl guanidinium CO_2 capture fluid, referred to as CO_2BOL.[12, 13] Specifically, a combination of tetramethylguanidine and 1-butanol in dimethylformamide was used (0.5 M each). CO_2BOLs bind CO_2 as an alkylcarbonate salt and does not require water as a solvent. In the nanoparticle regeneration

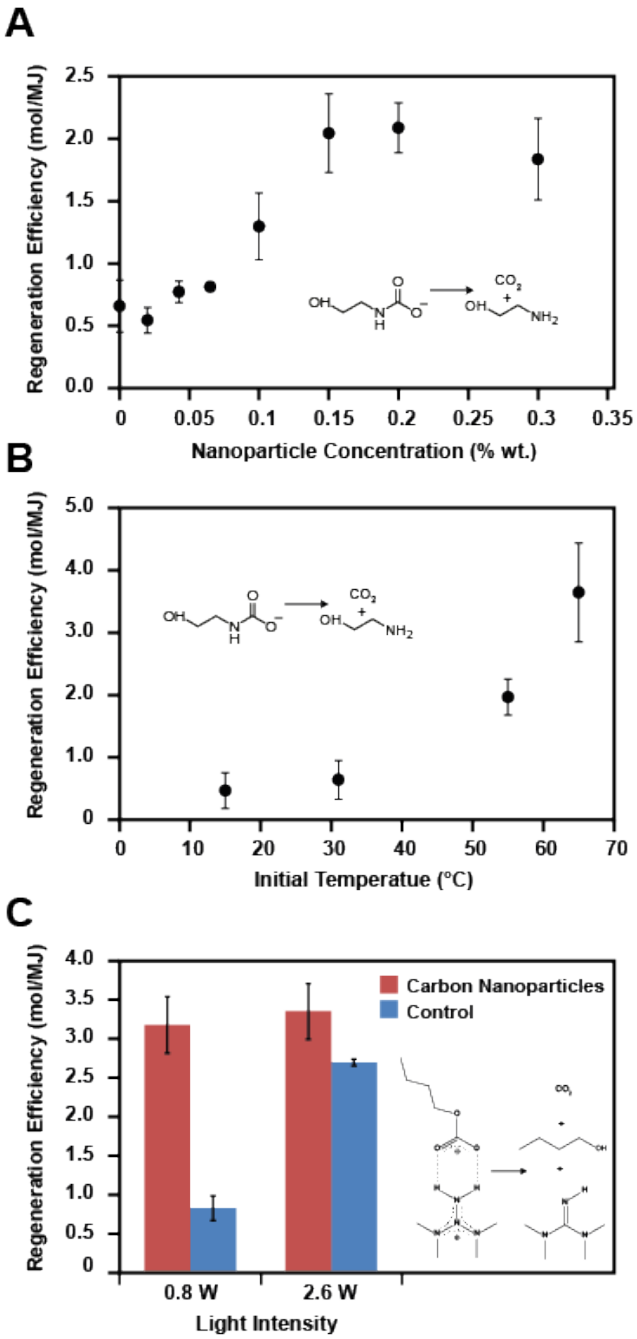

Figure 6.4: Regeneration efficiencies. (A) Carbon nanoparticle concentration. Regeneration efficiency increased with increasing nanoparticles concentration. Bulk temperatures reached 50 °C (B) Initial temperature. As the initial temperature of the capture fluid increased, an increase in the regeneration efficiency was found. This might influence applications as regenerators contain capture fluids at elevated temperatures. 0.1 wt% NCB concentration was used (C) CO_2BOL. The carbon black nanoparticles also released CO_2 in non-aqueous systems. Due to the lower desorption temperature profile of the CO_2BOL, the higher intensity light source was sufficient to remove CO_2 with and without nanoparticles. A lower intensity LED light source increases CO_2 regeneration only with nano-particles present.

system, the CO_2BOL had a greater regeneration efficiency than MEA (Figure 6.4 c). The solvent for the CO_2BOL, dimethylformamide, has a lower heat capacity and lower thermal conductivity than water, which results in increased local temperatures and higher regeneration efficiencies. We found that the 2.6 W light source induced CO_2 release in CO_2BOL both with and without the NCB. The lower regeneration temperature of the CO_2BOL allowed the solution to obtain similar regeneration efficiencies between the solution without nanoparticles and the solution with nanoparticles. The enhanced regeneration efficiency was observed by using the lower intensity, 0.8 W LED lights. At higher intensities, nucleation boiling may be a larger driving force for desorption rather than high localized temperatures since the bulk solution temperatures reach regeneration temperatures. The regeneration efficiency of the CO_2BOL increased 380% between the CO_2BOL with and without carbon black, when illuminated with the 0.8 W light source.

We examined the potential performance of solar energy regeneration with a nanofluid system by estimating the surface area of incident solar light required to regenerate MEA used in a 500 MW coal-fired power plant. In such a plant, on average, 2500 mol CO_2/sec are emitted.[21]20 With an average solar insolation of 561 W/m^2, an estimated 1.22 km^2 of surface area would be required to regenerate MEA, assuming 0.1 wt % NCB and an initial temperature of 65 °C.[22] The average solar insolation value was based on the average daytime direct normal solar insolation in Ward County, Texas which was reported by Cohen et al. as a comparative value for estimating the use of solar thermal energy for post-combustion CO_2 capture.[22] Our calculation assumes a flat surface as the interaction area between sunlight and the capture fluid. As a comparison, the Solar Energy Generating System in California[23] covers a total of 2.3 km^2 of field area, with the largest plant covering a field area of 0.48 km^2. Further optimization such as improved geometries, light collection, and thermal insulation could result in higher regeneration efficiencies and lower land usage. However, energy would still be required to pump the MEA and to compress the released CO_2 for storage. The physical effects of NCP on process equipment was not examined as part of this study. A potential

incorporation platform could be the use of parabolic troughs with the CO_2 capture nanofluid. Detailed process conditions, simulations, and cost analysis have yet to be performed and are beyond the scope of this initial publication.

6.4 Theoretical

6.4.1 Optical Simulation

The energy of light entering the round bottom flask was estimated using POV-Ray1, an optical ray tracing program. The refraction and Fresnel reflection of light causes loss of the some incident radiant (Figure 6.5 a). The software simulates the optical conditions of the system and can provides an estimate of the radiant energy entering the flask (Figure 6.5 b). A round bottom flask was cross-sectioned with a measuring plane where the pixel intensity can be measured (Figure 6.5 c). By comparing the average pixel intensity within the cross section and outside of the cross section, the fraction of lost light was estimated to be 15% as the flask reflects some light and does not contains anti-reflective coatings. This was experimentally confirmed using a modified cuvette to measure the light emission spectra. Within the same spatial coordinates, the irradiance was measured in open air and within a round bottom flask confirming the 15% energy loss.

6.4.2 CO_2 Solubility in MEA Model

activity-fugacity approach reported by Tong et al (Figure 6.6).[20] The model combines physical equilibria, chemical equilibria, and phase nonidealities to generate information on

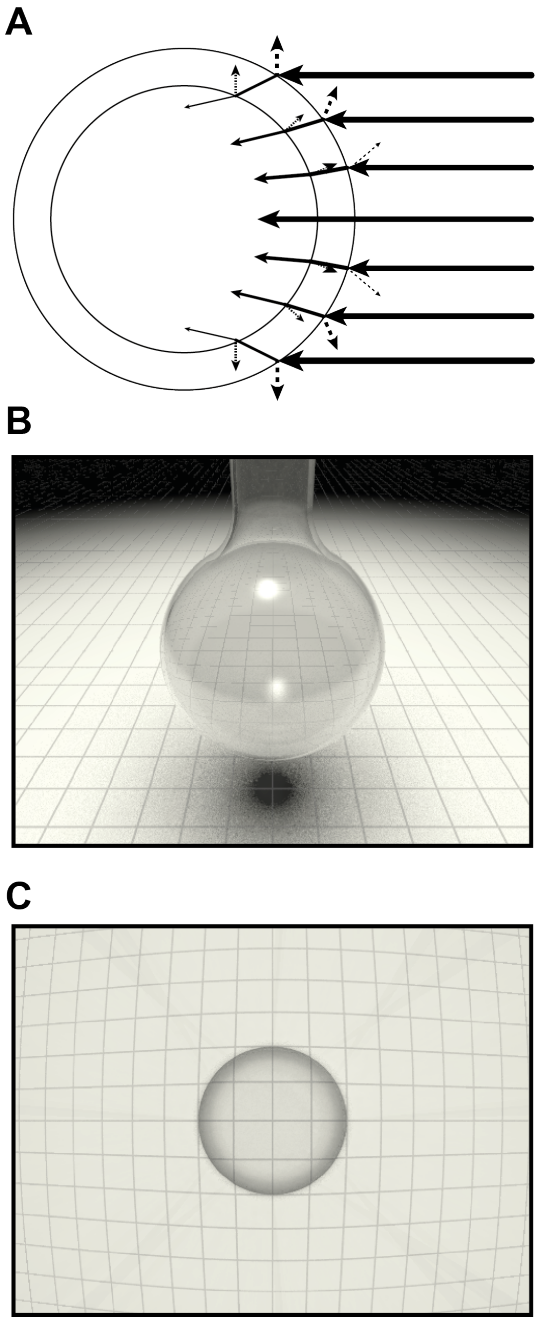

Figure 6.5: Optical simulation. (A) Ray tracing. Light is lost as refraction and Fresnel reflection diverts some of the light from the flask. (B) POV-Ray simulation. A representative simulation is shown to demonstrate the capabilities of the software. (C) Lost energy measurement. Half the flask is placed above a measurement plane. The amount of light that passes through the flask is compared to the light that directly hits the grid.

the vapor-liquid equilibria of CO_2 and MEA at given temperatures and pressures.

$$CO_2(g) \overset{HCO_2}{\longleftrightarrow} CO_2(l) \tag{6.1}$$

$$2H_2O \overset{K_1}{\longleftrightarrow} H_3O^+ + OH^- \tag{6.2}$$

$$CO_2 + 2H_2O \overset{K_2}{\longleftrightarrow} H_3O^+ + HCO_3^+ \tag{6.3}$$

$$HCO_3^+ + H_2O \overset{K_3}{\longleftrightarrow} H_3O^+ + CO_3^{2-} \tag{6.4}$$

$$RNH_3^+ + H_2O \overset{K_4}{\longleftrightarrow} RNH_2 + H_3O^+ \tag{6.5}$$

$$RNHCOO^- + H_2O \overset{K_5}{\longleftrightarrow} RNH_2 + HCO_3^- \tag{6.6}$$

Further information on the model can be found from Tong et al.[20]

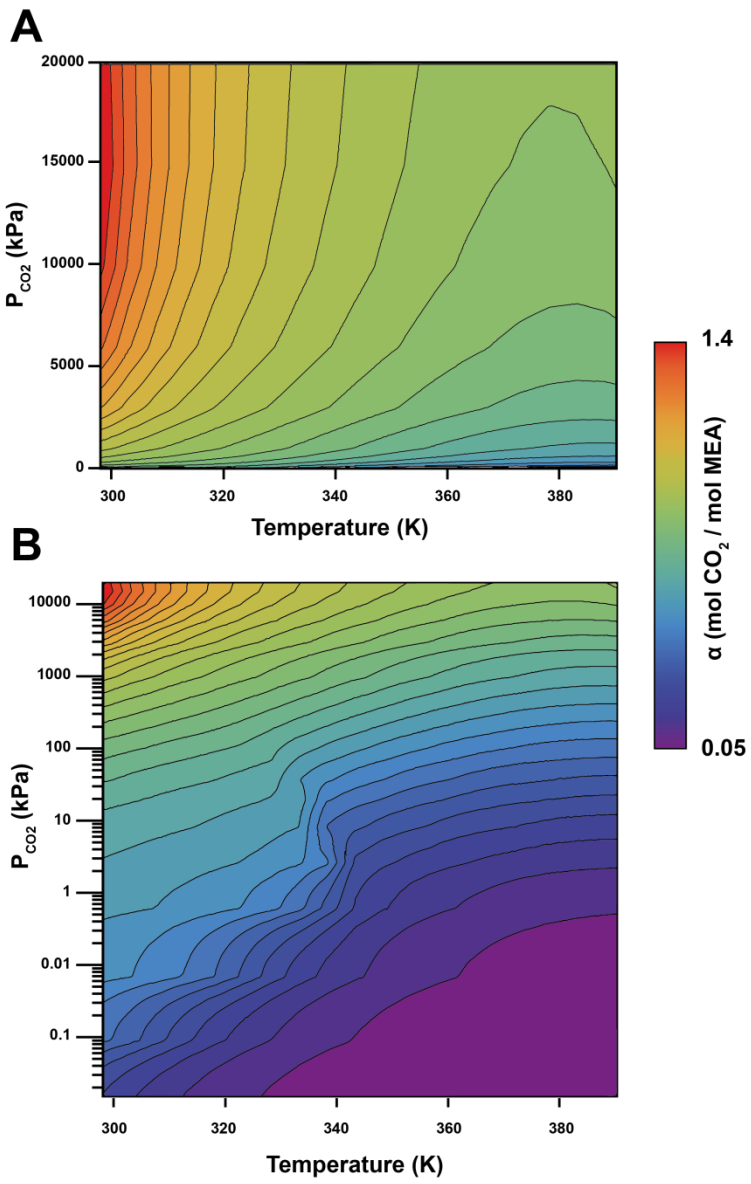

Figure 6.6: CO_2 Solubility in MEA Model based on Tong et. al. (A) Linear contour plot. At high pressures and low temperatures, CO_2 is most soluble in MEA. (B) Log scale contour plot.

The equilibria was used to estimate the predicted release of CO_2 with given temperature changes by numerically solving (Eq 7)

$$\frac{\delta\alpha(t)}{\delta t} = -r\left(\alpha(t) - \alpha_{eq}(T(t), P(t))\right)^3 \tag{6.7}$$

The rate constant was empirically estimated to match experimentally collected data. Data on the solubility of CO_2 was previously collected by Jou et al. at 313K (Figure 6.7 a).[24] At loading pressures and temperatures used in this report, 0.5 moles of CO_2 are absorbed per mole of MEA. However, higher loading capacities are possible at higher CO_2 pressures. The model matched well with their reported data. The predicted release of CO_2 was compared with an experiment in which 40 mL of MEA was immersed in a 50 °C water bath. The measured release rate matched well with the predicted results (Figure 6.7 b).

Temperature evolutions of time were also measured for the two extremes of NCB concentration (Figure 6.8 a). Using these temperature profiles for the model, a predicted release of CO_2 was constructed by the model (Figure 6.8 b). While the model was accurate for bulk temperature increases and the resulting CO_2 release, the photothermal release of CO_2 resulted in greater release than was predicted.

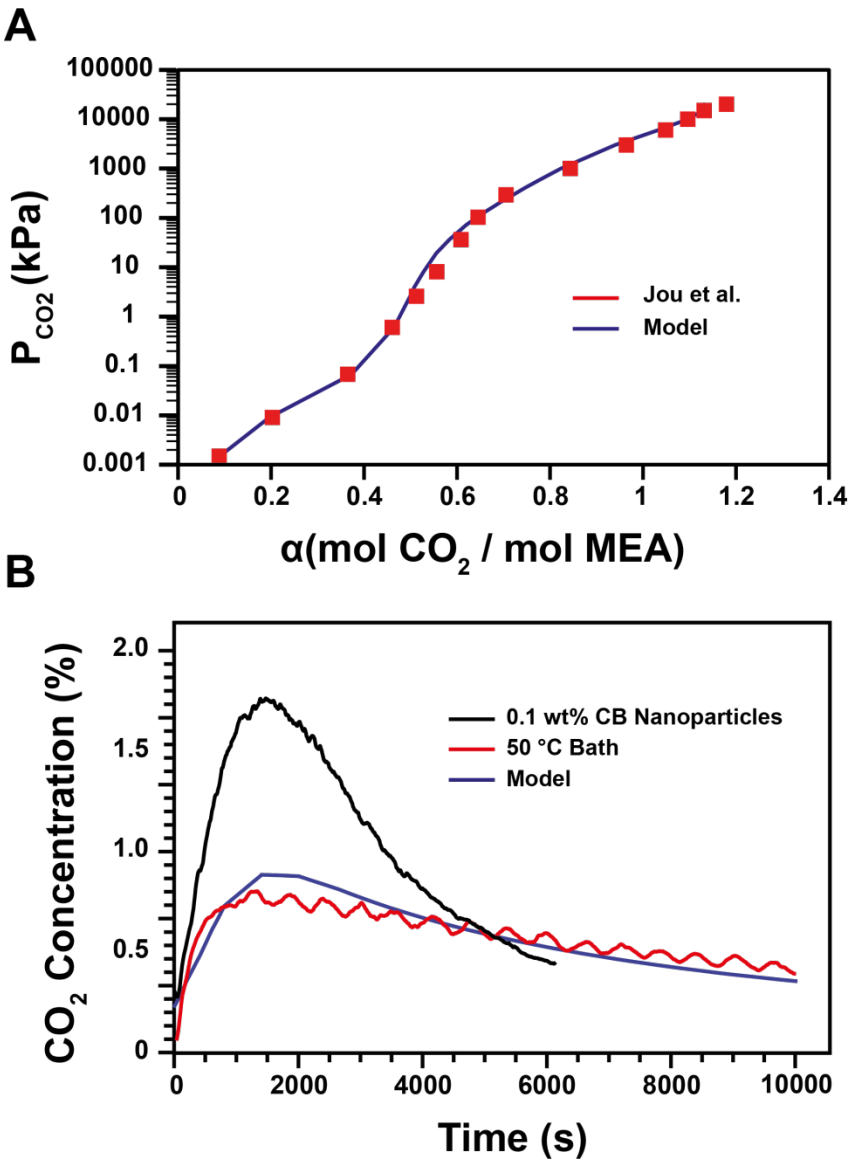

Figure 6.7: Experimental and model results. (A) Correlation of model and Jou et al. at 40 °C. (B) Correlation of model and experimental release rate at 50 °C.

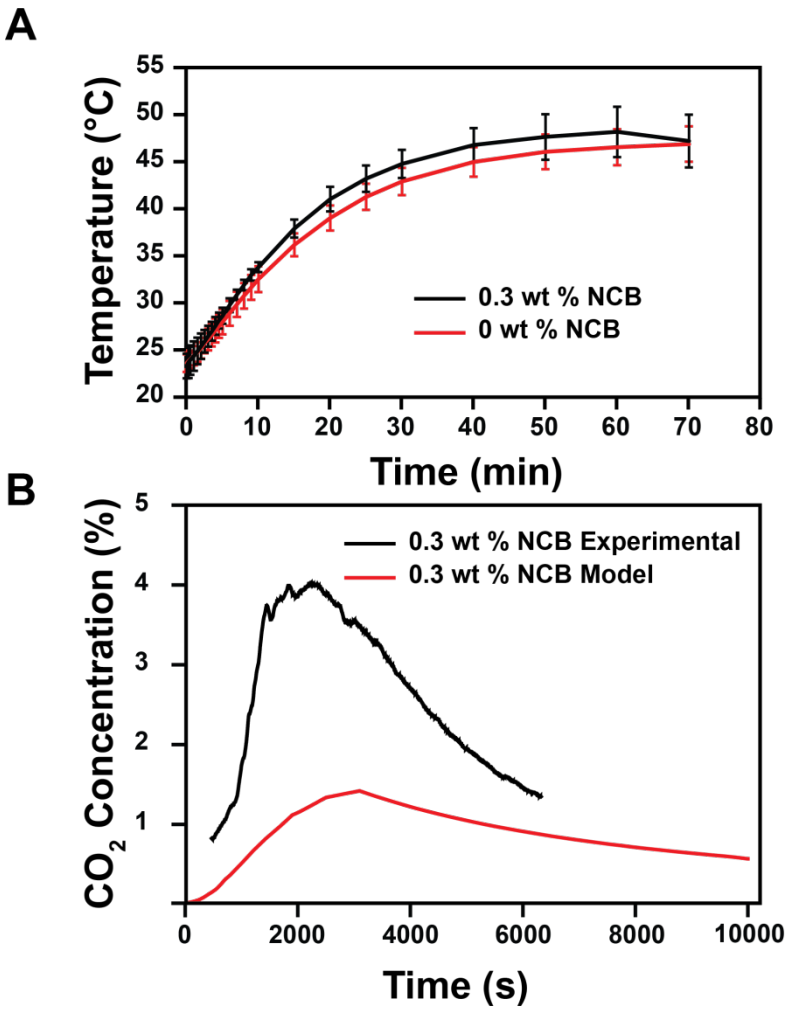

Figure 6.8: Photothermal temperature evolution. (A) Temperature evolutions. Temperature profiles were measured with respect to time at 0 wt% and 0.3 wt% NCB using a thermocouple. Bulk temperatures only show minor differences. (B) CO_2 release model. Experimental temperature evolutions were inputted into the model to produce the expected CO_2 release profile. The increased CO_2 release between the experiment and model indicate enhanced release due to the presence of the NCB

Bibliography

[1] P. Friedlingstein, R. A. Houghton, G. Marland, J. Hackler, T. A. Boden, T. J. Conway, J. G. Canadell, M. R. Raupach, P. Ciais, and C. Le Qur. Update on CO_2 emissions. *Nature Geoscience*, 3(12):811–812, November 2010.

[2] Ryan P. Lively, Ronald R. Chance, B. T. Kelley, Harry W. Deckman, Jeffery H. Drese, Christopher W. Jones, and William J. Koros. Hollow Fiber dsorbents for CO_2 Removal from Flue Gas. *Industrial & Engineering Chemistry Research*, 48(15):7314–7324, 2009.

[3] Dean Camper, Jason E. Bara, Douglas L. Gin, and Richard D. Noble. Room-Temperature Ionic LiquidAmine Solutions: Tunable Solvents for Efficient and Reversible Capture of CO_2. *Industrial & Engineering Chemistry Research*, 47(21):8496–8498, November 2008.

[4] Hailian Li, Mohamed Eddaoudi, M. O'Keeffe, and O. M. Yaghi. Design and synthesis of an exceptionally stable and highly porous metal-organic framework. *Nature*, 402(6759): 276–279, November 1999.

[5] Howard J. Herzog. Peer Reviewed: What Future for Carbon Capture and Sequestration? *Environmental Science & Technology*, 35(7):148A–153A, April 2001.

[6] DeannaM. D'Alessandro, Berend Smit, and JeffreyR. Long. Carbon Dioxide Capture: Prospects for New Materials. *Angewandte Chemie International Edition*, 49:6058–6082, August 2010.

[7] Babatunde A. Oyenekan and Gary T. Rochelle. Energy Performance of Stripper Configurations for CO_2 Capture by Aqueous Amines. *Industrial & Engineering Chemistry Research*, 45(8):2457–2464, April 2006.

[8] Stefano Freguia and Gary T. Rochelle. Modeling of CO_2 capture by aqueous monoethanolamine. *AIChE Journal*, 49(7):1676–1686, July 2003.

[9] Oara Neumann, Curtis Feronti, Albert D. Neumann, Anjie Dong, Kevin Schell, Benjamin Lu, Eric Kim, Mary Quinn, Shea Thompson, Nathaniel Grady, Peter Nordlander, Maria Oden, and Naomi J. Halas. Compact solar autoclave based on steam generation using broadband light-harvesting nanoparticles. *Proceedings of the National Academy of Sciences*, 110(29):11677–11681, July 2013.

[10] Oara Neumann, Alexander S. Urban, Jared Day, Surbhi Lal, Peter Nordlander, and Naomi J. Halas. Solar Vapor Generation Enabled by Nanoparticles. *ACS Nano*, 7(1): 42–49, January 2013.

[11] Joseph Cole. *Photothermal Energy Conversion by Plasmonic Nanoparticles*. PhD Thesis, Rice University, 2009.

[12] David J. Heldebrant, Clement R. Yonker, Philip G. Jessop, and Lam Phan. Organic liquid CO_2 capture agents with high gravimetric CO2 capacity. *Energy & Environmental Science*, 1:487–493, 2008.

[13] David J. Heldebrant, Clement R. Yonker, Philip G. Jessop, and Lam Phan. CO_2 -binding organic liquids (CO_2 BOLs) for post-combustion CO_2 capture. *Energy Procedia*, 1(1): 1187–1195, February 2009.

[14] Hui Zhang, Hui-Jiuan Chen, Xiaoze Du, and Dongsheng Wen. Photothermal conversion characteristics of gold nanoparticle dispersions. *Solar Energy*, 100:141–147, February 2014.

[15] Robert A. Taylor, Patrick E. Phelan, Todd Otanicar, Ronald J. Adrian, and Ravi S. Prasher. Vapor generation in a nanoparticle liquid suspension using a focused, continuous laser. *Applied Physics Letters*, 95(16):161907, 2009.

[16] Dongxiao Han, Zhaoguo Meng, Daxiong Wu, Canying Zhang, and Haitao Zhu. Thermal properties of carbon black aqueous nanofluids for solar absorption. *Nanoscale Research Letters*, 6(1):457, 2011.

[17] Alexander O. Govorov and Hugh H. Richardson. Generating heat with metal nanoparticles. *Nano Today*, 2(1):30–38, February 2007.

[18] W.J. Minkowycz, E.M. Sparrow, and J.P Abraham, editors. *Nanoparticle heat transfer and fluid flow*. Number volume 4 in Series in computational and physical processes in mechanics and thermal sciences. CRC Press/Taylor & Francis Group, Boca Raton, 2013.

[19] Susil Baral, Andrew J. Green, Maksim Y. Livshits, Alexander O. Govorov, and Hugh H. Richardson. Comparison of Vapor Formation of Water at the Solid/Water Interface to Colloidal Solutions Using Optically Excited Gold Nanostructures. *ACS Nano*, 8(2): 1439–1448, February 2014.

[20] Danlu Tong, J.P. Martin Trusler, Geoffrey C. Maitland, Jon Gibbins, and Paul S. Fennell. Solubility of carbon dioxide in aqueous solution of monoethanolamine or 2-amino-2-methyl-1-propanol: Experimental measurements and modelling. *International Journal of Greenhouse Gas Control*, 6:37–47, January 2012.

[21] Kevin S. Fisher, Carrie Beitler, Curtis Rueter, Katherine Searcy, Gary Rochelle, and Majeed Jassim. Integrating MEA Regeneration with CO_2 Compression and Peaking to Reduce CO_2 Capture Costs. Technical Report DOE/ER/84111, USDOE Office of Fossil Energy (FE) Report DOE/ER/84111, June 2005.

[22] Stuart M. Cohen, Michael E. Webber, and Gary T. Rochelle. Utilizing Solar Thermal Energy for Post-Combustion CO_2 Capture. *Journal of Energy and Power Engineering*, 5:195–208, March 2011.

[23] Hank Price, Eckhard Lpfert, David Kearney, Eduardo Zarza, Gilbert Cohen, Randy Gee, and Rod Mahoney. Advances in Parabolic Trough Solar Power Technology. *Journal of Solar Energy Engineering*, 124(2):109–125, 2002.

[24] Fang-Yuan Jou, Alan E. Mather, and Frederick D. Otto. The solubility of CO_2 in a 30 mass percent monoethanolamine solution. *The Canadian Journal of Chemical Engineering*, 73(1):140–147, 1995.

Chapter 7

Conclusions

7.1 Biomimetic CO_2 Capture

7.1.1 Microvascular Systems

We have demonstrated the ability to precisely control the inter-channel distances of our microvascular gas exchange units at the micro-scale. This allows for the study of the connection between membrane thickness and gas exchange rates. Decreasing the membrane thickness resulted in increased mass transport. Below separations of ~25 μm, the increase in mass transport with respect to the membrane thickness was further accelerated. The presence of micro-dents was found to be the cause of this acceleration and indicates that the entire inter-channel membrane is not required to have uniform thickness to improve mass transfer rates. While we were unable to obtain inter-channel distances below 20 μm due to the leakage of capture fluid between channels, membrane healing processes can potentially be used to repair the areas where leakage occurred and allow for channel separations below 20 μm.[1] Additionally, modifications to the surface chemistry of the channels may further enhance

the reactivity of our microvascular gas exchange units. It has also not escaped our attention that PDMS is not an ideal material and we are interested in exploring alternative materials for synthesizing exchange units in future studies.

7.1.2 Close Packing Structures

We present a computational and experimental comparison of mass and heat exchange between close packed arrangements of circular microchannels - the first such exploration of bio-inspired exchange structures. The computational models created for the close packed exchangers accurately predicted the experimental mass transfer characteristics of each pattern. Predictions for the heat transfer characteristics were less accurate, but similar trends were found. This predictive capability will allow for future design optimization of exchangers. The mass transfer rates, normalized to the capture fluid volume showed large differences between the packing patterns. The "Double Squarer" pattern obtained the highest mass transfer rate. Large differences in the heat transfer characteristics were also observed. Again, the "Double Squarer" pattern obtained the highest heat transfer coefficient of all of the patterns for our preliminary experiments. However, only small variations in the Nusselt numbers were found between the patterns, with the "Dodecagonal" pattern obtaining the lowest. Parameters such as minimum inter-channel distances, mean distances, and channel sizes all play an important role in determining transfer characteristics. These parameters are interconnected, restricting the degrees of freedom when designing a system. Access to other packing geometries allows for a new design parameter. Our fabrication constraints resulted in the "Double Squarer" pattern obtaining the highest transfer rates. These differences in mass and heat transfer are likely to become more pronounced as the size scales of the exchangers decrease further.

These close-packed patterns form the basis of most biological exchange systems. We report

the first synthesis and analysis of these patterns in model exchange systems. These insights and new techniques, inspired by nature, might facilitate the development of novel cooling devices and gas exchangers with applications in electronics, flow chemistry, fuel cells, and many other areas where exchange is needed. Future work in this area will entail making smaller patterns and adding finer features as well as the adaptation of these patterns to specific applications and devices.

7.1.3 Hierarchical Structures

We adapted a method for the coating of polymer template structures and shown its compatibility with a range of polymeric materials and geometries. This coating method was used in conjunction with our template removal process, VaSC, and resulted in hollow membrane structures that were replicas of the initial templates. Several parameters can affect the thicknesses of the membranes formed, including the coating solution composition, residence time, and template size scale. The method is general enough to form coatings of a wide variety of membrane structures. The method was shown to work on a variety of size scales from 100 μm to 5 mm and could conform onto a variety of three-dimensional structure, as demonstrated by the coating of 3D printed objects and thermally induced phase separated templates. Our new polymer membrane coating technique enables coating of many new materials and geometries which should lead to new applications and designs in microvascular structures, self healing composites, and membrane separations.[1–6]

7.2 Novel CO_2 Capture Solvent Regeneration Techniques

7.2.1 Microscale Waste Heat Use

Our results have demonstrated the first adaptable system to use low grade waste-heat from a surface for powering the chemical reaction used in removing CO_2 from a saturated solution. This initial system has been shown to conform, on a lab scale, to both smooth, cylindrical surfaces, and to uneven surfaces using the VaSC fabrication process. The system was demonstrated by flowing a CO_2 saturated solution as the surface was heated. The subsequent chemical reaction resulted in the release of CO_2 from the solution through a two-phase heat transfer phenomenon. This flow-release process was further characterized with respect to flow rates, temperatures, and channel diameters. Increasing the solution residence time, increasing the temperature, and decreasing the channel diameters have all resulted in increased CO_2 release capabilities. The heat transfer coefficients obtained by our microvascular systems (200-1000 W/m^2 K) are lower in comparison to other microscale heat exchangers (5-30 kW/m^2K).[7] However, our initial material (PDMS) is a partial insulator. Furthermore, these microvascular systems conform directly to surfaces which are incompatible with other microscale systems. In the future, we plan to use more conductive materials by integrating conductive elements into conformable polymers. The advantages of these conformal systems allow them to potentially find use in a variety of applications including flow chemistry, thermal management, and removal of CO_2 from saturated solutions. This microvascular system might easily interface with common heated surfaces such as a boiler, radiator, or other pre-existing waste-heat surfaces in order to power chemical reactions and lower parasitic energy loss. Further investigation into the exergy cost of the microvascular system will be required in order to determine the full energy loss of a wider implementation.

7.3 Photothermal CO_2 Desorption

We demonstrate a new potential energy source for carbon capture and release technologies by regenerating capture fluids using actinic light and carbon black nanoparticles. We report that increased nanoparticle concentration and increased initial capture fluid temperatures resulted in higher regeneration efficiencies. The carbon black nanoparticles demonstrated capture fluid regeneration in both aqueous and non-aqueous systems including MEA and CO_2BOL. These photothermal nanoparticles could be incorporated, at low loading levels, into CO_2 capture fluids without affecting chemical absorption. Fossil fuels remain inexpensive and this approach might serve as a temporary stop-gap as renewable energy technologies continue to mature. The use of photothermal nanoparticles might aid in the integration of solar energy with CO_2 capture technologies as an economical intermediate. The incorporation of the nanoparticles enables the use of sunlight, instead of steam, to regenerate the capture fluid as the nanoparticles rapidly reach regeneration temperatures. Our future work will focus on exploring the surface properties of the nanoparticles, effect of particle size, understanding the basic phenomenon of photothermal gas regenerate, reducing the aggregation of nanoparticles, exploring other photothermal nanoparticles, and optimizing system geometry for light absorption.

Bibliography

[1] Kathleen S. Toohey, Nancy R. Sottos, Jennifer A. Lewis, Jeffrey S. Moore, and Scott R. White. Self-healing materials with microvascularnetworks. *Nature Materials*, 6(8):581–585, June 2007.

[2] Leon M. Bellan, Tatiana Kniazeva, Ernest S. Kim, Alla A. Epshteyn, Donald M. Cropek, Robert Langer, and Jeffrey T. Borenstein. Fabrication of a Hybrid Microfluidic System Incorporating both Lithographically Patterned Microchannels and a 3d FiberFormed Microfluidic Network. *Advanced Healthcare Materials*, 1(2):164–167, January 2012.

[3] Ying Zheng, Peter W. Henderson, Nak Won Choi, Lawrence J. Bonassar, Jason A. Spector, and Abraham D. Stroock. Microstructured templates for directed growth and vascularization of soft tissue in vivo. *Biomaterials*, 32(23):5391–5401, August 2011.

[4] Aijuan Zhang, Mingjie Chen, Can Du, Huizhang Guo, Hua Bai, and Lei Li. Poly(dimethylsiloxane) Oil Absorbent with a Three-Dimensionally Interconnected Porous Structure and Swellable Skeleton. *ACS Applied Materials & Interfaces*, 5(20):10201–10206, October 2013.

[5] C. J. Bettinger, E. J. Weinberg, K. M. Kulig, J. P. Vacanti, Y. Wang, J. T. Borenstein, and R. Langer. Three-Dimensional Microfluidic Tissue-Engineering Scaffolds Using a Flexible Biodegradable Polymer. *Advanced Materials*, 18(2):165–169, January 2006.

[6] Aditya Balasubramanian, Robert Morhard, and Christopher J Bettinger. Shape-Memory Microfluidics. *Advanced Functional Materials*, 23(38):4832–4839, 2013.

[7] Stefan S. Bertsch, Eckhard A. Groll, and Suresh V. Garimella. Review and Comparative Analysis of Studies on Saturated Flow Boiling in Small Channels. *Nanoscale and Microscale Thermophysical Engineering*, 12(3):187–227, September 2008.

Appendix A

Appendix

A.1 Microvascular Carbon Capture

A.1.1 Edge Detection

To determine the membrane thicknesses, the optical microscope images were processed with edge and distance detection programs coded in the Mathematica computational software program. The Canny edge detection algorithm was used to detect the edges in the images. The images were first converted to gray scale and a Gaussian blur was applied to remove particulates. The gradient of the intensity at each pixel within the image was approximated with the Sobel matrix operators:

$$G_x = \begin{bmatrix} -1 & 0 & 1 \\ -2 & 0 & 2 \\ -1 & 0 & 1 \end{bmatrix} * A \tag{A.1}$$

$$G_y = \begin{bmatrix} -1 & -2 & -1 \\ 0 & 0 & 0 \\ 1 & 2 & 1 \end{bmatrix} * A \tag{A.2}$$

Where the variables are:

$G = Gradient$

$A = ImageArray$

The gradients of each pixel are then examined to determine if they are local maxima. At each pixel, the value of the gradient was compared to the value in each opposite pixel of the gradient direction, rounded to the nearest 45°. If the current pixel gradient value was the largest in any direction, then it remained the same value. Otherwise, if the current pixel value was smaller, then it was suppressed to 0. This process reduced the edge thicknesses to 1 pixel. A threshold was then set to reduce artifacts in the image. Gradient values above the threshold were set to 1 (white) while values below the threshold were set to 0 (black). Any remaining artifacts in the image were manually removed in an image-editing program.

After the edges were found, images containing only edges were processed with a distance detection algorithm. The spatial coordinates of each white pixel was found first. The coordinates were then separated into groups corresponding to each channel edge. Pairs of groups corresponding to adjacent channel edges were then compared. The distances between each pixel in one group and each pixel in the other group were found. The minima of the distances for each pixel were then calculated, which corresponds to the membrane thickness after converting from pixel distances to real distances. The averages and standard deviation of the distances were then found from the resulting values.

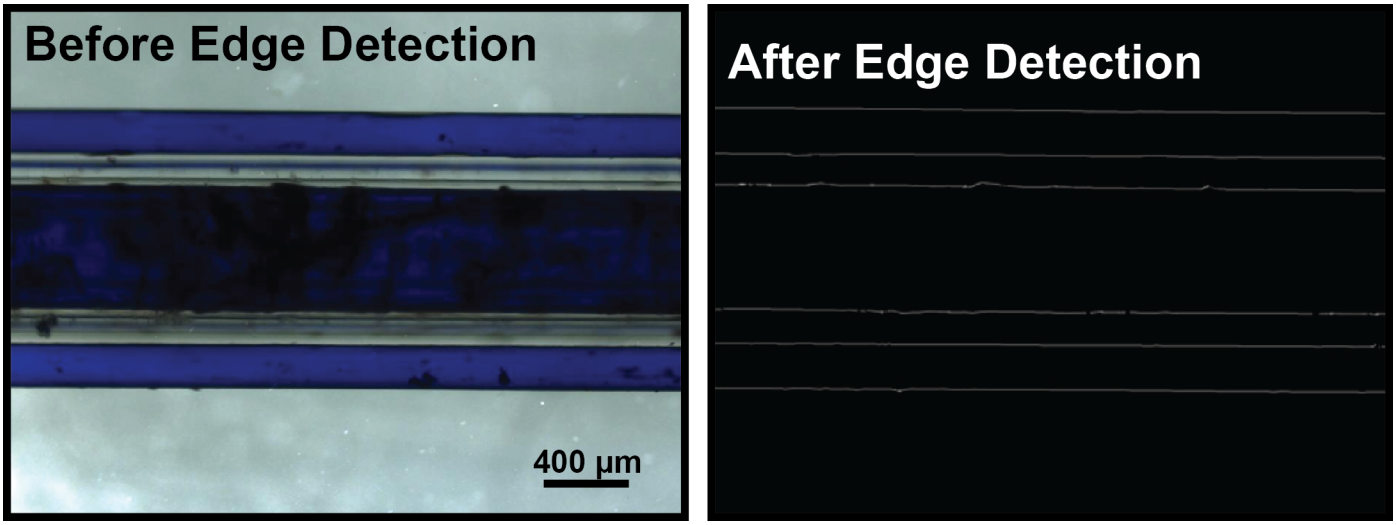

Figure A.1: Edge detection on a hexagonal gas exchange unit with a 500 μm central channel and 20 μm outer channels.

A.1.2 UV-Vis Experimental Details

Solutions of monoethanolamine (MEA) with dye were mixed with a lower dye concentration than the saturation time experiments (0.6 mg dye/mL MEA solution). Scintillation vials were filled with 10 mL of the diluted solution and their masses were obtained using an analytic balance (Denver Instruments SI-234). Pure CO_2 was then bubbled into the solutions at a rate of 0.1 L/min for times ranging from 0 to 10 minutes. The solutions were re-weighed to determine the change in mass and obtain the % wt of CO_2 captured by the solutions. UV-Vis Spectrometry was then performed on the solutions using a Varian Cary 50 Scan UV-Visible Spectrophotometer. Scans were run using disposable cuvettes containing the CO_2 saturated MEA solutions within a range of 400 nm to 900 nm at a medium scan rate.

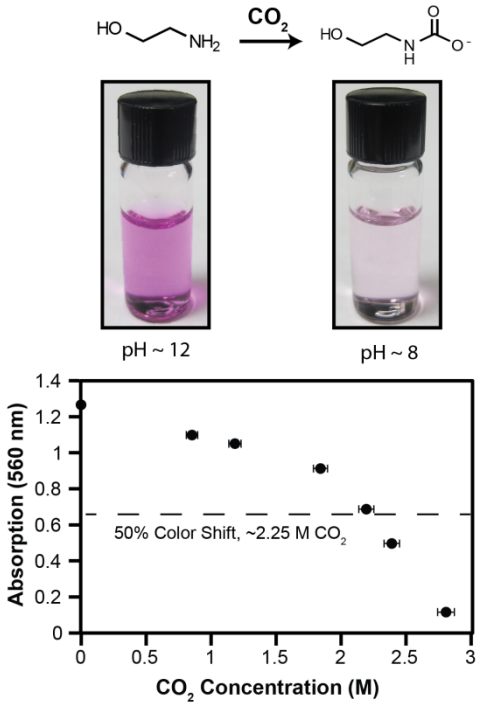

Figure A.2: Absorbance vs. concentration UV-Vis spectra of phenolphthalein dye in MEA. As the solution becomes more concentrated with CO_2, the pH decreases and phenolphthalein shifts from red to clear. This is indicated by the main absorption peak at 560 nm, which decreases as the carbamic acid concentration increases

A.2 Close Packing Structure

A.2.1 Fluorescent Temperature Measurement Probe

Rhodamine has previously been used to measure the temperature within microfluidic channels. However, these dyes can diffuse into the PDMS membrane and lower the accuracy of the temperature measurements. A two phase technique was used to optically measure the temperature profiles within the close packed exchangers. The pH sensitivity of fluorescein was coupled to the temperature sensitivity of Tris-HCL buffer. The relationship between intensity and pH is nonlinear for fluorescein within a larger range of pH, but within the values of 6-7, it is linear. This phenomena is useful as the relationship between pH and temperature for Tris-HCl is approximately linear within the pH range of 6-7 and a temperature range of 20-80 °C.

A.2.2 Heat Transfer Temperature Probe Calibration

A 250 mL solution of 10 μM Fluorescein in 10 mM Tris-HCl adjusted to a pH of 7.1 at 22 °C was prepared as the temperature probe. A 2.5 cm long, 300 μm diameter microchannel was fabricated with a thermistor element (Omega 5500 Series Glass Encapsulated Thermistor) embedded in contact with the microchannel in PDMS. A 7.5 cm long, 500 μm diameter microchannel was fabricated with a resistive heating wire coiled around the length of the microchannel to act as the heating element (Omega, Resistance Heating Wire, Nickel-Chromium Alloy, 80% Nickel/ 20% Chromium). A peristaltic pump (Buchler Polystaltic Pump) was used to flow the temperature probe solution through the heater and temperature sensing element at varying flow rates. The varying flow rates allowed for the temperature at the sensing element to change, while the change in intensity was measured using a fluorescent microscope (Figure A.3). Time lapsed images were taken using a Zeiss Axio Observer.A1

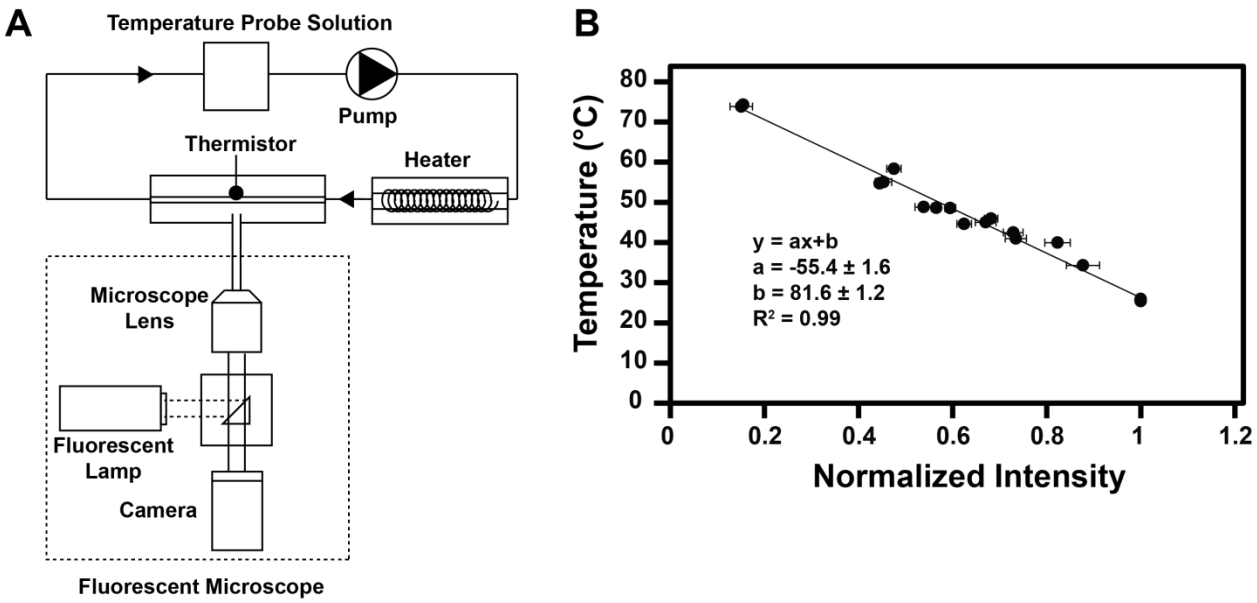

Figure A.3: Heat transfer temperature probe calibration. (A) Calibration schematic. The temperature probe flows continuously through a microchannel after being heated under different flow rates. The temperature is measured with a thermistor element and the intensity of the probe is measured with a fluorescent microscope. (B) Calibration results. A linear relationship between the normalized intensity and temperature was found within the temperature range between 75 and 25 °C.

Microscope. A 5 X objective was employed and images were aquired at intervals of 30 seconds for 20 minutes were taken for each temperature point. Baseline intensity measurements were also taken as the reference point for the intensity changes.

A.3 Hierarchical Microvascular Structures

A.3.1 Coated Membrane FTIR

The mixed region of PLA and PDMS due to the entrapment procedure led us to believe that it was possible for some PLA to remain within the PDMS membrane. We determined if this occurred using FTIR spectroscopy. A thin film of PLA was fabricated by dissolving PLA in trifluoroethanol (TFE) and casting the solution over a plate. The solvent evaporated leaving

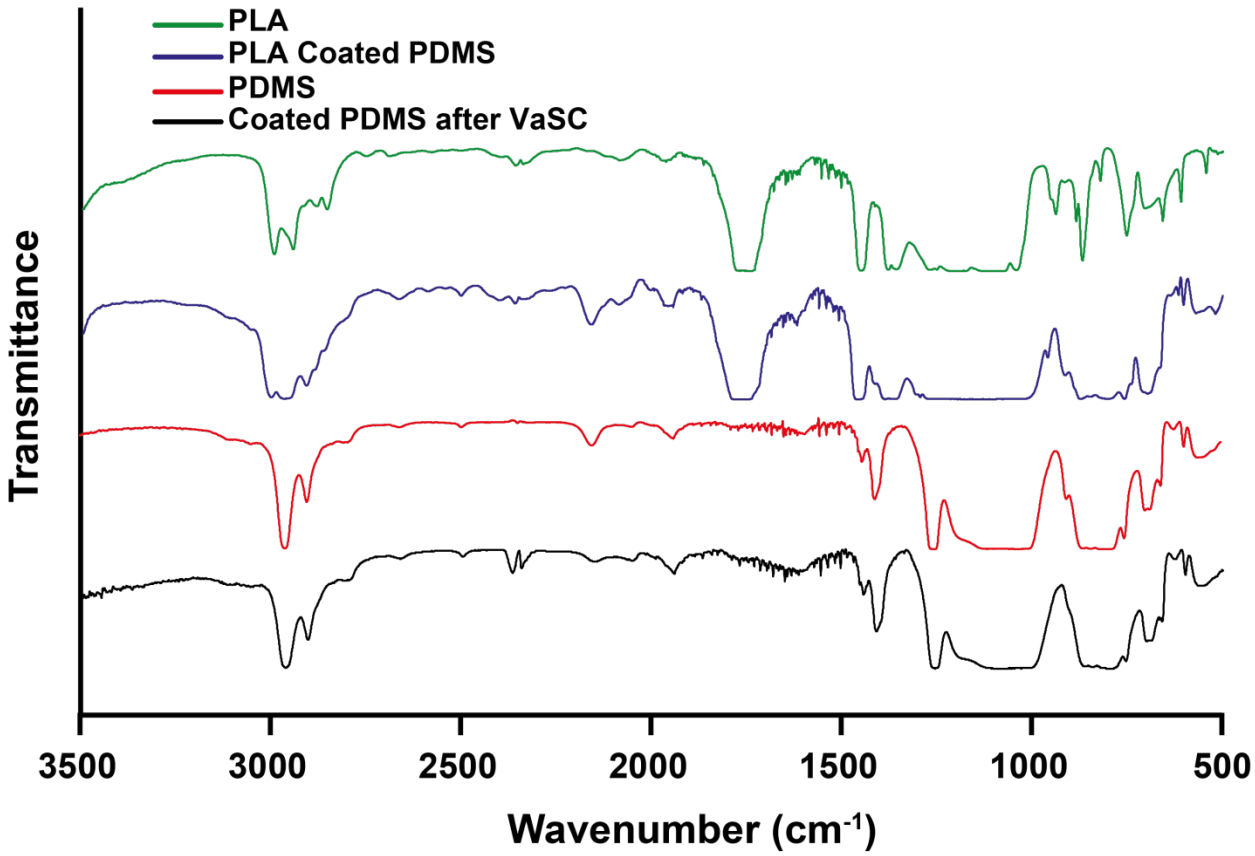

Figure A.4: Coated membrane FTIR data. A PLA film underwent the entrapment procedure with PDMS. The loss of the band near 1750 cm-1 confirmed the removal of PLA, resulting in a PDMS membrane after VaSC.

behind a film. The film was then treated for the VaSC technique and a PDMS membrane was entrapped onto its surface. The film was removed using VaSC, leaving behind the PDMS membrane. A PDMS film without PLA entrapment was also fabricated for comparison.

Using these films, FTIR spectrums of PLA, PLA coated with PDMS, PDMS, and PDMS after the PLA was removed using VaSC were obtained (Figure A.4). The PLA spectrum shows a band near 1750 cm^{-1}, corresponding to the carbonyl group. This band is not found in either the PDMS film nor the PDMS membrane formed through entrapment and VaSC, confirming the removal of PLA.

A.4 Waste Heat Usage

A.4.1 Additional Data Summary

Additional information regarding the effects of power on release rate, high speed optical analysis, and characterization of experimental parameters are provided.

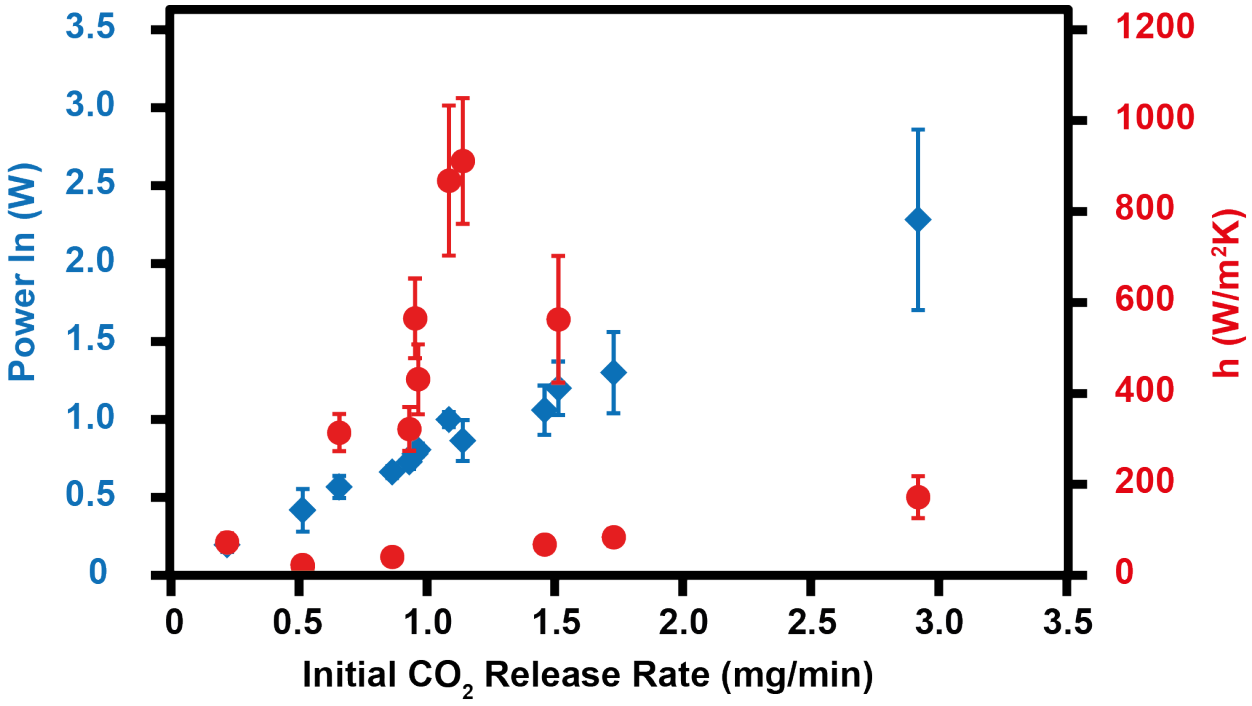

Figure A.5: Power In and Heat Transfer Coefficient vs. Initial CO_2 Release Rate. Values are plotted for each variance of the experimental parameters (channel type, temperature, and flow rate). Little correlation between the heat transfer coefficients and the initial release rates were found. A much stronger correlation was found between the power into the saturated MEA solution and the initial CO_2 release rates.

Trial	dt (ms)	U_i (m/s)	U_f (m/s)	x_i (mm)	x_f (mm)	$V_i \times 10^{-12}$ (m^3)	$V_f \times 10^{-12}$ (m^3)	P_i (kPa)	P_f (kPa)	Rate (mg/min)
1	12.9	0.43	0.7	7.8	12	3.0	1.5	68	65	0.90
2	15.6	0.69	1.7	7.9	20	1.0	1.3	69	61	0.74
3	16.2	0.36	2.0	9.1	19	5.2	7.7	65	62	0.43
4	10.2	0.54	1.5	11	19	1.5	9.2	65	61	0.71
5	10.5	0.56	1.6	11	20	3.6	1.5	65	61	1.00
6	9.4	0.75	1.4	11	19	2.0	8.9	66	61	0.68
7	11.4	0.38	1.9	9.7	19	1.7	1.4	65	63	1.02
8	14.5	0.33	1.5	9.7	19	1.9	1.1	64	62	0.58
9	75.8	0.66	1.8	11	19	1.7	7.9	66	62	0.79
10	9.4	0.77	1.3	11	19	4.0	1.1	66	61	0.73
11	10	0.37	1.4	11	19	2.6	8.1	63	61	0.52
12	8.2	0.46	1.0	9.5	16	3.5	1.3	66	63	1.13
13	15.2	0.52	0.9	8.9	16	2.4	1.1	67	63	0.54
14	13.8	0.32	2.6	9.3	19	1.6	1.3	64	63	0.83

Table A.1: Summary of data from high-speed optical analysis.

Channel Type	Flow Rate (mL/min)	Temperature (C)	Nusselt Number	Reynolds Number	Power In (W)	Heat Flux (W/m^2)
Hex	0.05	125	0.02 ± 0.004	1.8	1.06 ± 0.16	200 ± 70
Hex	0.1	125	0.03 ± 0.01	3.7	1.30 ± 0.26	810 ± 260
Hex	0.2	125	0.06 ± 0.02	7.4	2.28 ± 0.58	2760 ± 590
1.59 mm	0.05	125	0.11 ± 0.01	1.6	0.66 ± 0.04	510 ± 60
1.59 mm	0.1	125	0.06 ± 0.01	3.3	0.42 ± 0.04	790 ± 130
1.59 mm	0.2	125	0.06 ± 0.02	6.5	0.42 ± 0.14	800 ± 80
100 μm	0.1	125	0.16 ± 0.02	51.8	0.86 ± 0.13	11590 ± 1250
200 μm	0.1	125	0.20 ± 0.03	25.9	0.78 ± 0.04	10910 ± 1200
300 μm	0.05	125	0.17 ± 0.03	8.6	0.73 ± 0.05	3620 ± 490
300 μm	0.1	125	0.22 ± 0.04	17.3	0.81 ± 0.04	8580 ± 900
300 μm	0.2	125	0.45 ± 0.09	34.5	1.00 ± 0.05	18310 ± 980
300 μm	0.1	105	0.04 ± 0.01	17.3	0.20 ± 0.05	3240 ± 600
300 μm	0.1	115	0.16 ± 0.02	17.3	0.57 ± 0.07	7650 ± 360
300 μm	0.1	135	0.29 ± 0.07	17.3	1.20 ± 0.17	7750 ± 1450

Table A.2: Additional characterization of experimental parameters. Characteristic length for the Hexagonal sizes is considered to be 200 μm.

A.5 Photothermal Release of CO_2 from Capture Solutions using Nanoparticles

A.5.1 Nanoparticle Characterization

The carbon black nanoparticles were characterized with respect to their size and light absorbance. The particle sizes were measured using a Malvern Zetasizer AZ Nano DLS. The nanoparticles were examined in water, MEA, and MEA loaded with CO_2. The nanoparticles were distributed within the liquids at 0.001 wt% and dispersed under ultra-sonication. In water and MEA, the nanoparticle diameters ranged from 40 to 1000 nm, with an average of 200 nm (Figure A.6). When CO_2 was introduced into MEA, the particles agglomerated, resulting in an average measured particle diameter of 3 μm.

The carbon black nanoparticles were also characterized with respect to their light absorption (Figure A.7). The nanoparticles were distributed in water under ultra-sonication at 0.001 wt%. A Cary 50 Photospectrometer measured the transmittance of light through the nanoparticles over a wavelength range of 200 to 1100 nm. There is a broad absorption of light by the nanoparticles with wavelengths greater than 400 nm indicating its potential photo-thermal heat generation over a broad range.

A.5.2 Light Source Emission Spectra

The emission spectra of our light sources were examined using a Hitachi F4500 Fluorescent Spectrometer and a modified cuvette (Figure A.8). A set of optical fibers ran to the cuvette so that the emission of the light sources could be monitored by the spectrometer. It should be noted that due to the IR absorbance of glass, only the spectra for the visible range ought to be considered.

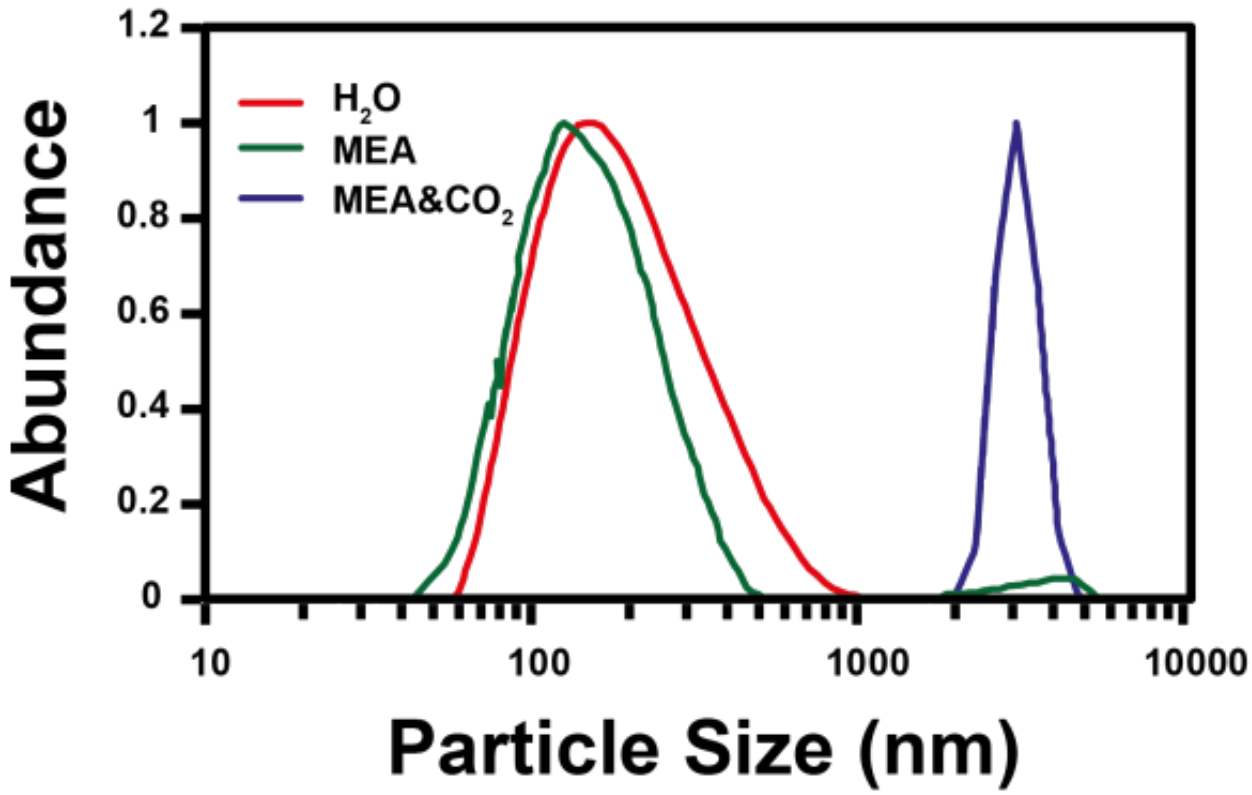

Figure A.6: Nanoparticle size distributions in H_2O, MEA, and MEA with CO_2

A.5.3 ^{13}C NMR Characterization

^{13}C NMR measurements were performed on the monoethanolamine and NCB nanofluid at three points: before CO_2 absorption, after CO_2 absorption, and after CO_2 desorption.

^{13}C NMR (125 MHz, D_2O, 1,4-dioxane), δ (ppm) = 67.19, 63.51, 43.10.

^{13}C NMR (125 MHz, D_2O, 1,4-dioxane), δ (ppm) = 165.14, 161.51, 67.19, 62.05, 58.71, 44.03, 42.10.

^{13}C NMR (125 MHz, D_2O, 1,4-dioxane), δ (ppm) = 164.97, 67.19, 63.01, 62.10, 44.11, 43.99, 43.18.

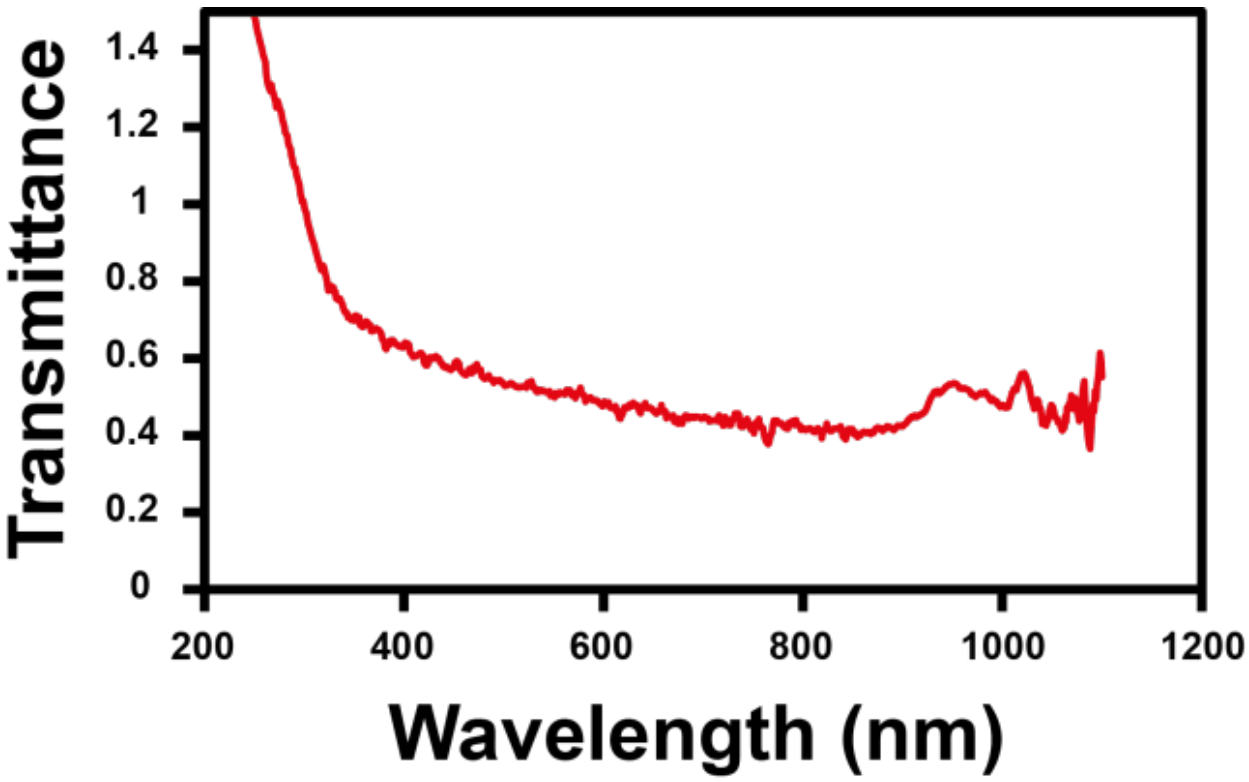

Figure A.7: UV-Vis Transmittance of carbon black.

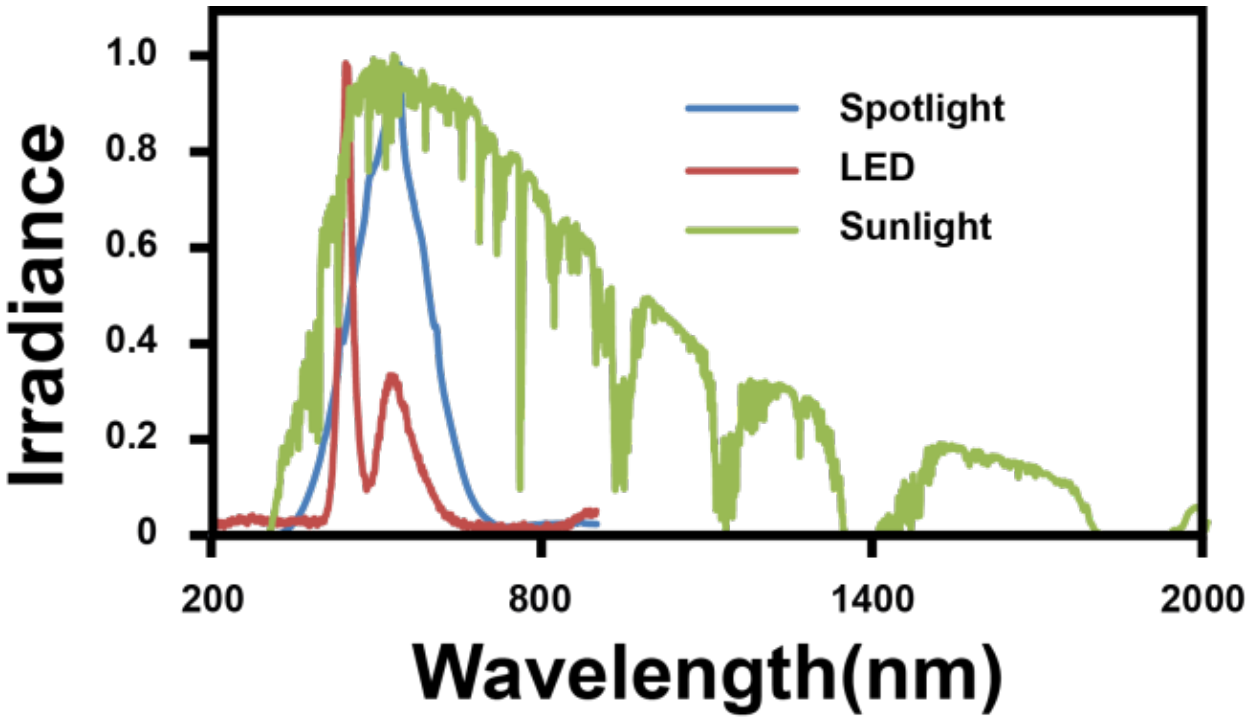

Figure A.8: Light source emission spectra

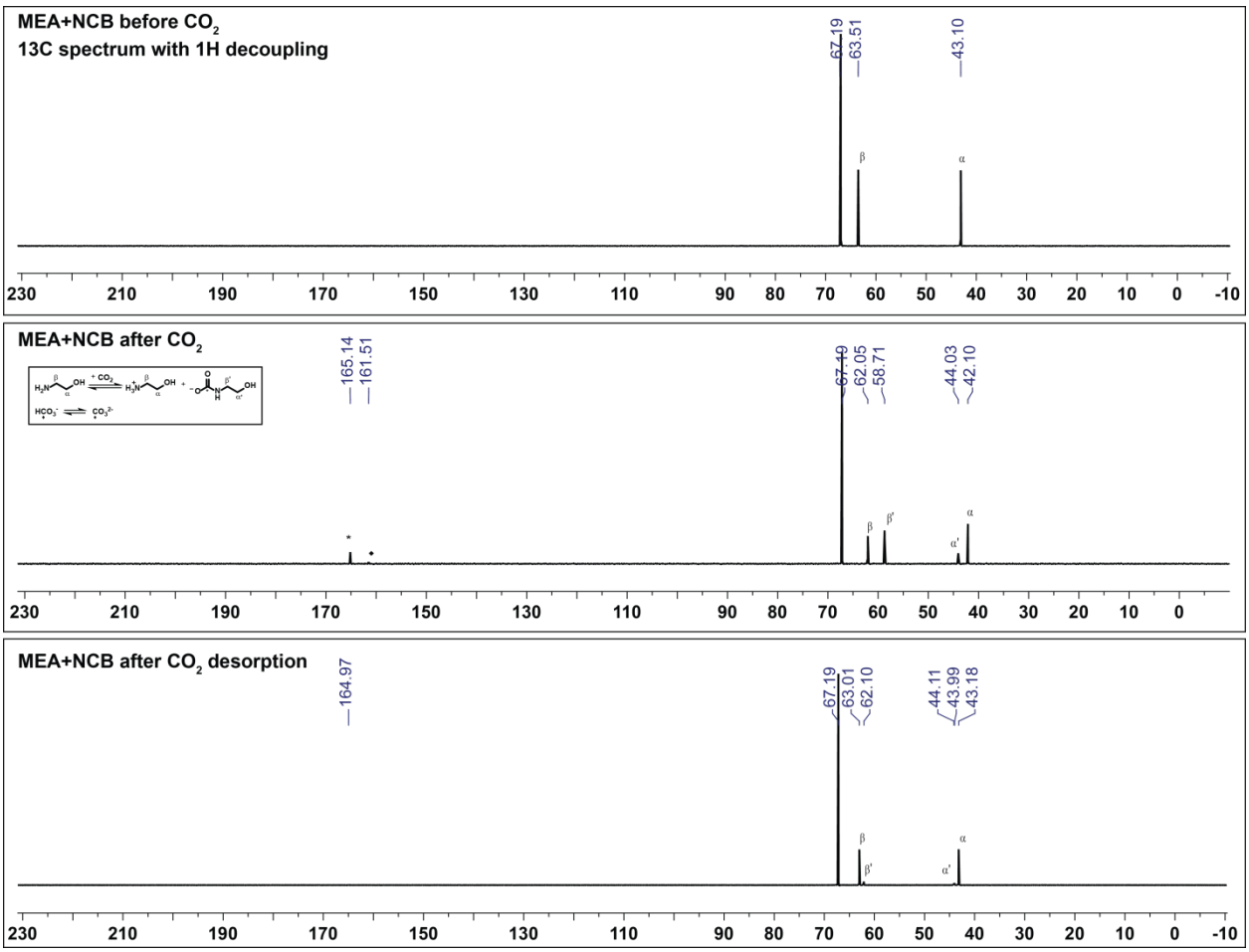

Figure A.9: ^{13}C NMR Measurements.